

TAILORING NANOSCOPIC AND MACROSCOPIC NONCOVALENT  
CHEMICAL PATTERNS ON LAYERED MATERIALS  
AT SUB-10 NM SCALES

A Dissertation  
Submitted to the Faculty  
of  
Purdue University  
by  
Jae Jin Bang

In Partial Fulfillment of the  
Requirements for the Degree  
of  
Doctor of Philosophy

December 2018  
Purdue University  
West Lafayette, Indiana

**THE PURDUE UNIVERSITY GRADUATE SCHOOL  
STATEMENT OF DISSERTATION APPROVAL**

Dr. Shelley A. Claridge, Chair

Department of Chemistry

Weldon School of Biomedical Engineering

Dr. David H. Thompson

Department of Chemistry

Dr. Elizabeth I. Parkinson

Department of Chemistry

Dr. Jianguo Mei

Department of Chemistry

**Approved by:**

Dr. Christine Hrycyna

Head of the School Graduate Program

For mom.

## ACKNOWLEDGMENTS

Broadly speaking, I would like to express my deepest gratitude to everyone who have made my journey in graduate school possible. I am extremely grateful to Professor Claridge for all the guidance and support that she provided me to help me mature into an independent chemist. Her motivation and commitment have always been inspiring and I am so fortunate to have her as my PhD mentor.

I would like to thank Prof. David Thompson, Prof. Jianguo Mei, Prof. Mary Wirth, Prof. Betsy Parkinson and Prof. Chen Yang for their helpful insights into my work and for being part of my committee. I extend my gratitude to Purdue electron microscopy facility, Dr. Gilpin, Bob and Laurie for their assistance with my research.

I also had amazing co-workers who made science even more exciting than it already is. I am happy for the warm friendship that I shared with everyone, especially the trilayer members: Tyson and Tyler. Our time at the small back office—full of interesting discussions and encouragement—is one of my fondest memory of Purdue and has been the source of motivation and inspiration for my work. Kortney and Shane have been great friends since we joined the Claridge group together in the first year. Shane’s work on spectroscopy and computational simulations have been particularly essential to this work. I am also grateful for all the knowledge and skills on synthesis shared by Erin, Ashlin and Terry. Jeremiah, Anni and John frequently offered excellent insights and advice whenever I was frustrated with my project. My spirit was also often lifted by the generous baking activities by the fellow group members. I am very thankful for all of Anni’s baking, Erin’s banana bread and Jeremiah’s zucchini bread. I would also like to thank Dave for all the help and advice that he has given our group in fixing and building instruments.

Most importantly, I would not have made it without the warm-hearted supports and love from my family and friends who always inspire me to achieve more. I genuinely appreciate presence of every single one of them in my life. An immense debt of gratitude is owed to my parents, aunts and uncles for all they have done to bring me up as a good person. I am also thankful to Hojung, Jeong-eun, Sun, Hyunji and InHaeng for their continued encouragements through college and graduate school. I thank my friends at PKLSG and 90MoIm especially. Yongbin, Hyunjin and Sora for their kind supports and advice. Finally, my PhD would not have been possible without my favorite people from Purdue: Arun, Marissa, Yoko, and Adam. Thank you very much.

## TABLE OF CONTENTS

	Page
LIST OF FIGURES . . . . .	viii
SYMBOLS . . . . .	xvi
ABBREVIATIONS . . . . .	xvii
ABSTRACT . . . . .	xx
1 MULTIMODAL SCANNING PROBE IMAGING: NANOSCALE CHEMICAL ANALYSIS FROM BIOLOGY TO RENEWABLE ENERGY . . . . .	1
1.1 Introduction . . . . .	1
1.2 Multimodal Atomic Force Microscopy . . . . .	3
1.2.1 Bias Application and/or Modulation (cAFM, EFM, KPFM, PRFM) . . . . .	5
1.2.2 Tip Height and Rotation Modulation (Force Curves and Multifrequency AFM) . . . . .	14
1.2.3 Application of External Stimuli (Electromagnetic Radiation, Heating, Mass Spectrometry, Magnetic Fields) . . . . .	21
1.3 Scanning Tunneling Microscopy (STM) . . . . .	28
1.3.1 Bias modulation (dI/dV, IETS, and Microwave) . . . . .	30
1.3.2 Tip Height Modulation ( <i>I</i> - <i>z</i> Spectroscopy) . . . . .	33
1.3.3 Application of External Stimuli (Magnetic Field and Electromagnetic Radiation) . . . . .	34
1.4 Conclusions and Prospects . . . . .	37
2 SITTING PHASES OF POLYMERIZABLE AMPHIPHILES FOR CONTROLLED FUNCTIONALIZATION OF LAYERED MATERIALS . . . . .	42
2.1 Introduction . . . . .	42
2.2 Results and Discussions . . . . .	45
2.2.1 Self-Assembled Sitting Phases of Diyne Phospholipids. . . . .	45
2.2.2 Polymerization of Diyne Phospholipids . . . . .	49
2.2.3 Controlling the Charge State of Surface Functional Group Patterns. . . . .	54
2.3 Conclusion and Prospects . . . . .	58
2.4 Experimental Methods . . . . .	59

	Page
3 HIERARCHICALLY PATTERNED NONCOVALENT FUNCTIONALIZATION OF 2D CONTROLLED LANGMUIR-SCHAEFER CONVERSION . . .	63
3.1 Introduction . . . . .	63
3.2 Results and Discussion . . . . .	67
3.2.1 Comparison of Transfer from Liquid Expanded and Condensed Phases in Langmuir Films . . . . .	68
3.2.2 Polymerization-Induced Cracking Reveals Lamellar Directionality.	71
3.2.3 Correlation of Large-Scale Features in Langmuir Films Undergoing Collapse and Transferred Film Structures on HOPG. . . .	74
3.2.4 Nanoscopic Features in Transferred Films . . . . .	76
3.2.5 Identification of Transfer Parameters Leading to High Degrees of Ordered Domain Coverage and/or Large Domain Sizes. . . .	77
3.3 Conclusion . . . . .	82
3.4 Experimental Methods . . . . .	83
4 SPATIALLY CONTROLLED NONCOVALENT FUNCTIONALIZATION OF 2D MATERIALS BASED ON MOLECULAR ARCHITECTURE . . . .	86
4.1 Introduction . . . . .	86
4.2 Results and Discussion . . . . .	89
4.2.1 Preparation and Characterization of Lying-Down and Sitting-Phase Monolayers . . . . .	89
4.2.2 Comparison of LS Transfer Efficiency with Molecular Structure.	93
4.2.3 Adsorption, Diffusion, and Nucleation Rates Modulate Domain Structure. . . . .	101
4.3 Conclusions . . . . .	104
4.4 Experimental Methods . . . . .	104
REFERENCES . . . . .	108
PUBLICATION . . . . .	139

## LIST OF FIGURES

Figure	Page
1.1 Overview of multimodal AFM and STM techniques incorporating: (1) an applied bias, (2) modulation of tip position (height or tapping frequency), or (3) an external stimulus or colocalized measurement modality. . . . .	2
1.2 Multimodal AFM with constant or variable bias probes local electronic properties including conductivity, local surface potential, or local piezoelectric effects. . . . .	7
1.3 Multimodal AFM with applied bias. (a) AFM topography and KPFM images of a polymer blend film both unilluminated (middle) and illuminated (right), showing the change in work function for individual polymer domains. (b) AFM topography and PRFM amplitude and phase of a nanostructured ferroelectric material, showing differences in poling directions in individual domains. Adapted with permission from ref. [88] and [89]. Copyright 2010 American Chemical Society and 2013 John Wiley and Sons.	9
1.4 Multimodal AFM with varied tip vertical position measures local mechanical properties including Young's modulus and elasticity. . . . .	14
1.5 Examples of single-molecule force curves and molecular recognition imaging. (a) Single-molecular force spectroscopy experiment measuring forces required to unfold individual subunits of titin protein. (b) Simultaneously acquired topography and molecular recognition imaging of a biotin-functionalized tip interacting with an avidin-functionalized surface. Avidin molecules appear as protrusions in the topography image, and as depressions in the recognition image. Adapted with permission from ref. [127] and [129]. Copyright 1997 AAAS and 2005 John Wiley and Sons. . . . .	16



Figure	Page
1.6 Examples of multimodal AFM exciting multiple resonant frequencies. (a) Bimodal AFM exciting both first and second cantilever harmonics to image ferritin proteins with and without iron oxide nanoparticle cores. First harmonic image reveals surface topography, while second harmonic provides contrast showing the presence or absence of the magnetic nanoparticle within the protein. (b) AFM holography reveals subsurface features with different mechanical properties by applying vibrations to the sample, and detecting transmission of the vibrations to the tip. Standard AFM image (left) shows surface topography of rat alveolar cells, while holography image (right) reveals the presence of sub-surface silica nanoparticles. Adapted with permission from ref. [152] and [153]. Copyright 2006 National Academy of Sciences and 2008 AIP Publishing LLC. . . . .	20
1.7 Multimodal AFM incorporating external stimuli or a colocalized measurement modality can be used to collect local information about the presence of specific chemical bonds, chemical species with specific masses, local phase transition temperatures, or thermal expansion. . . . .	22
1.8 Multimodal AFM employing external stimulus. (a) AFM with confocal Raman imaging of a bilayer graphene nanoribbon (GNR). Raman spectrum over GNR shows broadened 2D peak characteristic of bilayer graphene. (b) AFM-IR using synchrotron radiation to illuminate an AFM tip, which provides near-field enhancement. A spectrum collected over a nanoscale area of a peptoid sheet on the substrate exhibits the characteristic peptide amide I band at $1650\text{ cm}^{-1}$ . Overlaid AFM and IR images provide sub-diffraction localization of the peptoid sheets on the substrate. (c) Colocalized AFM and MFM images of a cobalt nanocrystal film reveal domains $\sim 100\text{ nm}$ in diameter with shared magnetization. (d) MS-AFM optical micrograph (left) of <i>Pseudomonas</i> GM15 colony including crystalline material imaged by AFM-MS. Mass spectrum (middle) of phenzaine-1-carboxamide, showing protonated peak at $m/z\ 224$ . AFM-MS image (right) overlays intensity of peak at $m/z\ 224$ as a color gradient on the 3D AFM image, providing chemical contrast highlighting the likely locations of P1C crystals. Adapted with permission from ref. [163], [164], [165] and [166]. Copyright 2009 Macmillan Publishers Ltd, 2014 National Academy of Sciences, 2014 American Chemical Society, and 2004 Macmillan Publishers Ltd. . . . .	24
1.9 Multimodal STM employing bias modulation, tip height modulation, or an external stimulus. . . . .	29

- 1.10 Multimodal STM employing bias modulation. (a)  $dI/dV$  spectroscopy identifies the HOMO and LUMO energy levels of a pentacene molecule adsorbed to an insulating bilayer of NaCl on conductive Cu(111). Subsequent STM imaging of a pentacene molecule at a bias corresponding to the energy level of the HOMO, the LUMO, and an intermediate bias in the gap produce images correlated with HOMO and LUMO orbital shapes as calculated using DFT. (b) IETS and IETS mapping. Using an STM tip modified with a single CO molecule allows the surface to be imaged with chemical contrast using a bias corresponding to a vibrational excitation of the CO molecule. IETS spectra acquired at several points over the molecule reveal that the CO hindered translational mode at 2.8 mV shifts to 1.7 mV when the tip sits over a bond in a cobalt phthalocyanine molecule on the Ag(110) surface. Imaging an individual CoPC molecule at 1.7 mV produces a skeletal image of the CoPC bond structure. (d) Microwave frequency bias modulation provides a simultaneously acquired second data channel showing polarizability of the molecule in the junction. Highly polarizable OPE molecules appear in high contrast against a background of less polarizable alkanethiols. Adapted with permission from ref. [186], [187], and [188]. Copyright 2010 American Chemical society, 2005 American Physical Society, and 2014 AAAS. . . . . 39
- 1.11 Multimodal AFM employing magnetic field. STM image showing two islands of Co atoms on Ir(111). Application of a 0.6 T magnetic field and  $dI/dV$  imaging at 250 mV reveals differences in conductances of the two islands based on spin alignment with (red) or against (purple) the orientations of spins in the magnetic Fe-coated-W STM tip. Adapted with permission from ref. [232]. Copyright 2011 American Physical Society. 40
- 1.12 Examples of multimodal AFM employing external stimuli. (a) Standard STM and STM-TERS images of amyloid peptide fibrils, which exhibit chemical contrast in the TERS image based on the aromatic ring breathing mode at  $1004\text{ cm}^{-1}$ . (b) Standard and X-ray STM showing chemical contrast from few-nm Ni clusters on Cu(111). Adapted with permission from ref. [252] and [256]. Copyright 2013 and 2014 American Chemical Society. . . . . 41
- 2.1 Topochemical polymerization of diyne lipids. . . . . 45

Figure	Page
2.2 Modeled structures and AFM images of self-assembled polymerizable amphiphiles on HOPG. The first column shows (a) PCDA, (b) diyne PC, and (c) diyne PE. For each molecule, the second column shows two views of the solvent-minimized molecular structure (top) and a view of the solvent structure adsorbed to HOPG (bottom). The adsorbed structures were minimized to create the models in the third column, showing top and side views of each monolayer. In the fourth column, AFM phase images show large domains of molecules oriented epitaxially on HOPG; high-resolution images in the fifth column reveal lamellar periodicities ( $\sim 6$ nm) commensurate with the head-to-head models shown in the second column. . . . .	46
2.3 Minimizations of amphiphiles in phosphate-down and phosphate-up adsorption geometries. Minimized models of rows of molecules adsorbed in (a) phosphate-down and (b) phosphate-up configurations reveal greater tail group ordering for the phosphate-down configuration in both interdigitated and noninterdigitated headgroup configurations. (c) Energy differences between the two adsorption configurations indicate that the phosphate-down conformation is preferred due to increased van der Waals interactions. . . . .	48
2.4 Energy-minimized molecular models and STM images showing polymerized (a–d) PCDA and (e–h) diyne PC. Minimized models of (b) unpolymerized PCDA and (f) diyne PC show that the distance between bond-forming carbons ( $D_{10-13}$ ) and the angle between diyne and lamellar axis ( $\theta$ ) are similar for the two molecules. STM images of polymerized (d) PCDA and (h) diyne PC show apparent protrusions corresponding to the conjugated ene-yne polymer. Highlighting in panel (e) indicates the alternating alkyl chain orientation probed in Figure 2.6. . . . .	51
2.5 Solvent washing assay for unpolymerized and polymerized PCDA (a and b) and diyne PE (c and d) shows the enhanced stability of polymerized monolayers in comparison with unpolymerized monolayers and increased stability of diyne PE vs PCDA. Insets of panels a and b show phase images of the entire images or the corresponding scanned areas marked by the black square. . . . .	54
2.6 PM-IRRAS spectra of films of PCDA and diyne PC exhibit differences in (a) C–H and (b) C=O stretch intensities consistent with alkyl chain orientation differences observed in energy-minimized molecular models. . .	55

Figure	Page	
2.7	Contact angle titrations showing changes in contact angle with buffer pH for HOPG with adsorbed (a) pentacosane, (b) polymerized PCDA, and (c) polymerized diyne lipids PC and PE. Square markers indicate advancing contact angles; circles indicate receding contact angles. Error bars indicate the standard deviation in angle over a series of nine measurements acquired from three different samples. . . . .	56
3.1	Structures of 10,12-PCDA (a) before and (b) after photopolymerization. Molecular models of (c) pre- and (d) postpolymerization lying-down phases epitaxially assembled on HOPG. (e) Schematic of targeted hierarchical nano- and microscale noncovalent functionalization of 2D material. . . . .	64
3.2	(a) Schematic showing molecular assembly of Langmuir film on aqueous subphase with microscale patterns in ordering. (b) Schematic of conversion of molecules from the standing phase Langmuir film into a lying-down phase on HOPG. . . . .	67
3.3	(a) Pressure-area isotherms for Langmuir films of PCDA on pure water at 20 °C (blue) and 30 °C (orange). (b) AFM image of typical nanoscopic ordering observed when lamellar phases are assembled on HOPG through LS transfer. White arrows highlight lamellar alignment in epitaxy with HOPG; the feature running from top left to bottom center is a step edge in the HOPG substrate. . . . .	68
3.4	(a) SEM images of PCDA film transferred at 30 °C, 30 Å <sup>2</sup> / molecule and photopolymerized after transfer but prior to SEM imaging. Scale bars represent (a) 100 μm and (b) 1 μm. Image in (b) is acquired from the highlighted region in (a). . . . .	69
3.5	SEM images of PCDA film transferred with the substrate lowered onto subphase at (a) 1, (b) 10, and (c) 50 mm/min. (d) Average circle diameters vs dipping speed. . . . .	72
3.6	(a) AFM and (b) SEM images showing domain structure of PCDA transferred to HOPG and then photopolymerized; cracking defects visible in SEM image. (c) Minimized molecular models showing polymerization-induced lamellar narrowing that leads to cracking in (b). (d) Images illustrating beam-induced formation of dendritic phases in nonpolymerizable domains. (e, f) AFM and SEM images of large-scale domain morphology. (g, h) Comparison of AFM and SEM images of disordered amorphous domains. . . . .	73

Figure	Page
3.7 (a) BAM image of a Langmuir film of PCDA at 20 °C and 20 Å <sup>2</sup> /molecule. (b, c) SEM images of PCDA films transferred to HOPG under the conditions illustrated in (a) and then photopolymerized. (c) A high-resolution SEM image of the small area of (b) highlighted with a black box. . . . .	75
3.8 (a) AFM images of PCDA transferred to HOPG at 30 °C, 35 Å <sup>2</sup> /molecule and then photopolymerized. Crossed arrow pattern indicates axes of crosshatched pattern of nanoscale domains. White boxes highlight transition from full to monolayer coverage to nanoscopic vacancies (upper left), a representative transferred nanoscopic molecular area (lower right). (b) BAM image of PCDA on aqueous subphase acquired at 35 and 30 Å <sup>2</sup> /molecule, showing larger-scale dendritic pattern. (c) Enlargement of tight-packed/nanoscale-vacancy boundary. (d) Enlargement of lower transferred nanoscopic feature highlighted in (a). . . . .	77
3.9 (a) Pressure-area isotherms for PCDA transferred from subphases at temperatures of 20 °C (left) and 30 °C (right). (b-d) SEM images of typical PCDA films transferred to HOPG at 20 °C (left) and 30 °C (right), at mean molecular areas of (b) 20, (c) 30, and (d) 40 Å <sup>2</sup> /molecule. Films were photopolymerized after transfer but prior to SEM imaging. . . . .	78
3.10 Analysis of film transfer at points along isotherms at 20 and 30 °C. (a) Isotherms, (b) transfer ratios, and (c) Langmuir film packing densities (expressed relative to ideal lying-down phase packing densities). (d) HOPG coverage after transfer, expressed as fractional coverage of lamellar (blue), amorphous (gold), and standing or multilayer (green) domain structure, with amount of vacant surface shown in red. (e) Average domain sizes for monolayers on HOPG and (f) polymerization-induced crack densities for monolayers on HOPG, expressed in cracks/μm. . . . .	80
3.11 AFM images of PCDA film transferred at 20 °C and 35 Å <sup>2</sup> / molecule: (a) as-transferred film structure and (b) same area of film after annealing for 1 h at 50 °C. . . . .	81
4.1 (a) Schematic of lying-down phase of PCDA on HOPG and hierarchical nanoscopic and microscopic assembly. (b) Schematic illustrating other amphiphile head and chain architectures for functionalization of 2D materials.	87
4.2 Schematic of LS conversion for (a) single-chain amphiphiles and (b) dual-chain amphiphiles, with schematics of expected domain structures (right).	89
4.3 (a, b) Lamellar structures of (a) PCDA and (b) diyne PC on HOPG. (c, d) AFM images of nanoscopic domain structure for PCDA and diyne PC on HOPG after LS conversion. (e, f) AFM images showing limited contrast from headgroups in PCDA (e) vs diyne PC (f). . . . .	90

Figure	Page
4.4 (a) BAM image of PCDA Langmuir film compressed to $30 \text{ \AA}^2/\text{chain}$ at a subphase temperature of $20^\circ\text{C}$ . (b–d) SEM images of PCDA film on HOPG after LS conversion. Inset in (d) shows molecular model of lamellar narrowing that leads to cracking visible in (d).	91
4.5 (a) BAM image of diyne PC Langmuir film compressed to $30 \text{ \AA}^2/\text{chain}$ at a subphase temperature of $20^\circ\text{C}$ . (b–d) SEM images of diyne PC film on HOPG after LS conversion illustrating local differences in extent of molecular transfer and domain shapes.	93
4.6 Chemical structures of the five amphiphiles used in LS transfer experiments (from left to right): PCD-NH <sub>2</sub> , PCDA, NAPDA, diyne PE, and diyne PC.	94
4.7 Isotherms of Langmuir films of single-chain amphiphiles from $10\text{--}30^\circ\text{C}$ (left) and SEM images of molecules assembled on HOPG after LS transfer at $20^\circ\text{C}$ , $30 \text{ \AA}^2/\text{chain}$ (right), for the following amphiphiles: (a) PCD-NH <sub>2</sub> , (b) PCDA, and (c) NAPDA. Insets show nanoscale domain structures. Color codes for temperatures shown in (a) are the same for each panel.	95
4.8 Isotherms of Langmuir films of phospholipids from $10\text{--}30^\circ\text{C}$ (left) and SEM images of molecules assembled on HOPG after LS transfer at $20^\circ\text{C}$ , $30 \text{ \AA}^2/\text{chain}$ (right), for the following amphiphiles: (a) diyne PE and (b) diyne PC. Insets show nanoscale domain structures. Color codes for temperatures shown in (a) are the same for each panel.	97
4.9 (a) Isotherms for diyne PE (left) and diyne PC (right) on subphases of pure water, 100 mM NaCl, and 40 mM CaCl <sub>2</sub> . (b) Langmuir film packing density, expressed as a ratio with the number of molecules required to form a full lying-down phase. (c) Transfer ratios for molecules undergoing LS transfer from a pure water subphase onto HOPG, with lamellar (blue), amorphous (yellow), and standing (green) phases quantified individually. (d–f) Fractional surface coverage of diyne PE (left) and diyne PC (right) on HOPG after transfer from subphases composed of (d) pure water, (e) 100 mM NaCl, and (f) 40 mM CaCl <sub>2</sub> .	98
4.10 SEM images of diyne PE (left) and diyne PC (right) transferred at $20^\circ\text{C}$ and $30 \text{ \AA}^2/\text{chain}$ using a dipping speed of (a) 2 mm/min and (b) 50 mm/min. (c) SEM image of diyne PE prepared via in situ thermal annealing. The subphase, aqueous 5 mM MnCl <sub>2</sub> solution, was heated to $30^\circ\text{C}$ while the substrate was also heated to $70^\circ\text{C}$ throughout deposition.	100

- 4.11 (a) Representative AFM images of domain structures of PCDA, PCD-NH<sub>2</sub>, NAPDA, diyne PE, and diyne PC. Insets (80 nm × 120 nm) show nanoscopic lamellar structure and domain edges. (b) Number density of domains ( $\log(N)$ ) vs fractional surface coverage for PCDA (blue), diyne PE (red), and diyne PC (yellow). Insets illustrate the portion of the vertical scale from 0 to 11. . . . . 102

## SYMBOLS

$N$	number density of domains
$F$	molecular adsorption rate
$D$	rate of molecular diffusion
$C$	average transferred coverage
$\chi$	fraction of surface coverage
$\alpha$	transfer ratio



## ABBREVIATIONS

PCDA	10,12-pentacosadiynoic acid
PCD-NH <sub>2</sub>	10,12-pentacosadiyn-1-amine
NAPDA	N-(2-aminoethyl)-10,12-diynamide
diyne PE	1,2-bis(10,12-tricosadiynoyl)-sn- glycero-3-phosphoethanolamine
diyne PC	1,2-bis(10,12-tricosadiynoyl)-sn-glycero-3-phosphocholine
LS	Langmuir-Schaefer
LB	Langmuir-Blodgett
mma	mean molecular area
SAM	self-assembled monolayer
HOPG	highly oriented pyrolytic graphite
LE	liquid expanded
LC	liquid condensed
SEM	scanning electron microscopy
BAM	Brewster angle microscopy
IR	infrared
CPD	contact potential difference
PEDOT:PSS	poly(3,4-ethylenedioxythiophene) polystyrenesulfonate
P3HT	poly(3-hexyl thiophene)
PCBM	P3HT/phenyl-C61-butyric acid methyl ester
FET	field effect transistor
FIB	focused ion beam
DNA	deoxyribonucleic acid
PEG	poly(ethylene glycol)

CoPC	cobalt phthalocyanine
OPE	oligo(phenyleneethynylene)
STM	scanning tunneling microscopy
LDOS	local density of states
STS	scanning tunneling spectroscopy
HOMO	highest occupied molecular orbital
LUMO	lowest unoccupied molecular orbital
IETS	inelastic electron tunneling spectroscopy
SP-STM	spin-polarized scanning tunneling microscopy
DFT	density functional theory
UHV	ultra-high vacuum
SXSTM	synchrotron X-ray scanning tunneling microscopy
AFM	atomic force microscopy
cAFM	conductive atomic force microscopy
EFM	electrostatic force microscopy
KPFM	Kelvin probe force microscopy
PRFM	piezoresponse force microscopy
SCM	scanning capacitance microscopy
SECM	scanning electrochemical microscopy
UME	ultramicroelectrode
TERS	tip-enhanced Raman spectroscopy
s-SNOM	scattering scanning near-field optical microscopy
MFM	magnetic force microscopy
MRFM	magnetic resonance force microscopy
SJEM	scanning Joule expansion microscopy
SIMS	secondary ion mass spectrometry
PMMA	polymethylmethacrylate
PS	polystyrene
ESI	electrospray ionization

P1C            phenazine-1-carboxamide

## ABSTRACT

Bang, Jae Jin PhD, Purdue University, December 2018. Tailoring Nanoscopic and Macroscopic Noncovalent Chemical Patterns on Layered Materials at Sub-10 nm Scales. Major Professor: Shelley A. Claridge.

The unprecedented properties of 2D materials such as graphene and MoS<sub>2</sub> have been researched extensively [1,2] for a range of applications including nanoscale electronic and optoelectronic devices [3–6]. Their unique physical and electronic properties promise them as the next generation materials for electrodes and other functional units in nanostructured devices. However, successful incorporation of 2D materials into devices entails development of high resolution patterning techniques that are applicable to 2D materials. Patterning at the sub-10 nm scale is particularly of great interest as the next technology nodes require patterning of (semi)conductors and insulators at 7 nm and 5 nm scales for nanoelectronics. It will also benefit organic photovoltaic cells as phase segregation of p/n-type semiconducting polymers on 2D electrodes at length scales smaller than the typical exciton diffusion length (10 nm) is expected to improve the charge separation efficiency [7].

However, traditional photolithography faces challenges at high resolution due to the diffraction limit [8,9]; designing high NA optics for shorter wavelengths is accompanied by prohibitively increasing cost. Other top-down methods such as electron beam lithography and dip-pen lithography offer high resolution but have limited throughput. Therefore, to construct 2D devices with reproducible properties, it is necessary to develop novel strategies to control interfacial chemistry of 2D materials with high precision—ideally at sub-10 nm scales.

One preferred approach for locally functionalizing 2D materials is via non-covalent assembly of molecular monolayers to avoid disrupting the in-plane bonding network of the 2D materials (e.g. delocalized  $\pi$ -electrons in graphene) that give rise to their unique properties. Self-assembly is an inexpensive bottom-up process in which molecules organize themselves into defined structures without external stimuli. It presents a feasible and scalable alternative to current lithographic techniques. Such non-covalent assemblies are particularly useful at interfaces with 2D materials, which exhibit high sensitivity of their physical/chemical properties to the interfacial environment [10, 11].

Self-assembled monolayers (SAMs) on 2D materials have been reported for various classes of organic molecules (e.g. alkanes and their derivatives, polymers and polycyclic aromatics such as porphyrins, and phthalocyanines) [10, 12]. In order to compensate for the relative weak molecule-substrate interactions in noncovalent SAMs, the constituent molecules often include long alkyl chains and/or aromatic cores which result in large numbers of atoms experiencing van der Waals interactions with the substrate [11–13]. Especially, the long alkyl chain groups assist with molecular packing via intermolecular van der Waals interactions, improving the ordering and the stability of the monolayer.

We noted that the cross-section of cell membranes, consisting of amphiphiles, have length scales that closely match with the sub-10 nm patterning scale mentioned above. Along with other amphiphiles, fatty acids have been widely reported to assemble into striped lying-down phases on highly oriented pyrolytic graphite (HOPG) with head-to-head interactions between carboxylic groups [12, 14]. In particular, 2D assemblies of 10,12-pentacosadiynoic acid (PCDA) have been studied by many groups for their ability to form conductive ene-yne molecular wires upon photopolymerization [14–17]. This suggests the possibility of using photopolymerizable diyne groups to enhance robustness of the monolayer. PCDA assembles into rows, driven by inter-chain van der Waals interactions, allowing topochemical polymerization while maintaining the molecular directional epitaxy with the graphitic lattice. Dimerization

of the carboxylic headgroups confers additional stability to the PCDA monolayer structure. Consequently, the assembly results in monolayers of PCDA that produce chemically orthogonal lamellar patterns with  $\sim 6$  nm periodicity, with each lamella representing a double row of molecules. In this work, we discuss using other types of diyne-functionalized amphiphiles to construct sub-10 nm chemical patterns as an alternative 2D patterning technique, investigating the assembly and the properties of the amphiphilic monolayers.

Characterizing locally modulated properties of non-covalently functionalized 2D materials requires high-resolution imaging techniques capable of extracting measurements of various physical/chemical properties. One such method is scanning probe microscopy (SPM) [18–21]. In Chapter 1, we present a brief review of SPM modalities, some of which are used to characterize interfacial properties, such as conductivity and local contact potential differences that can be modulated by amphiphilic assemblies [17, 22]. Atomic force microscopy (AFM) is one of main techniques that we use to determine topography. All imaging in this work were performed in attractive AC mode [23, 24] in order to minimize disruption to the self-assembly of the amphiphiles by the scanning tip.

One challenge of using SAMs for locally modulated functionalization is that the proximity to the nonpolar interface can modify the behavior of the functionalities present on the surface in conjunction with the steric hindrance of 2D molecular assemblies. For instance, ionizable functional groups, one of the strongest local modulators of surface chemistry, undergo substantial  $pK_a$  shifts (in some cases,  $> 5$  units) at non-polar interfaces, limiting their ability to ionize. In order to apply molecular assembly to create 2D chemical patterns, we needed to design alternative structures that can avoid such penalties against the intrinsic properties of functionalities present in the assemblies. Among amphiphiles, we observed that the chiral centers of phospholipids have the potential of elevating the terminal functional group in the head from the surface for improved accessibility. We refer to this type of assembly as a ‘sitting’ phase. Chapter 2 describes sitting phase assembly of phospholipids; the projection of

the terminal functionality allows it to maintain solution phase-like behavior while the dual alkyl tails provide additional stabilizing interactions with the substrates. Given the diversity of phospholipid architecture [25], the sitting phase assembly suggests the possibility of greatly diversifying the orthogonality of the chemical patterns, allowing highly precise control over surface functionalities.

While a variety of methods including drop-casting [26–28] and microcontact printing [29] have been used previously by others for noncovalent assembly of materials on the surface, they mostly address patterning scale in the sub- $\mu\text{m}$  range. Here, we utilize Langmuir-Schaefer (LS) transfer, which has been historically used to transfer standing phase multilayers [30], and lying-down domains of PCDA at  $< 100$  nm scales in the interest of molecular electronics [14, 31–33], as our sample preparation technique. LS transfer is remarkable in that the transferred molecules relinquish their pre-existing interactions in the standing phase at air-water interface to undergo  $\sim 90^\circ$  rotation and assemble into the striped phase on a substrate. This introduces the possibility of modulating local transfer rate across the substrate by manipulating local environment of the molecules. Thus, LS transfer has the potential to offer spatial control over the noncovalent chemical functionalization of the 2D substrate, essential in device applications.

In Chapter 3 and 4, We make comparative studies of various experimental factors such as surface pressure, temperature and molecular interactions that affect the efficiency of LS conversion. Considering the energetics of the transfer process, we predicted that the rate of transfer from the air-water interface to the substrate should be the highest from the regions around defects, which would be the energetically least stable regions of the Langmuir film [34, 35]. In Langmuir films, two phases of lipid assemblies—liquid expanded (LE) and liquid condensed (LC)—often coexist at the low surface pressures ( $< 10$  mN/m) used for sample preparation. Hence, we hypothesized that the microscale structural heterogeneity of Langmuir films could be translated into microscale patterns in the transferred film on HOPG. We compare the transfer rates between LE and LC phases and investigate the impacts of physi-

cal conditions during LS transfer such as temperature, packing density, dipping rate and contact time to conclude that local destabilization of Langmuir films leads to increased transfer efficiency. (Chapter 3)

As in the case of lipid membranes that reorganize routinely based on the structure of the constituent molecules [36–38], the structure of Langmuir films is strongly dependent on the molecular structures of the constituent molecules [39–43]. Accordingly, we expected the molecular structures/interactions to provide additional control over the LS transfer process. In Chapter 4, we compare domain morphologies and the average coverages between three single chain amphiphiles and two phospholipids, each of which contain hydrogen bonding motifs of varying strengths. We show that by influencing the adsorption and diffusion rates, molecular architecture indeed influences LS conversion efficiency and subsequent assembly on the substrate. The presence of strong lateral interactions limits transfer and diffusion, forming vacancies in the transferred films with smaller domain sizes while weaker intermolecular interactions enabled high transfer efficiencies.



## 1. MULTIMODAL SCANNING PROBE IMAGING: NANOSCALE CHEMICAL ANALYSIS FROM BIOLOGY TO RENEWABLE ENERGY

A version of this chapter has been published in *Anal. Methods*.

DOI: 10.1039/c5ay00507h

### 1.1 Introduction

Analysis of surfaces and interfaces was revolutionized in the 1980s by the development of scanning probe microscopy methods that enabled characterization of surface topography and electronic structure down to the nanometer (and in some cases atomic) scale [18, 44–46]. The first laboratory demonstration of the scanning tunneling microscope (STM) was reported in 1982 by Binnig and Rohrer [47, 48]. The following year, the same group used the microscope to resolve the spontaneous restructuring of a silicon crystal surface to form a structure known as the Si(111)- $7 \times 7$  reconstruction [49]. Previously, it had not been possible to experimentally distinguish between the multiple possible surface structures; this was an important problem since surface structure impacts reactivity in solid-state materials [50]. With this new analytical technique, the surface structure of Si and other conducting and semiconducting materials [51, 52] could be observed directly in real-space. Soon afterward, in 1986, the first atomic force microscope (AFM) was reported by Binnig and Quate [53], opening the additional possibility of imaging on non-conductive surfaces.

In the intervening years, both techniques have matured [18, 19], facilitating surface analysis for a broad range of applications [20, 21], including single-molecule measurements [54]. Scanning tunneling microscopy has been applied not only to characterize

ordering in self-assembled monolayers of organic molecules, but also to control the interface and to observe dynamics. For instance, the STM tip has been used to initiate surface-templated polymerization reactions with molecules including diacetylenes [14], creating conductive molecular wires, and to observe directly the isomerization of functionalized azobenzenes on surfaces [55–58]. The complexity of molecules that can be analyzed using the STM has also increased, with a growing number of applications to biomolecular structures such as amyloid peptides associated with Parkinson’s and other neurodegenerative diseases [59–61].

Simultaneously, advances in AFM instrumentation have both dramatically improved resolution and imaging speed, and further expanded the types of samples that can be analyzed. Development of liquid and low-force imaging techniques have made it possible to image delicate samples including membrane proteins embedded in a lipid bilayer [62–64]. Highspeed (in some cases video-rate or faster) imaging has opened the possibility of imaging dynamic processes on surfaces, including the rotation of the F1-ATPase [65–68]. Atomic-resolution imaging has even proven possible for selected samples including large aromatic molecules such as pentacene on a NaCl bilayer on Cu(111) [69, 70].

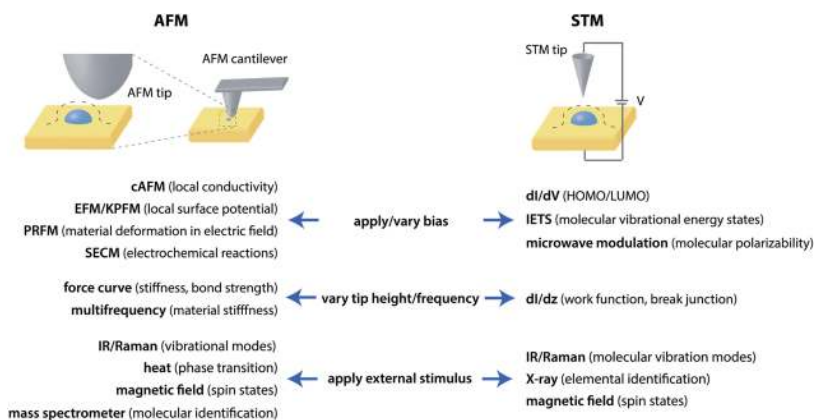


Figure 1.1. Overview of multimodal AFM and STM techniques incorporating: (1) an applied bias, (2) modulation of tip position (height or tapping frequency), or (3) an external stimulus or colocalized measurement modality.

As scanning probe methods have become more robust and widely applied, a growing community of researchers has sought to broaden the imaging capabilities of scanning probe microscopy to provide not just topographical, but also detailed chemical information about interfaces at these length scales Figure 1.1. This can be achieved either by modulating a parameter of the scanning probe experiment itself (for instance the voltage in an STM experiment, or the frequency of the AFM cantilever vibration), or by introducing an external stimulus such as IR radiation or a magnetic field. Multimodal information can also be acquired by co-localizing a second imaging modality, such as mass spectrometry imaging, with the scanning probe.

Here, we provide a tutorial review describing developments in the field of multimodal scanning probe microscopy, highlighting both foundational work and recent advances that have facilitated applications ranging from studies of biological structure and function to streamlined development of material electronic and mechanical properties for renewable energy. We present examples of both widely used techniques that are commonly available in shared user facilities in large academic research institutions, as well as cutting-edge techniques that are less commonly available but provide new types of nanoscale structural information. Since atomic force microscopy is the more broadly used technique in the analytical chemistry community, we begin by discussing multimodal AFM and its applications in characterizing materials, then address multimodal STM techniques for probing molecular properties at interfaces. We close by offering perspectives on future opportunities for both research areas.

## 1.2 Multimodal Atomic Force Microscopy

In a standard atomic force microscopy experiment, a sharp tip (often Si, with radius of curvature  $<10$  nm) mounted on a cantilever is rastered across the sample to measure surface topography. A laser beam is reflected from the back of the cantilever to a quadrant photodiode, and the position of the beam on the photodiode is used to track changes in the vertical position of the tip as it tracks the surface topography.

In contact mode, the tip touches the surface, which is experimentally straightforward and provides good spatial resolution (on the order of 1 nm lateral, 0.1 nm vertical). For typical contact mode imaging in air, forces applied to the sample by the tip may be in the range from 10–100 nN, which can damage soft materials. Such materials can instead be imaged using a soft cantilever that applies forces on the order of 100 pN [71], or using tapping or non-contact modes. In tapping mode, the AFM tip is held a small distance (a few nm) from the surface, and the cantilever is oscillated using an AC voltage applied to a piezoelectric actuator. These small oscillations (<10 nm) bring the end of the tip close enough to the sample to experience repulsive or attractive van der Waals and/or electrostatic interactions that modify the resonance amplitude or frequency. In addition to vertical deflection, lateral tip deflection can also be detected at the photodiode. This provides a readout of the strength of frictional forces between the tip and the surface [72,73], which can vary with surface chemical composition (for instance, with the terminal functional group in an alkanethiol SAM).

While contact and tapping mode have historically been the most common imaging options in commercial AFMs, in recent years additional imaging modes have proliferated due to the wide interest in mapping nanoscale surface properties. Here, we focus on methods that provide multiple types of information about the molecule or material in the probe-sample junction. We group these measurements into three broad classes: (1) applying or varying a bias between the tip and the sample to measure electrical properties, (2) modulating vertical tip position, generally used in measuring Young’s modulus, adhesive forces, and other mechanical properties important in biological and polymeric materials, and (3) adding an external stimulus such as IR or visible light, an ion beam, or a magnetic field, in order to correlate topography with the presence of chemical bonds, particular molecular species, or local magnetic properties.

### 1.2.1 Bias Application and/or Modulation (cAFM, EFM, KPFM, PRFM)

For energy applications, it is frequently useful to measure electronic transport and dielectric polarization properties at the nanoscale, since device performance is tied to local variations in these parameters [74, 75]. For instance, organic photovoltaic devices are often based on an interpenetrating network of two organic materials, one that is an electron conductor and one that is a hole (positive charge) conductor. Phase segregation of the materials on the 10–100 nm scale is desirable to promote efficient separation of excitons into unpaired electrons and holes when the device absorbs photons [75]. However, topographic measurements alone are insufficient to assess this behavior and associated variations in local transport properties. Thus, probing variations in conductivity, illuminated photocurrent and work function on the sub-100 nm scale using multimodal AFM is valuable in correlating device performance with domain structure to increase reproducibility. Several related but distinct methods are used to characterize these properties, broadly based on applying a DC and/or AC bias between the AFM cantilever tip and the substrate [19, 20, 76, 77].

#### *Conductive AFM, Electrostatic Force Microscopy and Kelvin Probe Force Microscopy*

Local variations in charge transport and electron and hole injection in materials for photovoltaic and other devices can be measured simultaneously with local topography using cAFM [18, 76, 78]. In this configuration, a conductive (usually metal-coated) AFM tip is rastered across the substrate in contact mode as a bias is applied. The current through the sample (pA to nA) is monitored to create a conductivity map, while tip deflection is measured in the standard way to create a topographic map. Because the measurement is made in contact mode, care must be taken not to damage soft materials such as polymers, and tip lifetime is limited as the metal coating can be abraded by the surface. Lower contact forces are less likely to cause sample damage, but can lead to less stable electrical contact, so this parameter must be optimized for

each system. Conductive AFM imaging has been used to observe the evolution of local conductivity networks in both electrode materials and polymer blends for solar cells as they are subjected to a variety of processing steps including chemical etching and thermal annealing [78–81]. For instance, Ginger and coworkers found that in poly(3,4-ethylenedioxythiophene) polystyrenesulfonate (PEDOT:PSS) thin films, frequently used as anode materials, relatively small 20 nm conductive domains were initially observed throughout the film by cAFM. The density of these conductive domains increased both with thermal annealing and with decreased PSS concentrations, and overall film conductivity increased after washing with chlorobenzene, highlighting the importance of controlling all aspects of film processing [79].

Local variations in surface work function, or surface potential, can impact the voltage necessary for charge injection and extraction at electrode contacts in a photovoltaic device. Lateral variations in work function are also important in field effect transistors, in which the potential drops between the source and drain electrodes.

Local surface potential may be characterized using electrostatic force microscopy (EFM) [82] or Kelvin probe force microscopy (KPFM) (Fig.1.2) [76, 83]. In both EFM and KPFM, the tip is usually first rastered across the surface in tapping mode to measure topography. To measure surface potential, the tip is then retracted slightly from the surface and a bias is applied for further imaging. At the smaller tip-sample separations (a few nm) used for topographic imaging, van der Waals forces ( $\propto z^{-6}$ ) dominate tip-sample interactions. At the larger separation distance (typically  $>10$  nm), coulombic forces ( $\propto z^{-2}$ ) instead dominate, allowing them to be imaged independently from topography. Coulombic forces arise based on the difference in the work functions of the tip and sample materials, known as the contact potential difference (CPD). If there is a nonzero contact potential difference between the tip and the sample, and the two are connected through an external circuit, electrons will flow into the material with the larger work function until the Fermi levels are equal. This local charging effect produces coulombic forces between the tip and the sample; tip deflection due to these forces can be measured in the standard way, based on the

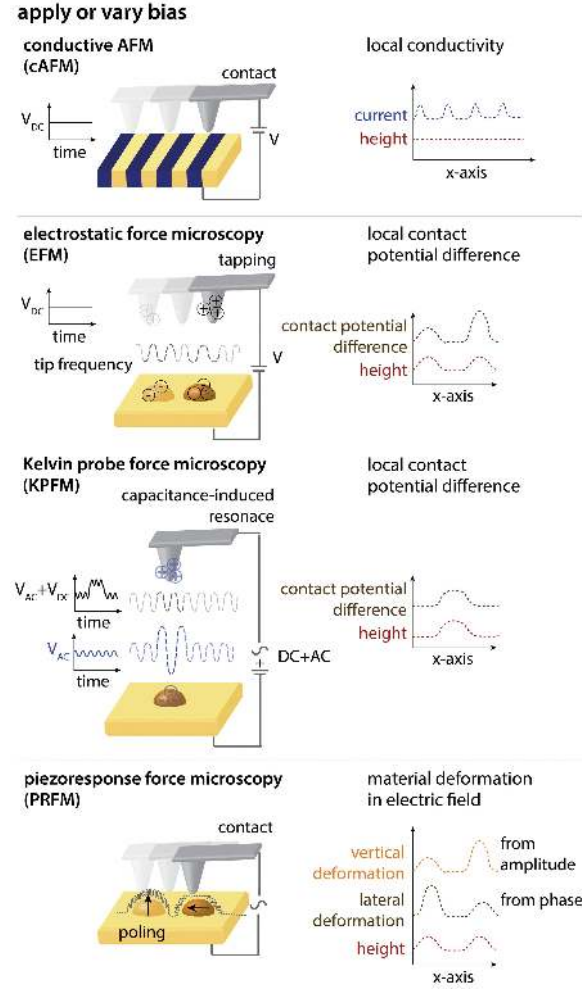


Figure 1.2. Multimodal AFM with constant or variable bias probes local electronic properties including conductivity, local surface potential, or local piezoelectric effects.

position of the laser beam on the detector photodiode. An additional bias is usually applied to the tip to further control the total potential difference and improve sensitivity. While both EFM and KPFM measure surface potential based on such local capacitive effects, they use somewhat different bias and measurement schemes, described below.

In EFM, the tip rasters above the surface in tapping mode with a constant applied bias [82]. Changes in surface potential vary the tip-sample forces, producing a

shift in the tip resonance frequency proportional to the contact potential difference. Attractive forces slightly decrease the tip oscillation frequency, while repulsive forces increase it; this may be detected either directly, or based on a phase shift in the oscillation.

One important application of EFM was in early studies of semiconductor nanocrystals, which were known to exhibit photoluminescence intermittency or blinking behavior, believed to be associated with photoionization. Brus and coworkers, using EFM imaging, demonstrated that in small ( $\sim 5$  nm) CdSe nanocrystals, roughly half the particles carried a positive charge under ambient conditions. The charged fraction increased substantially when the particles were illuminated, then decreased again when the particles were no longer illuminated [84, 85]. Understanding and controlling this type of photophysical behavior is important in using nanocrystals for photovoltaic and other material applications. More recently, EFM has also played a role in characterizing layered materials for devices, including characterizing metal-semiconductor contact between ZnO and graphene for a transparent, flexible field emission device [86], and observing electric field screening of substrate charges by individual MoS<sub>2</sub> sheets [87].

In contrast with EFM, KPFM applies a dynamic DC bias to equalize the potential of the surface and the tip. The tip is not mechanically excited, but an AC bias is applied near the tip resonant frequency. This produces oscillating capacitive charges on the tip and sample, exerting electrostatic forces that cause the tip to begin to oscillate. The magnitude of the tip oscillation at the AC frequency is proportional to the tip-surface potential difference. Applying a DC offset bias equal to the contact potential difference equalizes the tip and surface potentials, minimizing the tip oscillation. Therefore, as the tip rasters across the surface, a feedback loop adjusts the DC offset dynamically to minimize tip oscillation, and the required bias is recorded as the local CPD.

Since the CPD mapped by KPFM equals the difference between the tip and local sample work functions, it can then be used to extract the local sample work function.



This requires the tip to be calibrated against a reference material (such as a sputtered thin film of Au, or freshly cleaved HOPG) with a known work function. Importantly, when working with materials under ambient conditions, surface contaminants can alter the work functions of metals (including the tip) by 0.5–1.0 eV, and can introduce surface states and oxides on semiconductor surfaces, also changing measured CPD values [22]. Thus KPFM measurements are frequently performed under UHV conditions when possible.

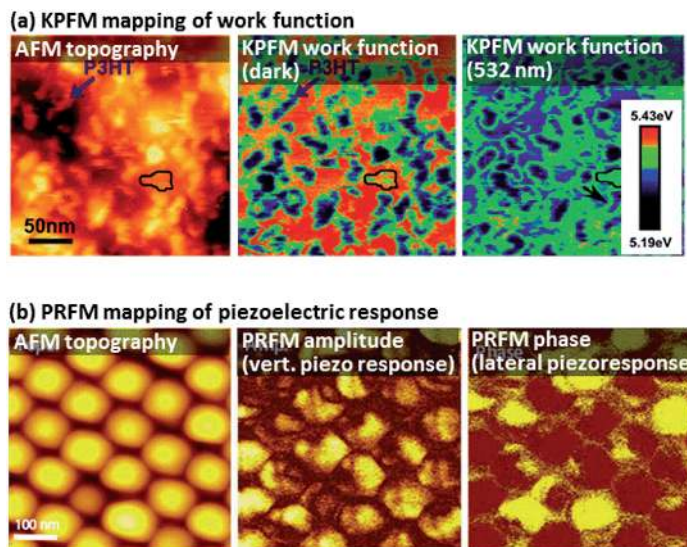


Figure 1.3. Multimodal AFM with applied bias. (a) AFM topography and KPFM images of a polymer blend film both unilluminated (middle) and illuminated (right), showing the change in work function for individual polymer domains. (b) AFM topography and PRFM amplitude and phase of a nanostructured ferroelectric material, showing differences in poling directions in individual domains. Adapted with permission from ref. [88] and [89]. Copyright 2010 American Chemical Society and 2013 John Wiley and Sons.

Similarly, KPFM has been utilized in examining contact potentials in organic materials for devices, as well as in biological systems [83]. Organic-inorganic contacts between electrodes and active layers in polymer devices represent an important nanoscale chemical characterization target, since high resistance contacts between materials with different work functions can dominate device performance. Friend and

coworkers examined potential drops in poly(3-hexyl thiophene) (P3HT) transistors at source and drain contacts, finding that KPFM can be used to measure the potential in the accumulation layer [90]. They were also able to use KPFM to screen for electrode/polymer material pairs that produce contact resistances of less than  $50\ \Omega$  at the source electrode, improving device performance in polymer FETs [91]. More recently, Spadafora, Grévin and coworkers used a modified noncontact AFM/KPFM detection scheme incorporating damping contrast, in order to achieve sub-10 nm resolution in KPFM measurements of a P3HT/phenyl-C61-butyric acid methyl ester (PCBM) blend film [88]. Fig.1.3a shows nanometerscale images of the surface work function of the film, which changes in a spatially heterogeneous manner when the film is illuminated with 532 nm radiation. An important aspect of this tandem characterization of topography and electronic properties has been the discovery that nanoscale topographic peaks do not necessarily correlate with local peaks in film conductivity, highlighting the necessity of characterizing both parameters [92]. In addition to measurements of organic and inorganic films, KPFM has also been utilized to study charge transfer in biological systems, including photosystem [18], quantifying the potential of the electron receptor system [93].

### ***Scanning Capacitance Microscopy***

Semiconductor conductivity is often controlled by the addition of a small number of dopant atoms (on the order of 1 in  $10^6$ ), containing either more or less valence electrons than the intrinsic semiconductor. Controlling the spatial distribution of dopants is important in reproducible device manufacturing [94]. Because intrinsic semiconductors such as Si and Ge form a surface layer of native oxide when exposed to air, it may be necessary to measure very small subsurface dopant concentrations through this layer of insulating material.

Scanning capacitance microscopy (SCM) was originally developed at RCA in the 1980s [95] and rapidly adapted to work with atomic force microscopes [96]. In this

method, a metal tip is rastered in contact mode on an insulating oxide layer over a semiconductor, as an AC bias is applied ( $\sim 10$  kHz). As in the EFM and KPFM measurements described above, this produces capacitive charge accumulation in the semiconductor; however, charging in this case is limited by the dopant concentration, making it possible to measure the local dopant concentration, if very small capacitances ( $< 10^{-18}$  farad) can be detected. This is achieved by measuring dynamic capacitance changes, which are easier to detect than small static capacitances. When a highfrequency (GHz) capacitive sensor is used to detect the accumulation and depletion of charge with each cycle, SCM can detect capacitances as low as  $10^{-21}$  farad, registering dopant densities from  $2 \times 10^{14} \text{cm}^{-3}$  to  $8 \times 10^{19} \text{cm}^{-3}$  [97]. Related microwave-frequency AFM methods have more recently been used to probe polarization in other insulating materials including peptide maquettes with a zinc(II) protoporphyrin IX center at electrode interfaces relevant for optoelectronic devices, mapping changes in nanoscale impedance as the films are optically excited at 425 nm [98].

### ***Piezoresponse Force Microscopy***

Many materials important for both energy and biological applications have a non-centrosymmetric crystal structure (one that lacks a center of inversion symmetry), and therefore exhibit a property known as piezoelectricity [99]. When piezoelectric materials are placed in an electric field, they expand or contract slightly along the axes of dipoles in their unit cells. Such deformations are typically quite small—piezoelectric coefficients for highly responsive lead zirconate titanate ceramics used as actuators (such as those used to control scanning probe tips) are on the order of  $300\text{--}600 \text{ pm } V^{-1}$ . However, much smaller responses can also be useful: for instance, many sensors are based on the piezoelectric properties of quartz, which has a response of just  $2.3 \text{ pm } V^{-1}$  [100]. Many biomolecules containing helical motifs are also piezoelectric. Bone, a mixture of the helical protein collagen and inorganic crystalline

hydroxyapatite [101], is piezoactive due to its collagen content, which is believed to be important in its mineralization process [102].

Piezoresponse force microscopy is a contact modality that measures the mechanical deformation of piezoelectric materials in response to an AC electric field applied through the tip [77, 103]. As the bias at the tip oscillates, the piezoelectric material expands and contracts slightly under the tip; this causes the tip to deflect, following the motion of the sample. Sensitive detection of tip deflection is required in order to track the small motions being measured. Because ferroelectric materials exhibit piezoelectric responses, PRFM has been used to probe both static and dynamic poling of domains in ferroelectric films [104, 105], as well as changes in inorganic structure, including mapping lithium ion diffusion in a battery cathode [106]. Fig.1.3b shows AFM topography and PRFM surface displacement maps for nanoscale islands of ferroelectric  $\text{BiFeO}_3$  on  $\text{SrRuO}_3/\text{SrTiO}_3$  [89], a material of interest for nanoscale non-volatile memory applications. Peaks in the PRFM amplitude correspond to a vertical voltage-induced deformation of the material, while peaks in PRFM phase indicate lateral deformation. In the case shown here, application of a higher poling voltage to switch the ferroelectric domain orientation also resulted in switching of diode-like conductive direction in the material, as measured by conductive AFM, with rectification ratios as high as 500 at  $\pm 0.6$  V. Even weakly piezoactive materials such as collagen can be characterized by PRFM [107–109]. For example, measurements of tooth dentin have been used to elucidate collagen fibril ordering in the enamel with sub-10 nm resolution [109].

### ***Scanning Electrochemical Microscopy***

Electrochemical reactions are central to fuel cells and batteries, as well as biological energy generation and metabolism. Performing an AFM bias experiment in liquid with a specialized tip, it is possible to probe local variations in electrochemical processes, referred to as scanning electrochemical microscopy AFM (SECM-AFM) [110].

The scanning electrochemical microscopy (SECM) technique, developed in 1989 by Bard and coworkers [111], utilizes an ultramicroelectrode (UME) to limit the spatial extent of the electrochemical reaction. Typically, the UME is based on a Pt or Au wire, or carbon fiber with a diameter from a few  $\mu\text{m}$  to as little as 10 nm. The body of the wire is sealed in an insulator such as glass or Apiezon wax to localize the electrochemical reaction to the exposed tip [112]. Integrating SECM into an AFM improves positioning feedback for the ultramicroelectrode [113,114], but levies additional requirements on the probe tip since it must be mounted on a cantilever. UME-AFM probes have been fabricated using a number of strategies, for instance by insulating a commercial conductive AFM probe with a material such as parylene, followed by mechanical abrasion or focused ion beam (FIB) processing to remove the insulating layer at the probe tip on [113–118].

The tip is then immersed in an electrochemical cell and acts as the working electrode, which can be moved precisely relative to the sample as a bipotentiostat controls the bias of the tip and/or substrate relative to a reference electrode. Electrochemical oxidation or reduction of species from solution at the tip results in a small current (pA–nA), which increases based on the solution concentration of the molecule. If the reactive molecule is being generated by the substrate, the current is limited by the diffusion of the molecule from the substrate to the tip, and increases as the tip approaches the surface. Other surface features such as proteins, nanoparticles, or micro- or nanoscale pores in a membrane may also act as sources for the electrochemically active species [114]. Due to the more complex probe structure and the fact that electron transport occurs through Faradaic currents in the liquid medium, this experiment provides nm-scale vertical resolution, but substantially lower lateral resolution (typically  $> 100$  nm) than standard AFM experiments. SECM-AFM has been used to probe diverse processes in which precise z-resolution and operation in solution are critical, including the dissolution of crystals [113], localized corrosion [119] and enzymatic activity [115,116], and transport through micropores [118].

### 1.2.2 Tip Height and Rotation Modulation (Force Curves and Multifrequency AFM)

Many soft materials including polymers and biomolecules are soft enough to be deformed by interactions with the AFM tip, which can be used to study mechanical properties often integral to their function. Here, we begin by describing force curve measurements, in which the AFM tip is pressed into or pulled away from the surface, to measure local hardness and adhesive forces. Second, we discuss tapping mode experiments in which higher harmonics (or other frequencies) are excited to measure surface mechanical properties simultaneously with topography.

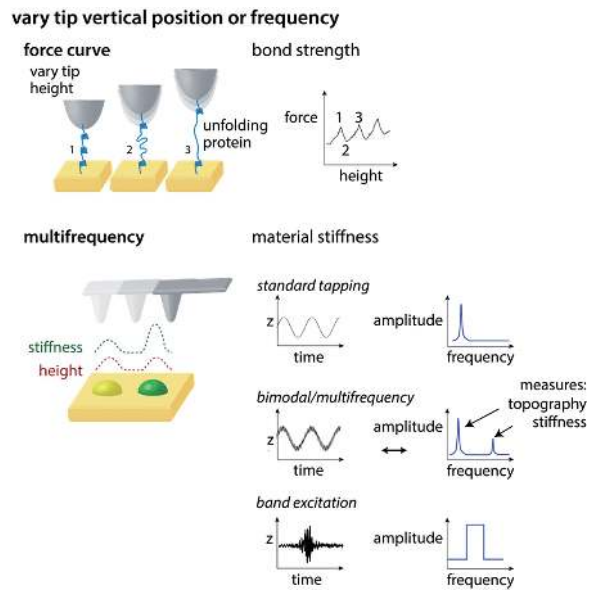


Figure 1.4. Multimodal AFM with varied tip vertical position measures local mechanical properties including Young's modulus and elasticity.

#### *AFM Force Curve Measurements*

Measuring tip deflection as the tip height is decreased or increased relative to the surface creates a force curve (Fig.1.4) [120–122]. As the tip height is decreased,

repulsive forces with the surface begin to cause the end of the cantilever to deflect upward. Force curves can be used to calculate elastic moduli for soft materials, and have been used extensively in characterizing the properties of polymers [123–125]. For instance, cartilage has a hierarchical structure, and different mechanical parameters were found in AFM indentation measurements based on tip contact area [126]. Sharp pyramidal AFM tips (radius  $\sim 20$  nm) measured a 100-fold lower elastic modulus than larger spherical indenter tips (radius  $\sim 2.5$   $\mu\text{m}$ ), suggesting that the individual collagen fibrils are softer than the collagen structure at the micrometer scale. Recently, advances in instrument design have enabled force curves to be collected in an automated fashion at each point to create an image of surface mechanical properties, a capability that is now available on some commercial instruments.

Conversely, the tip can be used to measure mechanical behavior of single molecules, including the strength of noncovalent interactions within the molecule. If a macromolecule such as a protein is covalently bound to both a surface and an AFM tip (frequently through thiol-Au linkages), noncovalent and/or covalent forces within the macromolecule will resist the retraction of the tip from the surface, causing the cantilever to deflect downward [64, 127, 128]. Fig. 1.5a shows force curves acquired during the unfolding of domains in titin muscle protein. As the tip is withdrawn from the surface, the force on the tip increases (point 1) until a domain unravels (point 2), decreasing the pulling force and forming a sawtooth pattern with a periodicity of 25–28 nm between peaks, consistent with the length of an extended titin Ig domain. Forces are calculated based on tip deflection, using a calibrated tip; the force required to overcome intermolecular forces within the domain varied from 150 to 300 pN with greater forces required at faster pulling speeds (with a range from 0.01–1  $\mu\text{m s}^{-1}$ ).

### ***AFM Molecular Recognition Measurements***

In many cases in biology, the strength of the interaction between a pair of molecules is of interest, and this interaction can also be probed directly with the AFM [130–133].

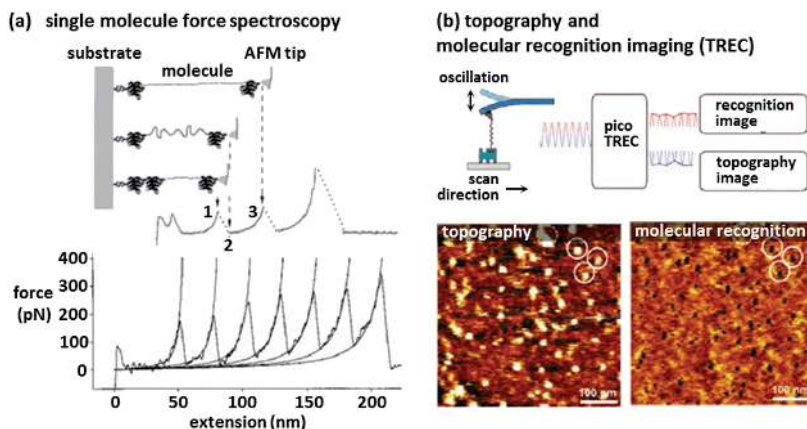


Figure 1.5. Examples of single-molecule force curves and molecular recognition imaging. (a) Single-molecular force spectroscopy experiment measuring forces required to unfold individual subunits of titin protein. (b) Simultaneously acquired topography and molecular recognition imaging of a biotin-functionalized tip interacting with an avidin-functionalized surface. Avidin molecules appear as protrusions in the topography image, and as depressions in the recognition image. Adapted with permission from ref. [127] and [129]. Copyright 1997 AAAS and 2005 John Wiley and Sons.

In this case, the AFM tip is functionalized with one binding partner, and the surface with the other. This configuration has been used to detect ligand-receptor binding events [134], antibody-antigen recognition events [130], and the hybridization of DNA [135]. For example, AFM recognition experiments have helped to distinguish multiple types of binding between cadherin proteins that dimerize during cell surface adhesion [136]. Bringing a cadherin-functionalized tip into contact with a lipid-coated surface containing complementary cadherins, recognition dynamics could be probed as controlled pulling forces were applied. The ability to apply controlled forces during the experiment helped mimic biological conditions as cells migrate, and suggested that initially cells form catch bonds, which become stronger when pulled, making them robust during migration. Over time, the cadherin dimers relax into more permanent slip-bond structures that are strongest in the absence of stress. In performing such experiments with functionalized tips, control over the orientation and binding density of



the functional partner on the tip are critical in ensuring reproducible measurements, as is control over sample hydration and tip pulling speed [137].

It is also possible to simultaneously map both surface topography and molecular recognition using an imaging scheme in which a molecular recognition event creates attractive forces that decrease the oscillation amplitude of a probe scanning the surface in tapping mode [137]. In the experiment shown in Fig.1.5b [129], biotin is affixed to the AFM tip through a flexible poly(ethylene glycol) (PEG) linker, and used to probe an avidin-coated surface. As the tip rasters across the surface, the lower and upper halves of the oscillation are analyzed separately to create two images. The lower oscillation magnitude decreases as the tip rasters over an avidin molecule (or any surface protrusion), due to the higher surface topography. This half of the oscillation is used to control the tip Z height to maintain a set point oscillation amplitude as in standard AFM tapping mode imaging. In contrast with other types of surface protrusions, when the biotin-PEG-functionalized tip rasters over an avidin molecule, the binding interaction limits the magnitude of the upswing of the cantilever. Therefore, the upper half of the oscillation can be used to image molecular recognition; avidin molecules appear as depressions in the molecular recognition image constructed from the maxima of each oscillation.

### ***Multifrequency AFM Measurements***

When imaging samples in tapping mode, multifrequency AFM measurements can be used to examine local topography and mechanical properties (e.g. Young's modulus) simultaneously [138–140]. In standard tapping mode imaging, the cantilever is driven near the frequency of its first bending mode. However, higher harmonics of the cantilever can be excited simultaneously, leading to nonlinear tip-sample interactions that change with sample stiffness [138,140]. Higher harmonic excitations are typically much smaller in magnitude ( $< 1$  nm, vs. 1–10 nm first-harmonic oscillations), making

them more congruent with the decay length of tip-surface interaction forces ( $\sim 0.5$  nm) [141].

To some extent, higher harmonics are naturally excited as a consequence of driving the tip at its first eigenmode, or resonance frequency. Tip deflection at higher frequencies can be recorded along with the primary tip excitation frequency, referred to as multiharmonic AFM imaging. However, harmonic amplitude decreases with  $n^2$ , necessitating sensitive detection methods for higher harmonics. Such resonances are most often observed with soft cantilevers (force constants  $0.5 \text{ N m}^{-1}$  or less) or when imaging in liquids [142], and have been used to image live bacteria [143, 144] including work by Raman and coworkers mapping nanoscale local mechanical properties of live cells [144]. For instance, using commercial AFM systems and cantilevers, with the cantilever stiffness calibrated based on thermal noise, multiharmonic measurements were used to differentiate mechanical properties of cells including rat fibroblasts and red blood cells. Red blood cells contained a relatively stiff center region (with  $k_{\text{sample}} \sim 0.05 \text{ N m}^{-1}$ ) and a softer periphery ( $k_{\text{sample}} < 0.01 \text{ N m}^{-1}$ ), enabling the cells to deform as needed when passing through blood vessels. Rat fibroblasts were stiffer overall than red blood cells, and could be described in terms of Hertzian mechanics, leading to local measured stiffnesses of 30–80 kPa, with clear differences in mechanical properties corresponding to nucleus, cytoskeleton, and actin fibers.

It is also possible to excite the cantilever at multiple frequencies directly, increasing oscillation amplitude at the higher frequencies [139]. Simultaneous excitation of both first and second resonant frequencies, referred to as bimodal AFM [145], has been used to map local dissipation and stiffness in conjunction with topography in soft materials including proteins. For instance, phase shifts in the second flexural mode (2nd harmonic) have been used to detect the presence or absence of 5 nm magnetic iron oxide nanoparticles inside a peptide shell, distinguishing between ferritin and apoferritin proteins with similar topography (Fig.1.6a) [146]. The method has also been used to map protein structural flexibility in antibodies, providing sub-2 nm spatial resolution in liquid, using forces as small as 30–40 pN. Elastic modulus variations were observed

across a single antibody, from 8 MPa at the end of the arm to as high as 18 MPa at the central protrusion [147]. When multiple modes are excited, it is also possible to detect at an intermodulation frequency—for instance, the difference between the two frequencies—which can decrease the required detection bandwidth [148, 149], or at one or more off-resonance frequencies, which can increase sensitivity [150]. Alternatively, it is possible to perform broadband excitation of the cantilever and detect amplitude or phase shifts throughout the range of frequencies to determine multiple mechanical or frequency-dependent properties, simultaneously [151]. The technique has been applied to both so and inorganic materials, distinguishing between damping, Young’s modulus, and electromechanical properties in biomaterials, and assessing ion migration in a lithium ion battery cathode with 100 nm resolution [106]. In these experiments, grains of  $\text{LiCoO}_2$  with different orientations relative to the imaging plane exhibited enhanced displacement at a range of resonant frequencies from 360 to 400 kHz, corresponding to different local out-of-plane Young’s moduli.

### ***Non-Longitudinal Bending Modes***

Although longitudinal bending modes of the cantilever are usually excited for imaging, other types of deflection can also be used to image mechanical properties of the sample including stiffness. For example, torsional deflection across the short axis of the cantilever can be measured, known as lateral force microscopy (LFM), which measures frictional forces as the tip rasters the surface. Whitesides and coworkers used this technique in early experiments demonstrating the ability to differentiate between nanoscale areas of a chemically patterned surface containing areas of both methyl-terminated alkanethiols and carboxylic acid-terminated alkanethiols on Au(111) [73]. Carboxylic acid-terminated areas of the surface exhibited greater lateral deflection of the AFM tip characteristic of higher frictional forces.

Torsional *resonances* can also be excited in tapping mode (in contrast to static torsional deflections due to frictional forces with the surface). Such resonances can be

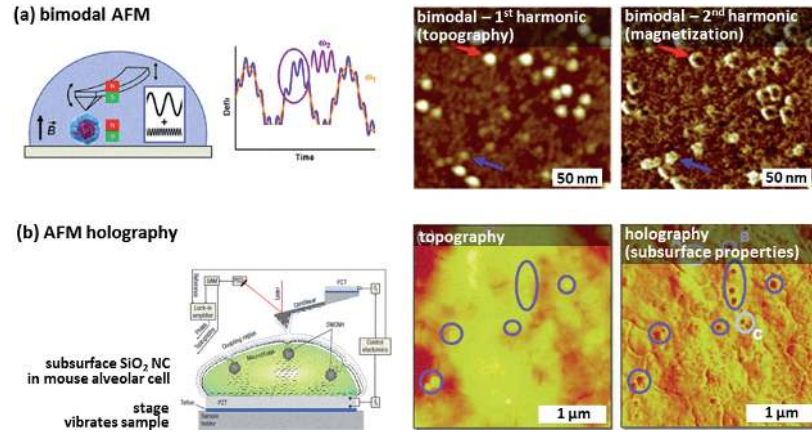


Figure 1.6. Examples of multimodal AFM exciting multiple resonant frequencies. (a) Bimodal AFM exciting both first and second cantilever harmonics to image ferritin proteins with and without iron oxide nanoparticle cores. First harmonic image reveals surface topography, while second harmonic provides contrast showing the presence or absence of the magnetic nanoparticle within the protein. (b) AFM holography reveals subsurface features with different mechanical properties by applying vibrations to the sample, and detecting transmission of the vibrations to the tip. Standard AFM image (left) shows surface topography of rat alveolar cells, while holography image (right) reveals the presence of sub-surface silica nanoparticles. Adapted with permission from ref. [152] and [153]. Copyright 2006 National Academy of Sciences and 2008 AIP Publishing LLC.

achieved using a specialized T-shaped tip design in which the AFM tip is positioned off-center near the end of the crossbar. As the tip rasters the surface in tapping mode, longitudinal deflections are used to track surface topography, while torsional deflections vary with surface stiffness. This configuration has been used to characterize local mechanical properties of DNA [154] and proteins [155]. In one such experiment, local stiffness was measured in a microarray of DNA designed to detect differences in microRNA levels corresponding to human colon and bladder tumor cell lines. Measured local stiffness ranged from 5 GPa to 3 GPa depending on the hybridization state of each DNA molecule, making it possible to measure individual hybridization events [154].

In a multimodal AFM technique known as AFM holography, the sample is subjected to vibrations, which are variably damped based on local structure [156,157]. Measuring this local damping using an oscillating cantilever can detect subsurface structural variance in living cells [157,158] or in soft materials [153] with lateral resolution on the 10–100 nm scale and depth resolution for some types of subsurface features. This is significant, since scanning probe methods in general are most sensitive to surface topography and chemistry. Fig.1.6b shows this technique utilized to observe nanoscale silica particles buried in mouse alveolar cells after the mouse was exposed to the particles by inhalation [156]. In this case, the cells were excited using ultrasonic energy at 3.950 MHz, and the AFM cantilever was oscillated at a slightly higher frequency (4.217 MHz); coupling between oscillations created a phase signal revealing locations of subsurface silica particles.

### **1.2.3 Application of External Stimuli (Electromagnetic Radiation, Heating, Mass Spectrometry, Magnetic Fields)**

To extract additional information from samples, scanning probe imaging can be applied in tandem with or colocalized with another modality. One important example is the measurement of photoconductance in thin films using cAFM while the film is irradiated with visible light, as discussed in the section on electrical measurements. Here, we will discuss four additional applications. First, we discuss the incorporation of Raman or IR spectroscopy in combination with a scanning probe to characterize local chemistry simultaneously with topography. These methods are useful for detecting defects in carbon nanomaterials for energy applications, as well as local variations in peptide structures. Second, magnetic fields can be applied in tandem with scanning probes to characterize magnetic domain structure (useful in nanoscale memory applications) and electron and nuclear spin (for both inorganic and soft/biological materials). Third, local sample heating using a scanning probe can be utilized to characterize local phase transitions in polymers for energy applications.

Finally, we discuss performing co-localized mass spectrometry imaging to correlate topographic features with the presence of species with characteristic masses, useful for both polymeric and biological materials.

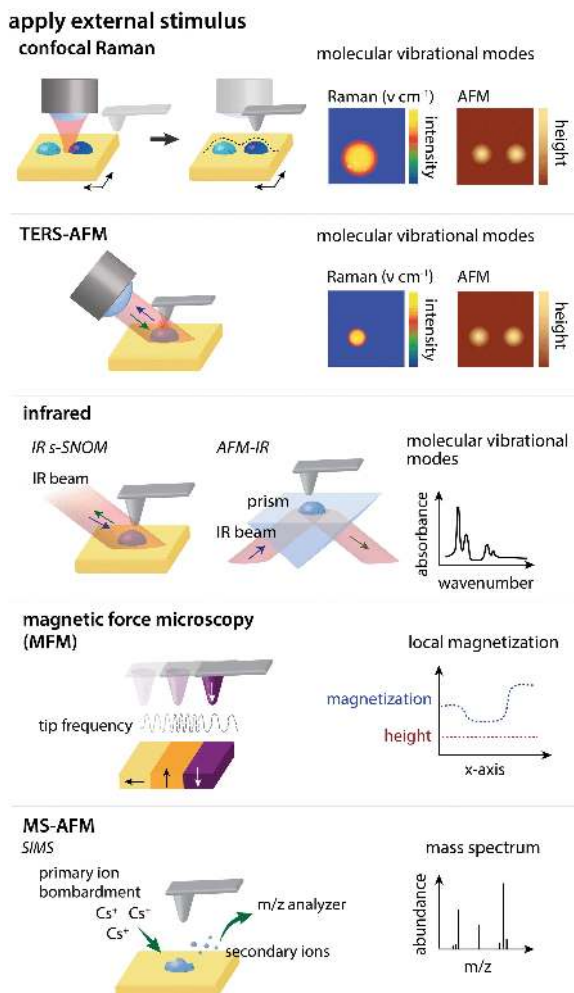


Figure 1.7. Multimodal AFM incorporating external stimuli or a co-localized measurement modality can be used to collect local information about the presence of specific chemical bonds, chemical species with specific masses, local phase transition temperatures, or thermal expansion.

### *Raman and Infrared Spectroscopy with AFM*

Combining Raman or IR spectroscopy with scanning probe microscopy offers the possibility of locally probing both topography and chemical structure (Fig.1.7 [159–162]). Perhaps the most widely used commercial capability integrates a confocal Raman microscope with a standard AFM, performing the two measurements in sequence to acquire surface topography at nanometer resolution in conjunction with diffraction-limited Raman spectra. This capability has been widely utilized to probe the structure of single- and multi-layer graphene as well as microcrystalline inorganic materials. Fig.1.8 shows a bilayer graphene nanoribbon created from a plasma-etched carbon nanotube imaged by AFM and confocal Raman microscopy in the graphene G band ( $1582\text{ cm}^{-1}$ ) [163]. Full spectra acquired over the nanoribbon (right) reveal a broadened 2D peak ( $\sim 2700\text{ cm}^{-1}$ , inset) characteristic of an AB-stacked bilayer structure, which chemically differentiated it from other imaged nanoribbons with narrow 2D bands characteristic of monolayer graphene.

Although Raman spectroscopy on graphene is relatively straightforward due to its large scattering cross-section, most molecules scatter more weakly (1 in  $10^6$  photons is common), and are more difficult to image in nanometer-thick films. Additionally, for some applications it is desirable to resolve features below the diffraction limit. In tip-enhanced Raman spectroscopy (TERS), a noble metal AFM or STM tip can be utilized to create a large local electric field gradient that enhances Raman scattering; when a metal tip is used to image samples on a metal surface, the field in the gap can produce Raman enhancement factors up to  $10^8$ , sufficient to detect an individual molecule or nanostructure with a large Raman scattering cross-section. Although AFM-TERS imaging typically does not provide spatial resolution sufficient to resolve single molecules, it has been applied in characterizing phase-segregated polymer blends on the 10–100 nm scale, as well as performing sub-diffraction imaging of carbon nanotubes. For instance, the chirality of individual carbon nanotubes has been established by AFM-TERS based on differences in radial breathing modes [167, 168].

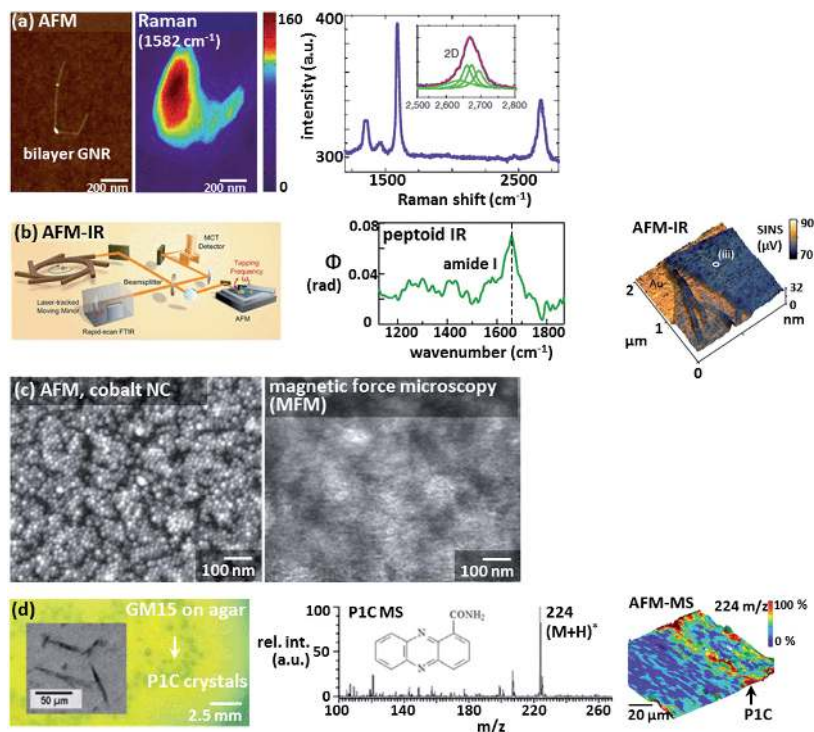


Figure 1.8. Multimodal AFM employing external stimulus. (a) AFM with confocal Raman imaging of a bilayer graphene nanoribbon (GNR). Raman spectrum over GNR shows broadened 2D peak characteristic of bilayer graphene. (b) AFM-IR using synchrotron radiation to illuminate an AFM tip, which provides near-field enhancement. A spectrum collected over a nanoscale area of a peptoid sheet on the substrate exhibits the characteristic peptide amide I band at  $1650\text{ cm}^{-1}$ . Overlaid AFM and IR images provide sub-diffraction localization of the peptoid sheets on the substrate. (c) Colocalized AFM and MFM images of a cobalt nanocrystal film reveal domains  $\sim 100\text{ nm}$  in diameter with shared magnetization. (d) MS-AFM optical micrograph (left) of *Pseudomonas* GM15 colony including crystalline material imaged by AFM-MS. Mass spectrum (middle) of phenazine-1-carboxamide, showing protonated peak at  $m/z\ 224$ . AFM-MS image (right) overlays intensity of peak at  $m/z\ 224$  as a color gradient on the 3D AFM image, providing chemical contrast highlighting the likely locations of P1C crystals. Adapted with permission from ref. [163], [164], [165] and [166]. Copyright 2009 Macmillan Publishers Ltd, 2014 National Academy of Sciences, 2014 American Chemical Society, and 2004 Macmillan Publishers Ltd.



Because tip-enhanced Raman spectroscopy (TERS) can be performed with either STM or AFM tips, with similar experimental considerations, we provide a more extensive discussion of TERS in the STM section.

Infrared radiation is widely used to probe molecular structure due to the diversity of IR-active bonds found in organic materials. However, the relatively long wavelengths (2.5–20  $\mu\text{m}$ ) associated with IR typically restrict the spatial resolution of this information to micron length scales. Utilizing the scanning probe tip either for near-field enhancement [164], similar to TERS, or to track local sample heating and expansion due to IR absorption, provides a means to localize chemical structural information at the sub-100 nm scale, well below the diffraction limit [160]. Fig.1.8b shows the scattering scanning near-field optical microscopy (s-SNOM) configuration, in which a metal-coated AFM tip is used to provide a local field enhancement to localize IR radiation. In the configuration illustrated, synchrotron radiation is used in order to sample across an especially wide range of the IR spectrum. The center panel of Fig.1.8b shows a spectrum taken over a nanoscale spot in a peptoid (poly-Nsubstituted glycine) sheet, revealing the characteristic amide I absorption peak at  $1650\text{ cm}^{-1}$ . Overlaying a 3D AFM topography map of the surface with the scattering intensity at this wavelength reveals the locations of peptoid sheets across the surface. Such measurements are also relevant to inorganic materials—similar scattering geometry utilizing a continuum source was recently used both to launch and detect plasmons in graphene nanoribbons [169].

### ***Magnetic Fields Coupled to AFM***

Magnetic fields can also be applied during imaging to probe local structure [18, 170]. In magnetic force microscopy (MFM), a magnetic tip (frequently silicon coated with FeCr or a similar material) is used to probe the local magnetic domain structure of a sample. Similar to EFM, a common lift-mode imaging scheme involves scanning the surface under conditions typical for AFM topography imaging, then withdrawing

the tip 10–100 nm (to reduce the impact of electrostatic and van der Waals interactions) and re-scanning the surface to produce the magnetic force image. The lift height between passes in this imaging scheme will impact the measured magnetic signal strength—greater lift heights decrease the magnetic signal, but can also increase signal-to-noise ratio for some samples. The technique has been used to image local magnetic structure in a variety of materials, ranging from room-temperature semiconductors [171] to magnetic nanocrystal films [166]. In the case of cobalt nanocrystal films, of interest for ultra-high-density recording media, MFM was used to identify the presence of correlated areas of parallel magnetization  $\sim 100$  nm in diameter, within a film consisting of 12 nm Co particles, and to visualize the evolution in domain structure with consecutive scans (Fig.1.8c).

Magnetic fields can also be applied locally in unconventional ways to provide new types of nanoscale structural information. Magnetic resonance force microscopy (MRFM) [172, 173] aims at providing spatially resolved information on electron or nuclear spins equivalent to a nanoscale version of magnetic resonance imaging. In this technique, a magnetic tip applies a large local magnetic field gradient (on the order of  $10^6 \text{ T m}^{-1}$ ) that, in combination with a strong uniform magnetic field (a few Tesla), creates a region of aligned spins in the sample with a characteristic Larmor frequency that can be detected based on an RF pulse. Single electron spins in inorganic materials such as  $\text{CaF}_2$  have been detected using this methodology [174]. Larger numbers of proton nuclear spins have also been imaged with  $< 25$  nm resolution, sufficient to analyze structure in large biological macromolecules such as tobacco mosaic virus [175].

### ***Local Sample Heating Measurements***

The AFM probe can be used to apply heat as well as to assess phase change temperatures or expansion coefficients in materials such as polymers [176]. Controlled doping of a Si probe can be used to selectively heat the probe tip by increasing the

resistance in that area, localizing heating of the sample to an area roughly 200 nm in diameter [177]. Conversely, for materials with known thermal expansion coefficients, AFM deflection can be used as a readout for the temperature of the sample, known as scanning Joule expansion microscopy (SJEM) [178–180]. For instance, SJEM measurements taken as current flowed through a graphene device revealed small temperature increases at wrinkles, and much larger temperature changes ( $\sim 100$  K) at grain boundaries, which was used to estimate the grain boundary resistivity [179].

### ***Mass Spectrometry Coupled to AFM***

Another avenue for multimodal characterization of local chemical structure is to couple scanning probe imaging with 2D or 3D mass spectrometry imaging (Fig.1.8d) [165, 181–185]. This measurement correlates surface topography with the presence of characteristic mass fragments to identify regions containing molecules of interest on the surface. Two general strategies have been exploited in this regard. One performs the two types of imaging sequentially, imaging surface topography both before and after secondary ion mass spectrometry (SIMS) imaging to enable registration of the two images [183–185]. In one configuration, a small AFM is mounted inside the vacuum chamber of a secondary ion mass spectrometer, with a custom high-precision sample stage that can be rotated  $180^\circ$  to switch between measurement modalities. Spatial resolution for SIMS imaging is as good as 50 nm laterally, and the sample can be maintained under low-temperature vacuum conditions for AFM imaging, removing the possibility of surface remodeling or contamination under changing environmental conditions. The integrated scanning probe also enables surface topography to be scanned after each sputtering pass, meaning that it is possible to compensate for variable sputtering rates for different materials. This method has been used to improve 3D mapping in polymer blend surfaces consisting of poly methyl methacrylate (PMMA)/polystyrene (PS), which erode at very different rates [185].

A second set of strategies couples the scanning probe with the ionization process, collecting information about both surface topography and local chemistry simultaneously. This reduces the challenges in registering the two imaging modalities, while levying additional requirements on the probe or sample. One such approach uses a heated cantilever to locally vaporize analytes from the sample surface, then uses the vacuum draw of an electrospray ionization (ESI) mass analyzer to transport the vaporized sample away from the tip-sample junction [165,181]. This approach has been used to sample the surface of bacteria plated on agar with 2 mm lateral resolution in the MS. Fig.1.8d shows an optical micrograph of the bacterial colony, including crystals of phenazine-1-carboxamide (P1C), a green metabolite characteristic of the *Pseudomonas* GM15 strain. Overlaying 3D AFM topography images with color coding showing the relative intensity of the mass spectral peak at  $m/z$  224 (characteristic of protonated P1C) provides chemical contrast indicating likely locations of P1C crystals across the surface.

### 1.3 Scanning Tunneling Microscopy (STM)

In scanning tunneling microscopy, an atomically sharp metal tip (usually Pt/Ir or W) is raster scanned across a sample at a tip-sample separation less than 1 nm, a distance at which the electronic wave functions of the tip and the sample begin to overlap. When a small positive bias (on the order of 1 V) is applied to the sample, electrons are able to tunnel from occupied electronic states in the tip to empty states in the sample. Conversely, at a negative sample bias, electrons tunnel from occupied sample electronic states to empty tip states. In the commonly used constant-current mode, the contrast of surface features is gauged based on the tip height necessary to maintain a constant tunneling current (pA–nA), which provides sub-nanometer resolution due to the exponential decay of the tunneling probability as the tip-sample distance increases. The STM provides excellent lateral and vertical spatial resolution (often 0.1 nm or better), yet a standard STM image — a convolution of heights and

the local density of states (LDOS) around the Fermi level — is often inadequate to uniquely fingerprint individual molecules on a surface. Therefore, substantial efforts have been made to design additional STM-based modalities that enable extraction of electronic, chemical, and magnetic information from the surface with nanoscale resolution. Three main approaches discussed here are: (1) voltage modulation used to probe electronic or vibrational energy levels of the molecules in the junction, (2) modulation of tip-sample distance, and (3) application of an external stimulus such as light or a magnetic field at the tunneling junction (Fig.1.9).

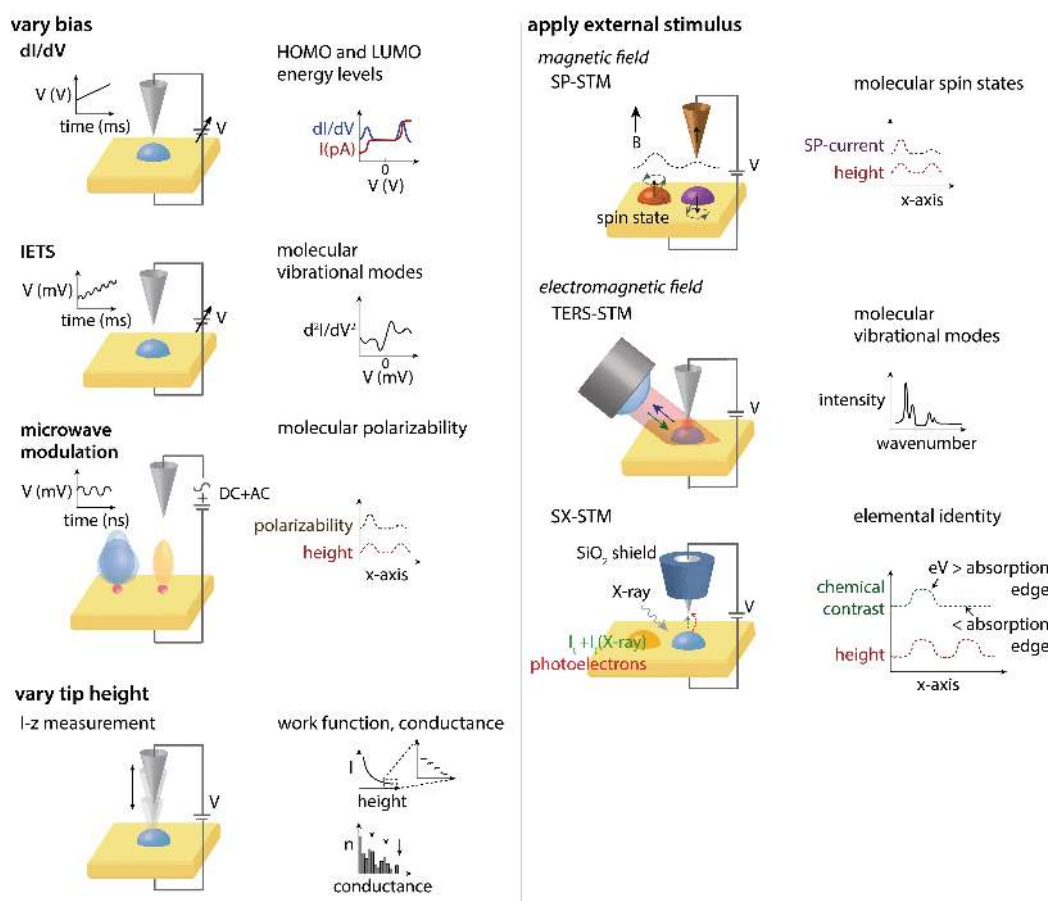


Figure 1.9. Multimodal STM employing bias modulation, tip height modulation, or an external stimulus.

### 1.3.1 Bias modulation ( $dI/dV$ , IETS, and Microwave)

While a standard STM image involves rastering the tip across the sample while maintaining a constant bias, one method for probing molecular electronic structure is to modulate the tip-sample bias (typically within the range of  $-2$  V to  $2$  V) while measuring the tunneling current. This class of measurements is broadly referred to as scanning tunneling spectroscopy (STS) [189,190]. Frequently, STS is performed after taking a standard STM image to identify features of interest and then engaging the tip at a series of desired points; however, it is also possible to perform a spectroscopic measurement at each pixel, given a sufficiently stable instrument [191,192], or to use a high-frequency modulation to collect more targeted electronic information at each point simultaneously with the standard STM image [186].

#### *Differential Conductance Spectrum ( $dI/dV$ )*

Differential conductance measurements can be used to establish the highest occupied molecular orbital (HOMO) and lowest unoccupied molecular orbital (LUMO) levels of molecules at an interface. In this configuration, the tip is held stationary above the surface, and the feedback loop is disengaged to maintain a constant tip-sample distance. The voltage is then ramped linearly through small bias range, on the order of a few volts (Fig.1.10a). The tunneling current is proportional to the number of conductance channels, which increases as more electronic orbitals lie at energy levels suitable for tunneling. This increase in conductance appears as a small step in the  $I$ - $V$  plot (red trace in Fig.1.10a, middle), and as a more noticeable peak in a plot of  $dI/dV$  vs.  $V$  (blue trace). Electronic states involved in tunneling, typically the HOMO and LUMO (separated by a gap of  $\sim 3$  eV in large aromatic molecules), will appear as peaks at energy levels related to the tip-sample bias. This technique is one of the most widely used capabilities of STM and has been used to probe the energy levels in a number of samples ranging from atoms to simple molecules and more complex composite materials [193–198]. Electronic states around the Fermi

level revealed by the  $dI/dV$  spectrum with nanoscale spatial resolution have been particularly useful in characterizing materials for electronic devices. For instance, Wolf et al. examined the electronic structure of colloidal Si nanocrystals (Si-NCs) of varying size and surface functionality, observing doping effects in the Si electronic structure when N-containing functional groups were used as ligands [195].

Electronic energy levels of a molecule adsorbed to a conductive surface often shift due to interactions with the substrate. Obtaining the native electronic structure of a sample can be facilitated using a thin insulator film (e.g. a bilayer of NaCl) to decouple the sample from the conductive substrate. Gerhard Meyer and coworkers have used this strategy to determine HOMO and LUMO energy levels as well as mapping the orbital shapes of pentacene molecules on a bilayer of NaCl on Cu(111) by imaging at the corresponding biases (Fig.1.10a) [187]. Enhanced resolution of the molecular orbital map was achieved with a pentacene functionalized tip. Further experiments also visualized the tautomerization of a molecular switch, naphthalocyanine, whose electronic density shifts with the orientation of the center proton pair [199].

### ***Inelastic Electron Tunneling Spectroscopy (IETS)***

In addition to detecting molecular electronic energy levels, STS can also be used to probe vibrational transitions [200]. Vibrational modes, which normally occur at energies  $< 400$  meV, appear as peaks in the plot of ( $d^2I/dV^2$  vs.  $V$ ) (Fig.1.10b), also referred to as the inelastic electron tunneling spectrum. Unlike conventional vibrational spectroscopic techniques, IETS selection rules have not been fully elucidated, though there is known to be some preference for bonds with dipoles oriented perpendicular to the surface plane [201]. Interpretation of the IET spectrum is somewhat simplified by the fact that vibrational bands are normally only observed at the fundamental frequency [202]. Due to the relatively small vibrational energies being probed, the sample analysis must be performed under vacuum at cryogenic temperatures in order to minimize thermal broadening of vibrational peaks. To increase sensitivity,

a small bias modulation is applied at kHz frequencies on top of the linear bias ramp and detected using a lock-in amplifier. IETS-STM has found many applications in surface chemistry [203–206], inelastic tunneling-induced single molecular manipulation and reactions [207–211], and analysis of molecular structure [188, 212–215]. For instance, an STM tip has been used to vibrationally heat (390 mV, 300 nA) a single propene molecule adsorbed on Cu(211), inducing dehydrogenation without disturbing neighboring molecules [209]. The capability of IETS to target a single molecule for detection and manipulation opens up many possible uses, particularly in developing molecular-scale nanostructures.

The IETS signal can also be mapped spatially for visualization of orbitals related to a specified vibrational mode [214]. Fig.1.10b shows an experiment in which carbon monoxide (CO) and cobalt phthalocyanine (CoPC) are deposited on an Ag(110) substrate and imaged by STM. An IETS spectrum of CO shows a hindered translation peak at 2.8 mV. Picking up a single CO molecule with the STM tip and subsequently acquiring IETS spectra both over the Ag(110) substrate and over a CoPC molecule shows that the 2.8 mV peak shifts to 1.7 mV when the CO-functionalized tip is positioned over a bond in a CoPC molecule. Performing IETS mapping across the entire surface at 1.7 mV then reveals the location of the bonding network in the CoPC molecule [188].

### ***Microwave-Modulated STM***

In the previous sections, we have discussed voltage modulation techniques that involve linear ramping of the tunneling bias. Another approach (Fig.1.10c) involves mixing the usual DC bias with a small AC bias with a frequency (0.5–20 GHz) much higher than that of the feedback loop controlling position (1 kHz) [186] and measuring a down-converted modulation (fA) in the tunneling current (pA). This modulation, which varies with the polarizability of the molecules in the tunneling junction, can be collected simultaneously with the topographical data, using a lock-in amplifier.



This capability has been used in the area of molecular electronics to image buried interfaces, characterizing the electronic state of an oligo(phenyleneethynylene) (OPE) molecular switch in the moments just prior to switching [186]. Fig.1.10c shows standard STM and microwave polarizability images of the same region, in which OPE molecules in the high-conductance ‘on’ state appear as high-contrast features in the microwave image, but those in the low-conductance ‘off’ state do not. Time series images of a single OPE molecule indicate fluctuations in polarizability occurring just prior to switching, suggesting a change in surface contact leading up to the switching event.

Microwave modulation of the field at the tunneling junction can also be performed using an antenna [216,217]. Similar to the scanning capacitance AFM capability discussed earlier, this configuration has been used for dopant profiling in semiconductors, to measure capacitance in conductive organic films [216,218]; it has also been utilized to detect the spin-flip energy of Cr(001) using an iron-coated tip [217].

### 1.3.2 Tip Height Modulation ( $I$ - $z$ Spectroscopy)

Unlike AFM, in which force vs. tip-height is commonly measured, current vs. tip-height ( $I$ - $z$  spectroscopy) is less routinely utilized in STM, though the modality can be employed to measure the work function of the tip based on the tunneling decay constant, as an indicator of tip quality [190]. More recent work by Manassen and coworkers suggests that it is also possible to characterize the elastic moduli of nanoparticles in this manner, similar to an AFM force curve measurement [219]. In a non-imaging context, observing the current dependence on the tip-sample separation is commonly used for STM-based break junction experiments to analyze conductance through a single atom [220] or molecule [221–223]. Early measurements by Besenbacher and coworkers using this technique characterized the conductance quantum,  $G_0 (= 2e^2/h)$ , for a single gold atom (77.48  $\mu$ S), providing an important correlation between theory and experiment [224]. More recent experiments have analyzed conductance in a wide va-

riety of conjugated molecules of interest for molecular electronic applications, including alkanethiols, small aromatic functional molecules including pyridines, and larger functional molecules including oligo(phenyleneethylene)s [57, 222, 225–227]. Conductance in such molecules can vary significantly based on the molecule-metal binding geometry; the break junction measurement is amenable to automated collection of thousands of conductance measurements to average out such variations [225, 226, 228].

### 1.3.3 Application of External Stimuli (Magnetic Field and Electromagnetic Radiation)

#### *Magnetic Field*

**Spin-Polarized Scanning Tunneling Microscopy (SPSTM).** Magnetic properties of a material can be probed by introducing a magnetic field at the tunneling junction. In spin-polarized STM, a magnetic tip is used to image domain structure in a ferromagnetic or antiferromagnetic material at the sub-nanometer scale. The magnetic field in the tunneling junction causes electron spins in the material to align parallel or antiparallel to the field; the probability of tunneling varies with the spin alignment in the material, reaching a maximum when spins in the sample are parallel with those in the tip, and tunneling current increases or reduces the apparent height of features in the STM image. Spectroscopic data across a range of applied biases can be used to further analyze the dependence of electron energy levels on the magnetic field and to measure the spin-dependent conductance of the material.

SP-STM is commonly used in characterizing nanostructured magnetic materials for memory storage applications and quantum computing [229, 230], including monolayer Co islands [231, 232], Fe-Cu dimers [229], and organic-ferromagnetic hybrid interfaces [231]. Fig.1.11 demonstrates contrast between small islands of Co atoms on Ir(111) due to magnetic-field-induced spin alignment [232, 233]. While both islands appear with similar apparent height in the standard STM image, application of an external 0.6 T magnetic field while  $dI/dV$  imaging with an Fe-coated W tip causes

the two islands to appear different based on the alignment of the spins with (red) or against (purple) those in the STM tip. SP-STM has also been utilized to *write* magnetic bit data five-atom Fe complexes on Cu(111) [230, 234].

**Using a non-magnetic tip.** It is also possible to probe magnetic materials by applying an external magnetic field and imaging with a standard metal tip. A step in the  $dI/dV$  spectrum is observed, corresponding to the Zeeman energy (the energy difference between parallel and antiparallel spin states) which is proportional to the magnetic field strength [235, 236]. For instance, the Strosio group has used IETS to probe the spin-flip excitation of individual manganese atoms or atomic chains decoupled from a substrate, demonstrating the utility of the technique for developing magnetic storage devices. As with NMR spectroscopy, applying strong external fields increases spectroscopic resolution [237]. Imaging with an external field of 15 T at temperatures of 10 mK enabled the group to distinguish four normally degenerate quantum states of Landau levels of graphene ( $\Delta E \sim 10\mu\text{eV}$ ) [238].

In certain cases, unpaired spins in molecules can also be probed in a single-molecule electron spin resonance (ESR) experiment, useful for demonstrating the presence of individual organic radicals at an interface [239–242]. Spin precession of the electron creates radio-frequency modulation (500–600 MHz at 200 G) in the tunneling current, which appears as a noise peak in a spectrum analyzer. For instance, Mugnaini et al. measured the Larmor frequency of individual tris(2,4,6-trichlorophenyl)methyl (TMM) radicals on Au(111) at 254.7 MHz, showing the preservation of its unpaired electron even after adsorption.

### ***Electromagnetic Radiation***

**Tip-Enhanced Raman Spectroscopy (TERS).** TERS-STM combines the fingerprinting ability of Raman spectroscopy with the nanoscale spatial resolution of the STM [243], useful in analyzing interfacial materials such as solar cell membranes [161], biomolecules [243], and carbon nanomaterials [244, 245]. Raman spectroscopy is sensi-

tive to changes in polarizability caused by bond vibration, complementary to infrared (IR) spectroscopy, in which changes in dipole moment are detected due to asymmetric bond vibrations. Because the native Raman scattering probability is quite low (1 in  $10^6$  photons scattered in bulk), Raman spectroscopy is often implemented in a configuration that enhances the local field gradient in the vicinity of the molecules being measured to increase scattering. Surface enhanced Raman spectroscopy (SERS) takes advantage of a rough metal surface to increase signal intensity in this way. Large enhancements can also be achieved in a nanoscale gap (typically  $\sim 1$  nm) between metals due to the extremely large field gradient. Both STM and AFM tips can be used to create such a nanoscale gap when used in conjunction with a metal substrate. In TERS-STM, a chemically etched Au or Ag tip is engaged with the surface and irradiated, creating  $\sim 100$  nm<sup>2</sup> of enhanced local electromagnetic with a Raman scattering enhancement factor of up to  $\sim 10^6$  [246]. While typical resolution for TERS-STM is  $\sim 15$  nm [244, 247], the resolution can be improved to 1–2 nm if the local plasmon resonance matches the wavelength corresponding to the electronic transition energy [245, 248]. TERS-STM has also achieved single molecular sensitivity [238, 249–251], although the intensity of the Raman signals depends on the relative orientation of the dipole and the electromagnetic field, potentially producing large signal fluctuations [249, 252].

While many researchers have taken advantage of low temperature UHV environments for improved resolution and reduced photobleaching [247, 250], less restrictive ambient conditions are preferred for analyzing certain types of samples [244]. Zenobi and coworkers simultaneously obtained STM and TERS images of nanotapes formed from  $\beta$ -amyloid(1-40) peptides under ambient conditions (Fig.1.12a) [252, 253]. While the amide I band was missing from the Raman spectrum due to misalignment between the polarization of the external field and that of the peptide amide bond, the aromatic ring breathing mode ( $1004\text{ cm}^{-1}$ ) was evident. Thin nanoribbons appearing with low contrast in STM images were recognized by TERS images based on this form of chemical contrast.

**X-ray Coupled STM.** Synchrotron X-ray scanning tunneling microscopy (SXSTM) correlates surface structure with chemistry [254,255] by probing core electrons whose energy levels depend on elemental identity. Absorption of X-ray photons ( $\sim 10$  keV) results in emission of photoelectrons and enhanced tunneling current due to the excitation of secondary electrons to the electronic states near the Fermi level [216]. The X-ray beam illuminates both a relatively large area of the sample (on the order of  $100\text{ nm} \times 100\text{ nm}$ ) as well as the STM tip. Therefore, localizing detection of photoelectrons (with resolution as good as  $2\text{ nm}$ ) and maintaining a stable tunneling junction requires a specialized tip design that shields the tip, either with an insulating  $\text{SiO}_2$  layer, or with both an insulating layer and a metallic layer [256,257], effectively creating a coaxial shield up to the few nm closest to the tunneling junction. The sum of X-ray induced photocurrent and conventional tunneling current is recorded, and later filtered for deconvolution. Using this experimental design, nm-scale nickel clusters on a Cu(111) surface could be chemically distinguished based on the spatial map of X-ray induced tunneling current, though the number of Ni layers could not be determined based on the X-ray map (Fig.1.12b).

## 1.4 Conclusions and Prospects

Over the past 30 years, a profusion of new instrumental methods incorporating scanning probes have opened unexpected new possibilities for imaging structures of molecules and materials directly in real space. The ability to observe skeletal bond structure within an individual molecule [69,188], track the motion of a molecular machine [66], or to irradiate a solar cell and observe local photoconductivity [20] have been transformative across fields from biology to materials science. Many multimodal scanning probe capabilities, including conductive AFM and force curve imaging, have already been incorporated into commercial instruments, making them widely available to analytical researchers.

In the coming decade, we expect an increased focus on resolving complex chemical structural elements in the 5–10 nm regime, a size scale relevant to both biology and materials science, to meet developing needs in protein structure elucidation, electronics, and renewable energy. While both STM and AFM can provide high-resolution images of relatively simple molecules, and AFM can routinely provide chemical contrast at larger length scales, there are still substantial opportunities for progress in developing broadly applicable methods for resolving nanometer chemical features within larger 5–10 nm structures.

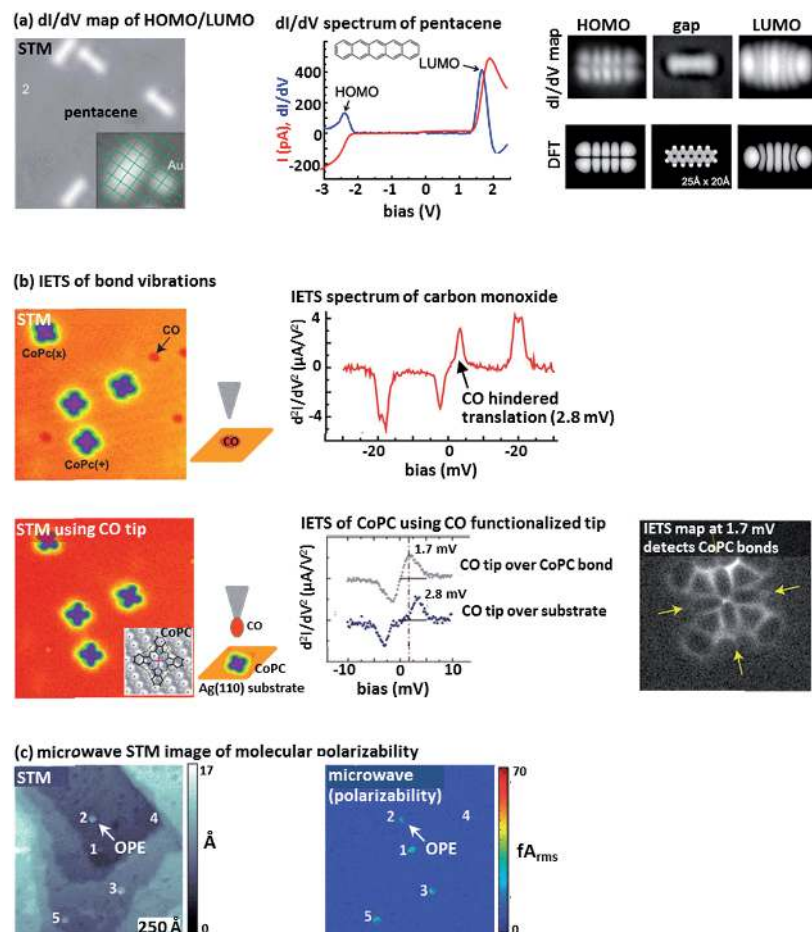


Figure 1.10. Multimodal STM employing bias modulation. (a)  $dI/dV$  spectroscopy identifies the HOMO and LUMO energy levels of a pentacene molecule adsorbed to an insulating bilayer of NaCl on conductive Cu(111). Subsequent STM imaging of a pentacene molecule at a bias corresponding to the energy level of the HOMO, the LUMO, and an intermediate bias in the gap produce images correlated with HOMO and LUMO orbital shapes as calculated using DFT. (b) IETS and IETS mapping. Using an STM tip modified with a single CO molecule allows the surface to be imaged with chemical contrast using a bias corresponding to a vibrational excitation of the CO molecule. IETS spectra acquired at several points over the molecule reveal that the CO hindered translational mode at 2.8 mV shifts to 1.7 mV when the tip sits over a bond in a cobalt phthalocyanine molecule on the Ag(110) surface. Imaging an individual CoPC molecule at 1.7 mV produces a skeletal image of the CoPC bond structure. (d) Microwave frequency bias modulation provides a simultaneously acquired second data channel showing polarizability of the molecule in the junction. Highly polarizable OPE molecules appear in high contrast against a background of less polarizable alkanethiols. Adapted with permission from ref. [186], [187], and [188]. Copyright 2010 American Chemical society, 2005 American Physical Society, and 2014 AAAS.

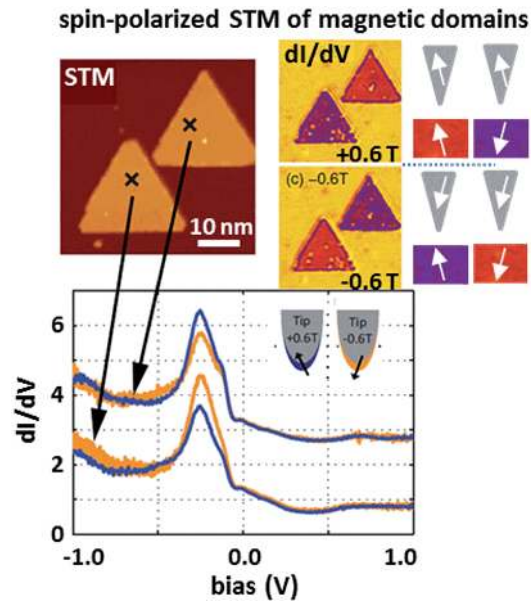


Figure 1.11. Multimodal AFM employing magnetic field. STM image showing two islands of Co atoms on Ir(111). Application of a 0.6 T magnetic field and  $dI/dV$  imaging at 250 mV reveals differences in conductances of the two islands based on spin alignment with (red) or against (purple) the orientations of spins in the magnetic Fe-coated-W STM tip. Adapted with permission from ref. [232]. Copyright 2011 American Physical Society.



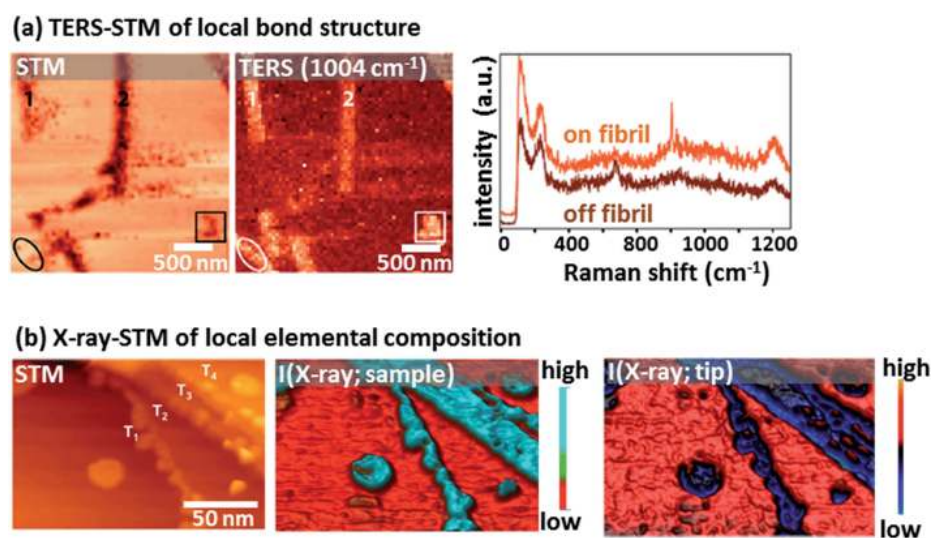


Figure 1.12. Examples of multimodal AFM employing external stimuli. (a) Standard STM and STM-TERS images of amyloid peptide fibrils, which exhibit chemical contrast in the TERS image based on the aromatic ring breathing mode at  $1004\text{ cm}^{-1}$ . (b) Standard and X-ray STM showing chemical contrast from few-nm Ni clusters on Cu(111). Adapted with permission from ref. [252] and [256]. Copyright 2013 and 2014 American Chemical Society.

## 2. SITTING PHASES OF POLYMERIZABLE AMPHIPHILES FOR CONTROLLED FUNCTIONALIZATION OF LAYERED MATERIALS

A version of this chapter has been published in *J. Am. Chem. Soc.*

DOI: 10.1021/jacs.5b13179

### 2.1 Introduction

Precisely controlling surface chemistry using self-assembled monolayers (SAMs) and bilayers has been a central focus of research in both synthetic and biological interfaces [58, 258–260]. Much synthetic monolayer chemistry has its basis in the formation of SAMs of alkanethiols on gold and the coinage metals, pioneered by groups including those of Whitesides, Nuzzo, and Allara in the 1980s [261–264]. Standing-up phases of alkanethiol monolayers form based on a combination of covalent or ionic molecule–substrate interactions (e.g., AuS), strong molecule–molecule van der Waals interactions (e.g., between long alkyl chains) that improve ordering, and a terminal functionality (e.g., CH<sub>3</sub>, COOH, NH<sub>2</sub>, biotin, DNA) that confers solvent wetting properties and/or selectivity for analytes [264, 265]. The surge of interest in colloidal nanocrystals [266–271] has further increased the importance of monolayer chemistry as well as opened entirely new avenues for control of morphology, electronic properties, solubility, and analyte binding [272–276].

Layered materials (e.g., HOPG, graphene, MoS<sub>2</sub>) [1, 277] represent a new frontier in utilizing monolayer chemistry to control physical properties and solubility [10, 11] but also introduce substantial challenges [10, 278]. In single-layer graphene, for instance, all atoms are surface atoms and in solution can actually be coordinated

through two faces, promising unusually high levels of electronic control through the design and spatial organization of appropriate ligands [10, 11]. In contrast with colloidal nanoscopic materials, in which surface curvature typically decreases ligand ordering, the relative flatness of a layered material surface enables ligand ordering that can more strongly resemble SAMs on extended solids [10, 279]. However, maintenance of extended  $\pi$ -conjugation in the layer requires noncovalent functionalization, restricting the choice of ligands [279]. These challenges have impacted the utility of graphene and other layered materials in many applications.

Monolayers on highly oriented pyrolytic graphite (HOPG) and graphene are frequently formed on the basis of lying-down phases of molecules [10, 11, 279, 280]; the increased surface area of the molecule-substrate interaction partially offsets the decreased per-atom interaction strength of noncovalent (vs covalent) interactions [10]. Two common classes of adsorption motifs utilized are long alkanes (e.g., 23-carbon tricosane) [12, 281] and planar aromatic hydrocarbons (e.g., pyrene, anthracene) [11, 13]. In noncovalent monolayers, molecule-molecule interactions also play a more prominent role in monolayer stability. These may be based on van der Waals interactions between long alkanes such as tricosane, one or more hydrogen-bonding interactions (e.g., between planar aromatic molecules that display carboxylic acids on their peripheries [282] or  $\beta$ -strand peptides that hydrogen bond to form  $\beta$ -sheets [61, 283]), or ionic interactions (e.g., in MOFs [284]).

However, even between very long alkanes, intermolecular forces are relatively weak ( $\sim 5$  kJ/mol of  $\text{CH}_2$  between alkane chains [285] and 5–10 kJ/mol of  $\text{CH}_2$  for alkane-HOPG interactions [286]). Thus, an extension of this strategy involves noncovalent functionalization using lying-down phases of reactive molecules, followed by polymerization within the layer [15, 287, 288]. One such route is based on self-assembly of long-chain carboxylic acids derivatized with an internal diyne that can be photopolymerized to yield a conjugated ene-yne polymer [14–17]. A number of studies have examined this reaction on HOPG [15, 289, 290], graphene [291], and  $\text{MoS}_2$  [17, 26], due to interest in the conductive ene-yne as a molecular wire. Such a strategy can

produce monolayers that exhibit some solvent stability [288,292], but a new challenge arises. Early work on monolayers on bulk metals has demonstrated that functional groups positioned adjacent to a hydrophobic monolayer interface undergo large  $pK_a$  shifts (frequently 4 units or more) due to the inability of the interface to stabilize the charged form of the molecule [293,294]. These shifts mean that groups such as carboxylic acids and amines may be predominantly neutral near pH 7 (for instance, in biological buffers), substantially altering their chemical behavior.

Interestingly, a vast amount of biology involving weak acids and bases occurs in a very similar chemical environment: at the periphery of the cellular membrane. Cellular membranes are largely composed of phosphoglycerolipids (typically 60–80 %) [295], in which two long hydrophobic acyl chains connect through a three-carbon glycerol backbone to a hydrophilic head. The head is comprised of a phosphate group connected through a short linker to a terminal functional group that is exposed at the solvent interface. The nominal phosphate  $pK_a$  values of 1.0 for phosphocholine and 1.7 for phosphoethanolamine [296] mean that the group will remain charged at physiological pH (7.4), even if it undergoes an interfacial  $pK_a$  shift. Additionally, the structure of the glycerol backbone facilitates control over headgroup orientation relative to the hydrophobic chains that root it in the bilayer.

Here, we take advantage of the phospholipid architecture to develop an atom-efficient interfacial functionalization strategy that confers the benefits of both standing-up and lying-down monolayers. Lipids in this “sitting-phase” geometry coordinate the surface through two nonpolar alkyl legs, allowing the terminal functional group in the head to project from the interface (Fig.2.1). Leveraging noncovalent assembly and subsequent polymerization utilizing polymerizable phospholipids makes fundamental and important differences in the surface chemistry that enable a new level of control over the ligand’s substrate and solvent interactions. A critical element of this strategy is the elevation of the terminal functional groups above the substrate and the monolayer to reduce interfacial  $pK_a$  shifts. Even modest separation also increases

steric accessibility, which has previously been found to facilitate binding of analytes from solution [297, 298].

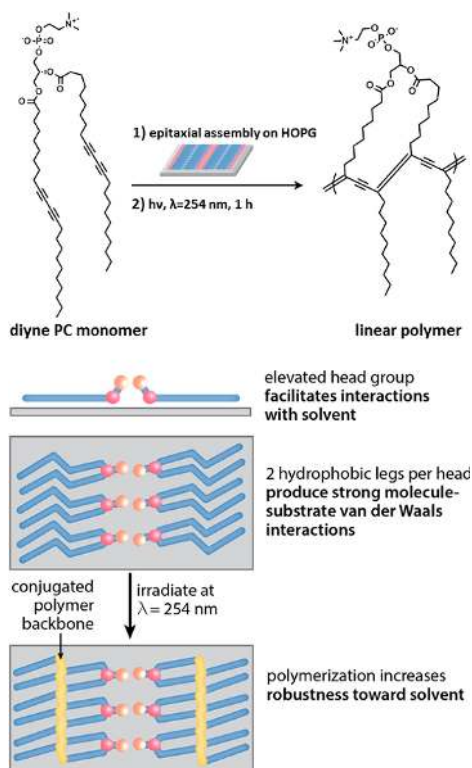


Figure 2.1. Topochemical polymerization of diene lipids.

## 2.2 Results and Discussions

### 2.2.1 Self-Assembled Sitting Phases of Diene Phospholipids.

As a starting point for developing a sitting-phase ligand chemistry for layered materials, we first test the ability of polymerizable diene phospholipids [299, 300] to self-assemble into appropriate structural elements. Previous studies of diene phospholipids in standing-phase monolayers and bilayers indicate that the headgroup tilts; as a result, the two functional alkyl chains penetrate different distances into the bilayer [301]. Thus, when the monolayer is polymerized, the two functional groups join two different polymer chains in the membrane, resulting in low molecular weight

cross-linked polymers very different from the high molecular weight linear polymers that would be necessary to stabilize the sitting-phase monolayers targeted here.

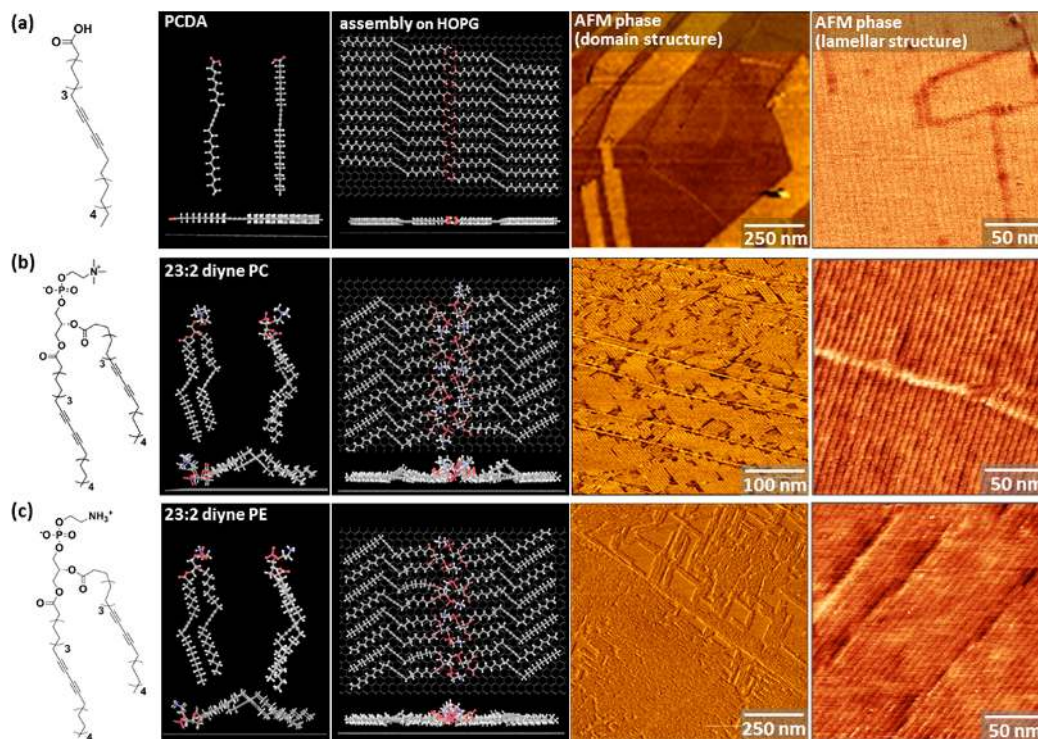


Figure 2.2. Modeled structures and AFM images of self-assembled polymerizable amphiphiles on HOPG. The first column shows (a) PCDA, (b) diyne PC, and (c) diyne PE. For each molecule, the second column shows two views of the solvent-minimized molecular structure (top) and a view of the solvent structure adsorbed to HOPG (bottom). The adsorbed structures were minimized to create the models in the third column, showing top and side views of each monolayer. In the fourth column, AFM phase images show large domains of molecules oriented epitaxially on HOPG; high-resolution images in the fifth column reveal lamellar periodicities ( $\sim 6$  nm) commensurate with the head-to-head models shown in the second column.

Monolayers of diyne amphiphiles were prepared either by drop-casting a small amount of dilute amphiphile in organic solvent or through Langmuir-Schaefer deposition (see the Experimental Methods for details). Because monolayers of fatty acids such as pentacosadiynoic acid (PCDA) have been prepared previously, we compared self-assembled structures of PCDA (Figure 2.2a) and two polymerizable phospho-

lipids: 1,2-bis(10,12-tricosadiynoyl)-sn-glycero-3-phosphocholine (diyne PC, Figure 2.2b) and 1,2-bis(10,12-tricosadiynoyl)-sn-glycero-3-phosphoethanolamine (diyne PE, Figure 2.2c). The two phospholipids differ only in the structure of the terminal head-group functionality; diyne PE terminates in a primary amine, which may be charged or neutral depending on pH and solvent, while the diyne PC terminates in a quaternary ammonium group, which remains charged under all pH and solvent conditions.

A combination of atomic force microscopy (AFM), semi-empirical molecular modeling, and molecular dynamics simulation was used to examine molecular adsorption geometry. First, we assessed structural features in AFM images to address the question of whether molecules assemble head-to-head, creating double rows of headgroups with a  $\sim 6$  nm periodicity (Fig.2.1), or head-to-tail, resulting in single rows of headgroups with  $\sim 3$  nm periodicity. Second, because the molecules can adsorb through two chemically different faces, we performed energy minimizations to examine which adsorption geometry is preferred, an issue that would impact which functional groups in the head are most solvent-accessible.

AFM images of all three molecules deposited on HOPG reveal similar striped patterns with domains arranged at  $\sim 120^\circ$  angles, characteristic of epitaxy with the hexagonal HOPG lattice, as expected from previous experiments with diyneic acids [290]. Line scans extracted from high-resolution AFM images exhibit lamellar periodicities of  $6.3 \pm 0.1$  nm for diyne PE and  $6.6 \pm 0.1$  nm for diyne PC. This is in good agreement with the modeled widths of double lamellae (6.0 nm for diyne PE and 6.4 nm for diyne PC) plus a van der Waals contact distance. Importantly, this suggests that the head-to-head structure is energetically preferred for both phospholipids, since a head-to-tail arrangement would likely produce features with  $\sim 3$  nm periodicity.

Unlike the diyneic acids, both diyne phospholipids contain a chiral center in the headgroup, creating multiple possible adsorption geometries. Phospholipids may adsorb with the phosphate ( $-\text{PO}_2^-$ ) facing the substrate, increasing the solvent accessibility of the amine (and presumably partly screening the phosphate charge), or

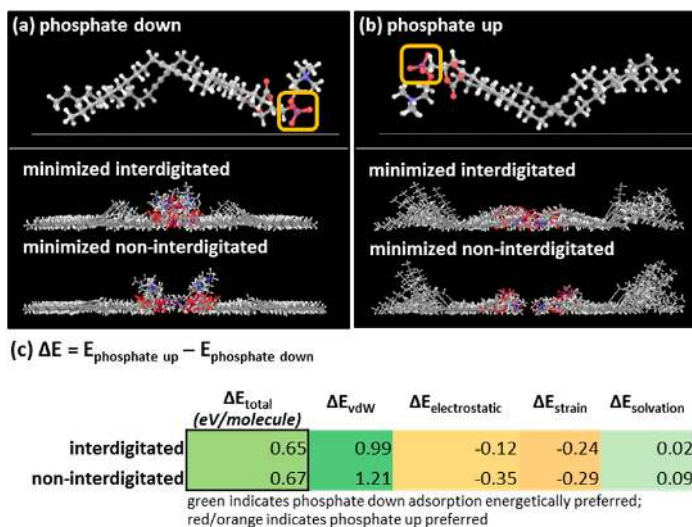


Figure 2.3. Minimizations of amphiphiles in phosphate-down and phosphate-up adsorption geometries. Minimized models of rows of molecules adsorbed in (a) phosphate-down and (b) phosphate-up configurations reveal greater tail group ordering for the phosphate-down configuration in both interdigitated and noninterdigitated headgroup configurations. (c) Energy differences between the two adsorption configurations indicate that the phosphate-down conformation is preferred due to increased van der Waals interactions.

they may adsorb with the phosphate proximal to the solvent and the amine adjacent to the surface. To test which configuration is more energetically favorable, we created models consisting of two adjacent rows of eight diyne lipids each adsorbed to a stack of two graphene sheets, with all molecules adsorbed in either a phosphate-down configuration (Figure 2.3a) or a phosphate-up configuration (Figure 2.3b). Additionally, because the phosphocholine and phosphoethanolamine headgroups are narrower than the combined width of the two alkyl tails, it is possible to envision that headgroups from adjacent rows might interdigitate, leading to a configuration in which phosphates from one row lie next to the terminal amine or ammonium groups of molecules in the adjacent row. Such an interdigitated structure would be expected to increase the robustness of the monolayer, while likely decreasing the solvent accessibility of the headgroups. Therefore, we created sets of models in which molecules



are initially positioned with interdigitated headgroups and models in which the rows are positioned 4 Å further apart, producing a noninterdigitated initial headgroup configuration. Minimization results in chloroform are presented in Figure 2.3c, as an energy difference between phosphate-down and phosphate-up adsorption geometries, expressed in units of eV/molecule (1 eV/molecule  $\approx$  96 kJ/mol). Both interdigitated and noninterdigitated initial headgroup configurations lead to an energetic preference of 0.6–0.7 eV/molecule for the phosphate-down configuration. Analyzing contributions from van der Waals and electrostatic interactions, strain, and solvation reveals that the preference arises from increased van der Waals interactions in the phosphate-down configuration. This is qualitatively visible in side views of the minimized models (Figure 2.3a,b) as increased ordering of the tail groups for phosphate-down structures in comparison with those of phosphate-up structures.

On the basis of modeling, it is not evident whether interdigitated headgroups would be preferred; however, a comparison of calculated and experimental lamellar widths suggests that the peripheries of the lamellar structures are not interdigitated. Minimizations of interdigitated structures lead to slightly smaller calculated average lamellar widths (5.8 nm for diyne PE and 5.7 nm for diyne PC) than those calculated for noninterdigitated structures (6.0 and 6.4 nm, *vide supra*). For diyne PC in particular (presumably due to the larger steric bulk of the terminal quaternary ammonium group), this leads to a relatively large difference between the modeled structure width and the structural periodicity observed experimentally in AFM images. Therefore, we postulate that the surface-adsorbed lipids adopt a noninterdigitated headgroup organization, which would increase the steric freedom of the terminal functional groups in comparison with an interdigitated structure.

### 2.2.2 Polymerization of Diyne Phospholipids

While individual molecules are relatively weakly adsorbed at the interface, surface-templated polymerization provides a route for increasing monolayer stability. Because

diynoic acid monolayers on HOPG are known to undergo surface-templated photopolymerization [14, 290], it is reasonable to expect the same reactivity from the diynoic lipids we use here. However, a key structural consideration prompted us to examine molecular models to further explore the likelihood of polymerization: adjacent chains in lipid lamellae are bound together through the phospholipid headgroup, while the chains in diynoic acid lamellae are not.

Such a consideration is important in the context of this surface-templated reaction for two reasons. First, photopolymerization rates for diynes are known to depend strongly on the distance between the two bond-forming carbons in the crystal. In 3D crystals of smaller diynes (particularly ptoluenesulfonate hexadiyne) [302, 303], increases of 1.0 Å between the bond-forming carbons correspond to a 2-fold decrease in polymerization rate. Similar constraints hold in 2D domains of diacetylene; in addition to decreasing polymerization efficiency with increasing separation between bond-forming carbons, studies of diynoic acids on HOPG and MoS<sub>2</sub> suggest differences in organization and polymerization behavior based on differences in lattice constants and work functions of the substrates [17, 26]. For instance, on MoS<sub>2</sub>, polymerization efficiency is  $\sim 4$  times higher than on HOPG, due to the increased conformational freedom afforded to alkyl chains in weaker epitaxy with the MoS<sub>2</sub> lattice [26]. A second structural consideration for polymerization is that the diyne functional group undergoes a rotation of  $\sim 45^\circ$  in the plane of the substrate in order to join the growing ene-yne polymer chain [302]. Therefore, it is possible that the additional constraints placed on chains joined through a headgroup would prevent them from undergoing polymerization.

With these considerations in mind, we compare the average distance ( $D_{10-13}$ ) between bond-forming carbons (C10 of one chain and C13 of the adjacent chain) in monolayers of PCDA with those for the diyne phospholipid monolayers we form here. In calculating the C10–C13 distances for lipids, we examine pairs of chains both within a single molecule and between adjacent molecules. Minimized models of the diyne lipids show  $D_{10-13}(\text{diyne PC}) = 4.1 \text{ Å}$ , comparable to  $D_{10-13}(\text{PCDA}) = 4.0$

Å. In addition, the initial angle  $\theta$  between the diyne and the lamellar axis is slightly smaller for the phospholipids ( $\theta_{PCDA} = 59^\circ$ ,  $\theta_{diynePC} = 51^\circ$ ), leading to favorable reduced rotational angles relative to PCDA ( $\Delta\theta_{PCDA} = 45^\circ$ ,  $\Delta\theta_{diynePC} = 34^\circ$ ).

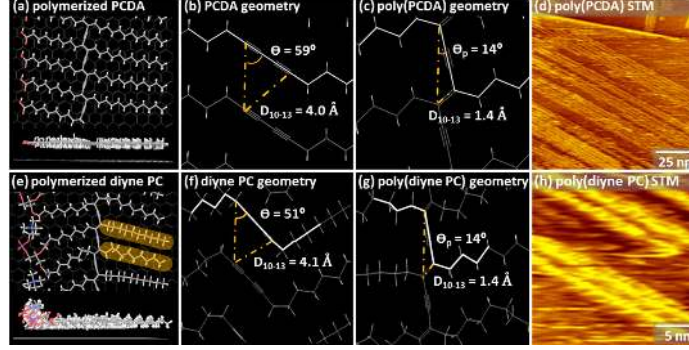


Figure 2.4. Energy-minimized molecular models and STM images showing polymerized (a–d) PCDA and (e–h) diyne PC. Minimized models of (b) unpolymerized PCDA and (f) diyne PC show that the distance between bond-forming carbons ( $D_{10-13}$ ) and the angle between diyne and lamellar axis ( $\theta$ ) are similar for the two molecules. STM images of polymerized (d) PCDA and (h) diyne PC show apparent protrusions corresponding to the conjugated ene-yne polymer. Highlighting in panel (e) indicates the alternating alkyl chain orientation probed in Figure 2.6.

STM images of polymerized diynes are known to exhibit features with increased apparent height due to formation of the conjugated ene-yne polymer backbone [14,58]. Figure 2.4 shows STM images of polymerized diynoic acids (Figure 2.4d) and polymerized diyne PC (Figure 2.4h). Apparent protrusions in the image appear corresponding to modulations in both the topography and the local density of electronic states (LDOS). The relatively small HOMO-LUMO gap in polymerized diacetylenes vs diacetylene monomers increases the LDOS near the Fermi level, increasing the probability of electron tunneling [16]; although the native band gap of bulk polydiacetylenes is 2.3–2.5 eV, p-doping from HOPG substrates can reduce the band gap to as little as 0.5 eV [17]. Imaging at sufficiently large negative sample biases (here,  $V_s = 1.5$  V) facilitates a two-step tunneling process that proceeds through the polydiacetylene wire [16,33]. While a number of studies provide experimental evidence suggesting

that PCDA and other diynoic acids form a polymerized structure in which the ene-yne polymer is elevated  $\sim 1.4$  Å in relation to the surrounding alkyl chains [14, 290], DFT studies suggest that the lifted and in-plane polymer structures are similar in energy [304], and in our simulations, models of both polymerized PCDA and diyne PC minimize to in-plane structures, though experimentally we find the standard linear features (Figure 2.4d) observed previously in STM images of polymerized PCDA. Previous studies imaging monolayers of long-chain diynes that do not form hydrogen-bonded dimers between headgroups (e.g. 17,19- hexatriacontadiyne) find a transition from a lifted phase at 220 K to the in-plane conformation at room temperature [305], which lacks the protruding linear features visible in STM images of PCDA. Here, while we observe the appearance of some linear features in STM images of polymerized diyne phospholipids (Figure 2.4h), the surface density of such features is lower than for PCDA, which could indicate either lower polymerization efficiency or the formation of an in-plane polymerized phase, as indicated in the minimized model (Figure 2.4e).

Because our primary interest is in the wetting properties of the interface, we use a washing assay to assess the impact of the polymerization on improving film robustness toward solvent. Samples of unpolymerized and polymerized amphiphiles were imaged and then subjected to sequential washing and imaging cycles to understand the extent to which washing removed molecules from the monolayer. Ethanol was used as a low surface tension washing solvent. Samples were washed vigorously with a stream of solvent from a squeeze bottle for 5-s intervals and then blown dry using compressed nitrogen gas. Figure 2.5 shows prewash and postwash images for unpolymerized and polymerized PCDA and diyne PE. Polymerized PCDA (Figure 2.5b) exhibits enhanced stability relative to unpolymerized PCDA (Figure 2.5a), demonstrating well-resolved lamellar structures within the domains throughout the washing procedure, although molecules at domain edges were eroded. The destabilizing effect of washing is also reflected in the increasing streakiness of the domain images, typically indicative of the presence of loose molecules. Conversely, a substantial frac-

tion of the surface of the unpolymerized PCDA sample appeared bare after 5 s of washing, with only sparsely distributed aggregates of PCDA still visible, appearing as dark islands in the phase insets. In contrast, washing unpolymerized diyne PE (Figure 2.5c) resulted in slow etching of domain edges, with  $\sim 40\%$  of the surface containing ordered domains even after 30 s of washing. For polymerized diyne PE (Figure 2.5d), etching around domain edges was much slower, and  $\sim 80\%$  of the surface remained covered after 30 s of washing. We postulate that the enhanced stability of both polymerized and unpolymerized phospholipids relative to the diynoic acids may result from the increased number of alkyl carbons per molecule.

Molecular models suggest substantial differences in alkyl chain orientation between PCDA and the diyne phospholipids (Figure 2.4a,e). In PCDA, strong hydrogen-bonding interactions in carboxylic acid dimers order the headgroups, and tails form a tightly packed lattice with the zigzag backbone of the alkyl chains parallel to the HOPG surface [14]. In contrast, our models suggest that the lipid headgroups are somewhat disordered due to the three-dimensional geometry around the glycerol backbone. Our models also suggest that the lipid tail groups form an unusual structure in which the alkyl chains alternately zigzag parallel and perpendicular to the HOPG surface (highlighted in Figure 2.4e). Polarization modulated IR reflection absorption spectroscopy (PM-IRRAS) [306] measurements of films of PCDA and diyne lipids on HOPG exhibit substantial differences in C–H stretch intensity (Figure 2.6a) consistent with this difference in ordering. Ester C=O stretch peak intensities for diyne PC are also reduced relative to PCDA C=O stretch intensities (Figure 2.6b), consistent with energy-minimized models, suggesting that the ester linkage adopts a variety of configurations relative to the surface normal, in order to bring the two diynes into alignment as the lipid conforms to the graphite surface.

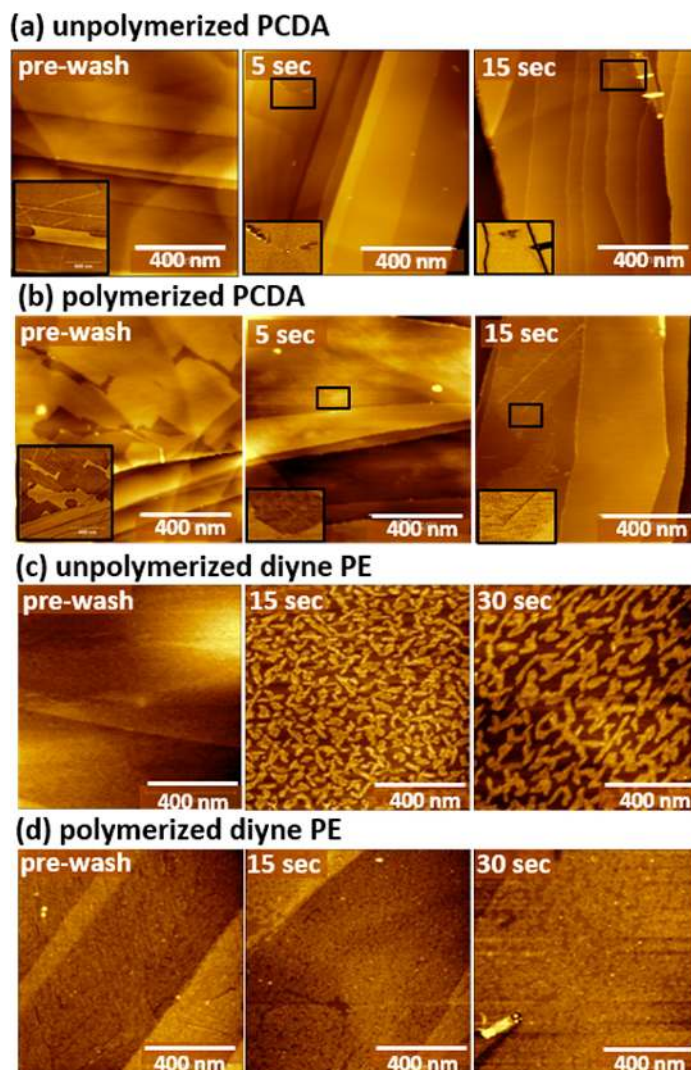


Figure 2.5. Solvent washing assay for unpolymers and polymers PCDA (a and b) and diyne PE (c and d) shows the enhanced stability of polymers monolayers in comparison with unpolymers monolayers and increased stability of diyne PE vs PCDA. Insets of panels a and b show phase images of the entire images or the corresponding scanned areas marked by the black square.

### 2.2.3 Controlling the Charge State of Surface Functional Group Patterns.

The difference in placement of the phosphate and amine functional groups relative to the interface is expected to impact their ionization and, thus, interactions with solvents and analytes.

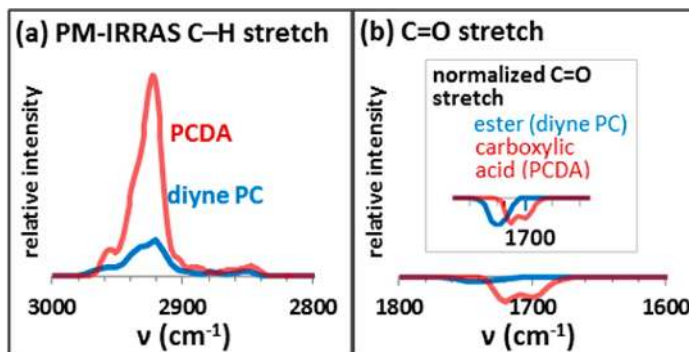


Figure 2.6. PM-IRRAS spectra of films of PCDA and diyne PC exhibit differences in (a) C–H and (b) C=O stretch intensities consistent with alkyl chain orientation differences observed in energy-minimized molecular models.

A number of techniques, including differential capacitance measurements [307], nonlinear optical spectroscopy [308], and contact angle goniometry [293], can be used to assess ionization behavior at interfaces. Here, we use contact angle titration, in which a series of small droplets of buffers with controlled pH are applied to the interface; the contact angles of the buffer droplets change in pH ranges corresponding to the ionization of functional groups at the interface [293]. Interfacial  $pK_{1/2}$  values are known to differ substantially from  $pK_a$ s of the same functionalities in solution. For instance, the  $pK_a$  of acetic acid in dilute aqueous solution is  $\sim 4.7$  [309]. However, previously it has been shown that both carboxylic acid-terminated SAMs and oxidized polymer films displaying carboxylic acids typically exhibit  $pK_{1/2}$  values of 7–8 [293]. Similarly,  $pK_{1/2}$  values of amines in alkanethiol SAMs typically decrease relative to  $pK_a$  values in aqueous solutions. While the  $pK_a$  of dilute methylamine in aqueous solution is 10.5 [294], one study measured a  $pK_{1/2}$  of 6.5 for an  $\text{NH}_2$ -terminated undecanethiol SAM, lower than the measured  $pK_{1/2}$  of 7.4 for a  $\text{COOH}$ -terminated undecanethiol SAM measured in the same work [294]. Both shifts can be understood by considering the equilibrium between charged and neutral forms of the molecules; in both amines and carboxylic acids, proximity to the nonpolar interface decreases stabilization of the charged form of the functional group, shifting the equilibrium

toward the neutral form. Similarly,  $pK_{1/2}$  has been shown to vary with the surface density of functional groups in a SAM [293]. For a 75 % COOH-terminated alkyl SAM, the measured  $pK_{1/2}$  was 8.5, while for a lower-coverage 15COOH-terminated alkyl SAM, the  $pK_{1/2}$  shifted as high as 11.

Both surface shifts and those due to fractional coverage are important in predicting the ionization behavior of functional groups in the monolayers prepared here. Figure 1a shows that for PCDA monolayers, approximately 10 % of the surface consists of ionizable functional groups. However, the chemical environment of the carboxylic acid groups is more similar to that which would be found in a high-percentage COOH-terminated alkyl thiol SAM, since the functionalities are clustered at the lamellar edges.

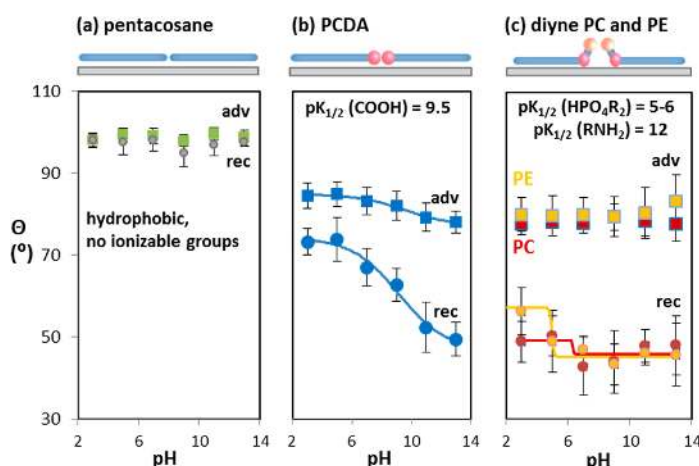


Figure 2.7. Contact angle titrations showing changes in contact angle with buffer pH for HOPG with adsorbed (a) pentacosane, (b) polymerized PCDA, and (c) polymerized diene lipids PC and PE. Square markers indicate advancing contact angles; circles indicate receding contact angles. Error bars indicate the standard deviation in angle over a series of nine measurements acquired from three different samples.

Figure 2.7 shows the results of contact angle titrations for pentacosane, PCDA, diene PC, and diene PE. For films of pentacosane (Figure 2.7a), a 25-carbon alkane, on HOPG, contact angles are  $\sim 98^\circ$  across the tested pH range (113). For PCDA



(Figure 2.7b, squares = advancing, circles = receding), contact angles are lower than for pentacosane due to the introduction of the polar carboxylic acid functional group. Below pH 5, the carboxylic acids are neutral, leading to advancing contact angles of  $\sim 84^\circ$ . We correlate this decrease with the fractional surface coverage of carboxylic acids using a modified form of the Young–Dupré equation for interfaces with nanoscale chemical heterogeneity [310]:

$$(1 + \cos \theta_{PCDA})^2 = f_{alkyl}(1 + \cos \theta_{alkyl})^2 + f_{COOH}(1 + \cos \theta_{COOH})^2$$

Using the measured contact angle of  $98^\circ$  for alkyl chains aligned epitaxially on HOPG,  $84^\circ$  for neutral PCDA, and  $30^\circ$  for neutral COOH groups (value observed in previous contact angle measurements on 100 % COOH-terminated alkyl thiol SAMs [293]), the observed decrease in contact angle relative to pentacosane would be expected for an 18 % surface coverage of neutral carboxylic acid groups, consistent with moderate disordering of the COOH groups during wetting. We note that it is not entirely clear that the contact angle for a lying-down phase of COOH dimers would be exactly the same as that ( $30^\circ$ ) for a standing phase of alkanethiol-terminated COOH groups and that, if the bond dipoles in the carboxylic acid are oriented in the plane of the monolayer, this would lead to a somewhat higher water contact angle. Using a larger contact angle in the above equation results in a higher calculated  $f_{COOH}$ , implying more disordering at the interface and a disruption of the COOH dimers along the periphery of the lamellar structure. This reorientation would produce hydrophilic areas with unpaired -COOH groups more closely resembling standing-phase COOH-terminated alkanethiols. Thus, the calculated hydrophilic surface coverage of 18% should be considered an approximate but reasonable minimum. With increasing pH, the carboxylic acids begin to ionize, further decreasing both advancing and receding angles. On the basis of the receding angles (blue circles), in which the larger change in contact angle makes the transition more evident, we estimate an onset of ionization at pH 5 and a  $pK_{1/2}$  of 9.5, using a sigmoidal fit (blue line). Therefore, while the  $pK_{1/2}$  is shifted due to the nonpolar environment at the interface, clustering

the carboxylic acid groups at lamellar edges decreases the  $pK_{1/2}$  relative to the value of 11 measured previously for 15 % COOH-terminated standing phases of alkanethiol SAMs on Au(111) [293].

In contrast with PCDA, diyne PC (Figure 2.7c, red squares = advancing; red circles = receding) has a terminal quaternary ammonium group that remains charged across the pH range, leading to advancing contact angles  $\sim 74^\circ$ , similar to those for the ionized form of PCDA. Although the ammonium group remains charged, at low pH, the phosphate group can become protonated. While the solution  $pK_a$  for a phosphocholine phosphate is 1, here we observe a  $pK_{1/2}$  of approximately 5.9, consistent with the interfacial  $pK_a$  shift of the carboxylic acid in PCDA. Similarly, for diyne PE, an increase in receding contact angle is observed at low pH (Figure 2.7c, yellow circles), with a calculated  $pK_{1/2} = 4.9$ . This sigmoidal fit was calculated using additional data points below pH 3 to improve accuracy.

The diyne PE primary amine has a solution  $pK_a$  of 11. A small increase in the advancing contact angle is observed near pH 11 (Figure 2.7c, yellow squares), consistent with neutralization of the amine. No corresponding increase in receding angle is observed (Figure 2.7c, yellow circles), presumably because the phosphate group remains charged and can influence the receding angle more strongly than the advancing angle. Importantly, this suggests that the diyne PE amine does not undergo a significant interfacial  $pK_{1/2}$  shift due to its separation from the hydrophobic interface and the proximity of the charged phosphate group.

## 2.3 Conclusion and Prospects

Here, we have demonstrated a route for functionalization of layered materials based on sitting phases of polymerizable lipids. The lipids contain multiple functional groups (phosphate and amine or ammonium) that are precisely positioned relative to the layered material interface. Because the phosphate sits close to the interface, it experiences a  $pK_a$  shift characteristic of functional groups at hydropho-

bic interfaces; conversely, the terminal primary amine in diyne PE, which projects just a few angstroms above the interface, maintains its standard solution ionization behavior. This difference points to the ability to tailor chemical characteristics of the interface by varying the functionalities present in the lipid headgroup and their positions relative to the interface.

On the basis of the diversity of natural lipids (over 100 unique lipids have been identified to date) [295], it is reasonable to suppose that a large amount of structural and chemical diversity can be introduced into monolayers using this strategy. In biology, lipids are known to play roles in stabilizing membrane curvature and junctions, protein interactions, regulating cell growth, and biosynthetic pathways, suggesting the possibility that similarly diverse functions could be stably integrated with layered materials.

## 2.4 Experimental Methods

**Amphiphile Monolayer Preparation** Diacetylene-functionalized phospholipids and fatty acids were purchased from suppliers indicated and used as received: 1,2-bis(10,12-tricosadiynoyl)-sn-glycero-3-phosphocholine (Avanti Lipids, Alabaster, AL, > 99.0 % purity), 1,2-bis(10,12-tricosadiynoyl)-sn-glycero-3-phosphoethanolamine (Avanti, > 99.0 % purity), 10,12-pentacosadiynoic acid (Sigma-Aldrich, St. Louis, MO,  $\geq$  97.0 % purity), and 10,12-nonacosadiynoic acid (Tokyo Chemical International, Tokyo, Japan, > 97.0 % purity). Chloroform, hexane, and isopropyl alcohol (ChromAR grade) were purchased from Macron Fine Chemicals (Center Valley, PA) and used as received. Self-assembled monolayers of diacetylene-functionalized lipids and fatty acids were prepared either by drop-casting or LangmuirSchaefer (LS) deposition as described below. In both techniques, polymerizable amphiphiles were deposited on  $1 \times 1$  cm highly oriented pyrolytic graphite (HOPG, SPI Supplies, West Chester, PA) substrates, which were freshly cleaved immediately prior to sample de-

position. All initial steps in the deposition process were carried out under UV-filtered light to prevent polymerization in solution.

For samples prepared by drop-casting, monolayers of lipids and fatty acids were formed by placing 6  $\mu\text{L}$  of a 0.015–0.017 mg/mL solution of the functional molecule in a 3:2 (v/v) mixture of hexane:isopropyl alcohol on a heated (90–107 °C) HOPG substrate. LS deposition was performed using a KSV-NIMA Langmuir-Blodgett trough (Biolin Scientific, Stockholm, Sweden). For the deposition of fatty acids, 12  $\mu\text{L}$  of a 0.75 mg/mL solution of fatty acid in chloroform was deposited on a subphase of deionized water ( $\sim 18\text{ M}\Omega$ ). For phospholipid monolayers, deposition was performed by spreading 15–20  $\mu\text{L}$  of a 0.5 mg/mL solution of lipid in chloroform onto a subphase of aqueous 5 mM  $\text{MnCl}_2$ . After the small amount of chloroform used for amphiphile transfer was allowed to evaporate, trough barriers were slowly moved inward to adjust the surface pressure. When the surface pressure reached 10 mN/m, the HOPG substrate was slowly lowered onto the subphase with the cleaved surface facing down, parallel to the liquid interface. After 4 min in contact with the liquid interface, the HOPG was gently lifted out of contact with the liquid using the automatic dipper.

Diacetylene-functionalized amphiphile monolayers prepared using the described procedure were photopolymerized by 1 h of irradiation under a 254-nm 8-W UV lamp with approximately 4 cm between the lamp and the sample surface.

**AFM Imaging** All AFM measurements were performed under ambient conditions using a Veeco MultiMode (Bruker Instruments, Billerica, MA) instrument in tapping mode with Nanoprobe (Neuchatel, Switzerland) PPP-FM or RFESP-75 tips (nominal force constant 3 N/m and radius of curvature  $<10\text{ nm}$ ).

**STM Imaging** STM images were acquired using a custom-built ambient STM [186,311,312] with a Besocke-type head design and RHK-R9 control electronics (RHK Technology, Troy, MI). STM tips were prepared mechanically from Pt/Ir alloy wire (Goodfellow, Pt 90%, Ir 10%). Imaging was performed in constant current mode with a tip bias of 1.5 V and tunneling current set point of 7 pA.

**Energy Minimization** Software packages Maestro46 and Macromodel [292] (Schrödinger, Cambridge, MA) were used, respectively, to visualize the structures of phospholipids and fatty acids on graphene and to perform the force field minimizations and molecular dynamics simulations. All models were minimized using the OPLS\_2005 force field [293], with normal cutoffs for van der Waals, electrostatic, and hydrogen-bonding interactions. Minimizations were performed using the PolakRibiere conjugate gradient (PRCG) algorithm and gradient method with 50 000 runs and a convergence threshold of 0.05. Most minimizations converged in less than 10 000 runs. For all calculations, atoms in the graphene sheets were frozen, to more closely mimic the structure of HOPG. Thus, while they contributed to the forces present in the system, their positions did not change in response to conformational changes of the adsorbed amphiphiles. For simulations using aqueous buffers, molecular dynamics simulations were carried out using explicit water and ions to simulate 5 mM  $\text{MnCl}_2$ . Briefly, 1680 water molecules, 19  $\text{Mn}^{2+}$  ions, and 38  $\text{Cl}^-$  were positioned with appropriate spacings over graphene sheets identical to those used in chloroform and solvent-free minimizations. Molecular dynamics simulations were run for 200 ps; models were subsequently reminimized and energy values tabulated as for other models.

**Contact Angle Titrations** Contact angle titrations were performed using an Attension Theta optical tensiometer (Biolin Scientific, Stockholm, Sweden) in sessile drop mode. Buffers with 20 mM buffering capacity at a range of pH values from 1 to 14 were purchased from Sigma-Aldrich and used as received. The pH of each buffer was measured prior to utilization in contact angle measurements to ensure that the measured pH was within 0.2 units of the stated pH. For each measurement, a 5- $\mu\text{L}$  droplet of buffer solution at the stated pH was deposited on a prepared sample of polymerized amphiphile on HOPG, and the contact angle was measured within 10 s and recorded as the advancing contact angle. Subsequently, solvent was withdrawn from the droplet using a syringe with a 32-gauge needle, until the solvent front on the sample receded. The contact angle was measured at this point and recorded

as the receding contact angle. Each contact angle graphed in the paper represents the average of nine points (three points measured on each of three different samples). Typically, it was possible to acquire a grid of nine measurements per  $1 \times 1$  cm sample.

**PM-IRRAS** Spectra were acquired using a custom-built PM-IRRAS spectrophotometer. The infrared light source, interferometer, and data collection and processing were provided by a Nicolet iS50R spectrometer (Thermo, Waltham, MA). All optical components were purchased from Thorlabs (Newton, NJ) unless otherwise specified. The infrared beam was passed from the spectrometer exit port into a polycarbonate enclosure and directed through a KRS-5 lens at a  $70^\circ$  incidence angle using AR coated gold mirrors. The beam then passed through a holographic  $\text{BaF}_2$  linear polarizer set at an angle of  $45^\circ$  relative to the optical axis of a Hinds Series II ZNS50 photoelastic modulator (Hinds Instruments, Portland, OR), which modulated the beam at a 50 kHz frequency with the half-wave retardation set to  $2100 \text{ cm}^{-1}$ . The beam was then focused onto the sample and reflected through a second  $\text{BaF}_2$  linear polarizer, which was adjusted to minimize the polarization effects of the substrate. Finally, the light was focused through a  $\text{BaF}_2$  lens onto a HgCdTe high  $D^*$  detector (Thermo, Waltham, MA). Spectra were acquired at  $8 \text{ cm}^{-1}$  resolution and normalized by dividing a spectrum of the substrate with a monolayer by a spectrum of a bare substrate.

### 3. HIERARCHICALLY PATTERNED NONCOVALENT FUNCTIONALIZATION OF 2D CONTROLLED LANGMUIR-SCHAEFER CONVERSION

A version of this chapter has been published in *Langmuir*

DOI: 10.1021/acs.langmuir.7b03845

#### 3.1 Introduction

As 2D materials (e.g., graphene, MoS<sub>2</sub>) are integrated more widely into hybrid materials and devices, rigorous control over both global and local surface chemistry becomes increasingly important [10,11]. Microscopic and nanoscopic patterning methods have been developed for monolayer chemistries including alkanethiols on the coinage metals, and have found remarkably broad use [29,58,264,313]. However, patterning monolayers on 2D materials raises additional challenges because such materials are often functionalized noncovalently (e.g., with lying-down phases of functional alkanes or polycyclic aromatic compounds) [11,281,314,315]. While this strategy avoids disrupting extended electronic conjugation within the 2D layer, it also reduces monolayer stability, with potential impacts to both pattern fidelity and characterization [306]. Thus, patterning and characterization strategies that are effective for covalent monolayers are not necessarily equally useful for noncovalently functionalized 2D materials, suggesting utility to the development of methods relevant to such interfaces.

Lying-down phases of diynoic acids such as 10,12- pentacosadiynoic acid (PCDA, Figure 3.1a) have been extensively investigated in the context of noncovalent functionalization of 2D materials [14–16,26,58,290]. When drop-cast from organic solvents

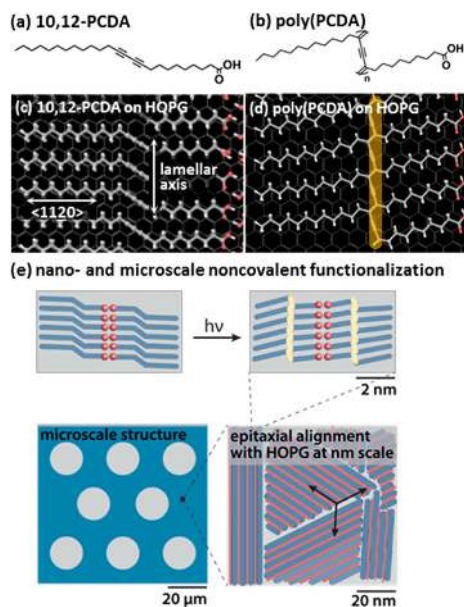


Figure 3.1. Structures of 10,12-PCDA (a) before and (b) after photopolymerization. Molecular models of (c) pre- and (d) postpolymerization lying-down phases epitaxially assembled on HOPG. (e) Schematic of targeted hierarchical nano- and microscale noncovalent functionalization of 2D material.

such as  $\text{CHCl}_3$  or assembled at a liquid-solid interface from low-vapor-pressure solvents such as octadecene, these molecules form lying-down lamellar striped phases (Figure 3.1c–e). In the lamellae, the zigzag carbon skeleton of each alkyl chain aligns along the  $\langle 11\bar{2}0 \rangle$  direction of the hexagonal highly oriented pyrolytic graphite (HOPG) lattice (Figure 3.1c), and pairs of headgroups form hydrogen-bonded carboxylic acid dimers that further stabilize the lamellar structure. The paired headgroup structure results in a lamellar width  $\sim 6$  nm (approximately twice the chain length), comprising predominantly exposed alkyl chains with rows of polar headgroups  $\sim 1$  nm wide.

The lamellar monolayer architecture also aligns the internal diynes for topochemical photopolymerization (Figure 3.1b,d) when the surface is exposed to UV irradiation [290, 316]. The conjugated ene-yne polymer backbone formed by irradiation of nanoscopic circuit design. Polymerization also stabilizes the monolayer toward removal of the deposition solvent and/or addition of other solvents [317, 318]. A



growing literature has begun to elucidate the consequences of the 1 nm wide stripes of functional headgroups and the noncovalently adsorbed ligand architecture (both PCDA and other polymerized diynes) in controlling interfacial wettability and other properties relevant to device design utilizing noncovalently functionalized 2D materials [317–322].

As this type of self-assembly has become more widely utilized to control the surface chemistry of 2D materials, governing not only nanoscopic but also microscopic ordering becomes desirable. Assembly from solution at the solid-liquid interface can create stable nanoscopic domain structures and molecular scale patterns [10,314,319], although microscale patterning is less straightforward.

In contrast, Langmuir-Schaefer (LS) transfer [30] provides significant potential advantages for patterning noncovalent 2D interface chemistry at the microscale by modulating local molecular adsorption across the substrate. A rich literature on molecular assembly, phase transitions, and phase segregation in Langmuir films has shown that it is possible to assemble diverse molecular patterns in monolayers on an aqueous subphase [323–328]. These molecular patterns can be transferred to solid supports through either vertical dipping (Langmuir-Blodgett, LB, transfer) [329,330] or horizontal dipping (LS transfer) [30,331].

Although both methods are classically used to transfer standing phases, a few reports have indicated that the LS approach can be used to create noncovalent lying-down monolayers of molecules such as PCDA on HOPG by deliberately converting the standing phase on the aqueous subphase into a well-ordered lying-down striped phase on the 2D material [14,32,33]. Previous reports of LS conversion of this type have been aimed at understanding molecular scale ordering and the formation of ene-yne molecular wires [15,16,332,333] relevant to nanoscopic circuit design [290,315]. Thus, they have used scanning tunneling microscopy (STM) and atomic force microscopy (AFM) to examine transferred molecular domains on scales typically  $< 1 \mu\text{m}$ . More recently, we have found that it is possible to assemble much larger domains ( $> 10 \mu\text{m}$ ) through LS conversion at elevated temperatures (50–70 °C) and that long-range

order confers additional stability during vigorous solvent washing [322], relevant to solution processing for some device preparation protocols [317, 318, 320–322].

Broadly, we aim to develop a foundation for using LS conversion to create spatially controlled microscopic patterns exhibiting the characteristic nanoscopic ordering (i.e., striped molecular rows) that has led to sustained long-term interest in noncovalent functionalization with diynes. Several questions arise: What structural factors in Langmuir films promote molecular transfer to the 2D material? Can transfer be prevented in specified areas of the film, analogous to resists used in other forms of patterning? What factors increase or decrease local ordering as transferred molecules assemble into domains on the 2D material?

Mechanistically, LS conversion of standing phases to form lying-down phases represents a fundamental departure from classical LS transfer of standing phases. In the classical LS transfer, domains of tightly packed molecules are lifted from the subphase in their original orientations. Conversely, in LS conversion of standing phases to form lying-down phases, each molecule must not only desorb from the aqueous subphase but also reorient substantially to lie horizontal on the substrate (Figure 3.2). Thus, experimental parameters (e.g., temperature, mean molecular area, pH or ionic strength of subphase) [334–336] that produce high transfer ratios [337, 338] for LS transfer of standing phases are not necessarily optimal for LS conversion to form lying-down phases.

Here, we examine the relationship between molecular transfer and expanded or condensed phase regions on the aqueous subphase, by controlling temperature, mean molecular area, substrate dipping rate, and contact time. On the basis of the required reorientation during transfer, we reasoned that LS conversion was likely to be more efficient from expanded phases than from condensed phases in the source Langmuir film; this would be consistent with relatively low surface pressures indicated for previous transfers (e.g.,  $< 10$  mN/m for conversion to lying-down phases on HOPG [15, 16] vs 20–30 mN/m for standing phase LS transfer to substrates such as mica) [339, 340]. However, forming a complete lying-down monolayer requires only a small fraction of

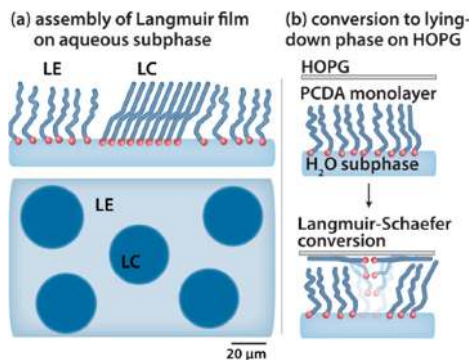


Figure 3.2. (a) Schematic showing molecular assembly of Langmuir film on aqueous subphase with microscale patterns in ordering. (b) Schematic of conversion of molecules from the standing phase Langmuir film into a lying-down phase on HOPG.

the molecules available in a standing phases Langmuir film. Because of this difference from standing phase transfer, we examined a broad range of transfer conditions.

### 3.2 Results and Discussion

#### SEM Characterization of Domain Structure and Ordering in Lying-Down Monolayers on HOPG.

A significant challenge in developing practical control over LS conversion relates to characterization of the transferred film. Lamellar features ( $\sim 6$  nm periodicity) within ordered domains (typically 100–1000 nm) are straightforward to visualize by AFM, and higher-resolution imaging of lamellar substructure can be performed by STM [290]. However, Langmuir films frequently exhibit domain structures on much longer scales (up to 1 mm) [324,325]. Thus, in relating post-transfer domain structures to Langmuir film ordering (Figure 3.3), it would be useful to visualize transferred monolayer structures across the entire range of scales relevant to ordering. Despite the local flatness of HOPG, monolayer structure (film thickness  $< 0.5$  nm) becomes difficult to visualize by AFM at larger scales ( $> 10$   $\mu\text{m}$ ), as contributions from HOPG step edges (0.34 nm/step) and other features begin to dominate image contrast.

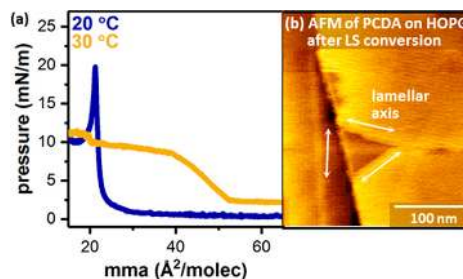


Figure 3.3. (a) Pressure-area isotherms for Langmuir films of PCDA on pure water at 20 °C (blue) and 30 °C (orange). (b) AFM image of typical nanoscopic ordering observed when lamellar phases are assembled on HOPG through LS transfer. White arrows highlight lamellar alignment in epitaxy with HOPG; the feature running from top left to bottom center is a step edge in the HOPG substrate.

Somewhat remarkably, we find that scanning electron microscopy (SEM) can resolve not only noncovalent lying-down domain structures at length scales up to 1 mm comparable to those probed optically in Langmuir films (Figure 3.4a), but also at scales as small as  $\sim 10$  nm, typically accessed by AFM (Figure 3.4b). SEM has been used previously to image standing phase domains (typical thicknesses  $\geq 2$  nm) of alkanethiols on gold [341–343] and phospholipids [344] on  $\text{SiO}_2$ ; however, contrast is typically dominated by ordered standing phases. Here, we resolve not only domain morphologies but also molecular row orientation in much thinner ( $< 0.5$  nm) lying-down organic monolayers on HOPG.

### 3.2.1 Comparison of Transfer from Liquid Expanded and Condensed Phases in Langmuir Films

Here, we compare transfer across a range of mean molecular areas from 100 to  $20 \text{ \AA}^2/\text{molecule}$ , at temperatures of 20 °C (at which there is a collapse point in the isotherm) and at 30 °C (at which the collapse point disappears and there is a rise in surface pressure at much larger mean molecular areas). Figure 3.3a illustrates differences in the isotherms collected at 20 and 30 °C. When molecules are transferred

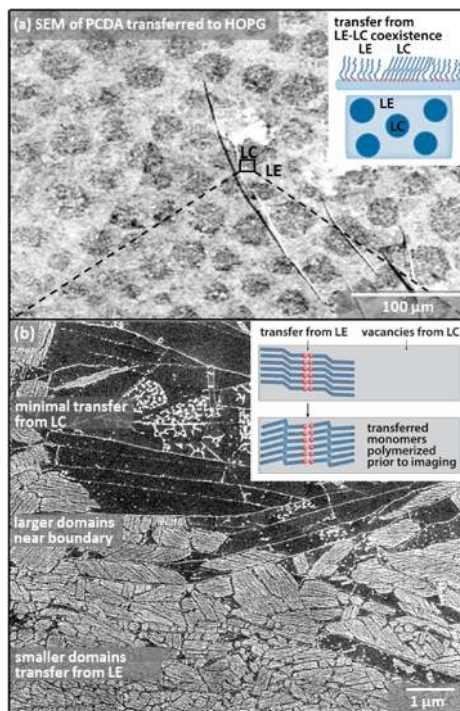


Figure 3.4. (a) SEM images of PCDA film transferred at 30 °C, 30  $\text{\AA}^2$ / molecule and photopolymerized after transfer but prior to SEM imaging. Scale bars represent (a) 100  $\mu\text{m}$  and (b) 1  $\mu\text{m}$ . Image in (b) is acquired from the highlighted region in (a).

from Langmuir films at both temperatures and a range of mean molecular areas, using LS transfer protocols, nanoscopic regions of molecular ordering are observed by AFM, similar to the image shown in Figure 3.3b. In such areas, lamellar axes align in epitaxy with the hexagonal graphite lattice as shown by the white arrows; the linear feature running from top left to center bottom is a step edge in the HOPG substrate.

At microscopic scales, we find correlations between areas of high and low extents of molecular transfer and factors such as local degree of condensation in the Langmuir film. Transfer under conditions corresponding to the LE-LC coexistence segment of the isotherm at 30 °C (Figure 3.3a, yellow trace) enables us to compare molecular transfer from expanded and condensed domains (Figure 3.4). Arrays of circular features with diameters of  $\sim 30\text{--}50 \mu\text{m}$  are visible in the transferred film (Figure 3.4a); interpreted in line with previous fluorescence studies of Langmuir films

of long-chain amphiphiles in the LE-LC coexistence [345,346], circular features would represent condensed phase domains and the surrounding areas expanded phase. Here, higher-resolution SEM imaging at the boundary of one of the circles (Figure 3.4b) reveals that the dark circular areas are predominantly vacant, with small areas of lacy, amorphous film structure and occasional lamellar domains. In contrast, regions transferred from the LE phase (areas around the circles) contain tightly packed, well-ordered lamellar domains. Greater transfer from the expanded phase than from the condensed phase would be consistent with stronger chain-chain interactions in the condensed phase stabilizing the source monolayer and reducing transfer.

In Figure 3.4b, there is a noticeable increase in the average domain size adjacent to the LC vacancy (middle), in comparison with the smaller domains transferred further into the LE phase (bottom). Previous work in submonolayer island nucleation and growth [34] has indicated that the number density of domains,  $N$ , varies with both molecular adsorption rate ( $F$ ) and the rate of molecular diffusion across the substrate ( $D$ ) with

$$N \propto \left( \frac{F}{4D} \right)^{\frac{1}{3}}$$

If the difference in domain size is interpreted in this light, a 4-fold difference in number density could suggest as much as a 64-fold difference in molecular transfer rate from the bulk LE phase in comparison with the LE-LC boundary, if diffusion rates in the two regions after transfer are similar. We do not observe this distinction in all cases at LE-LC boundaries. However, we frequently observe microscale transitions in average domain size, pointing to the capability to create local differences in transfer rate, and thus domain structure, based on local differences in molecular stability on the subphase at the time of transfer.

Because previous studies on Langmuir-Blodgett transfer of standing phase films have indicated that molecule-substrate interactions can be used to modulate assembled film structures [330,347–349], we also examined this possibility. Frequently in such studies, the relatively strong interactions between a polar or ionic headgroup

and an ionic surface such as mica can restructure molecular lattices in comparison with molecular ordering on the aqueous subphase [349, 350]. In the case of the films described here, the  $\pi$ -alkyl interactions that stabilize the lying-down phase are responsible for the most central type of restructuring (creating the striped phase), but we also wondered whether the macroscopic interaction between the descending HOPG and the molecular film on the substrate could be used to modulate local molecular condensation in the Langmuir film. Experimentally, we tested dipping rates from 1 to 300 mm/min (Figure 3.5), measuring at least three areas on at least three different substrates per dipping speed, and find circle diameters of  $140 \pm 40 \mu\text{m}$  at 1 mm/min (Figure 3.5a),  $40 \pm 10 \mu\text{m}$  at 10 mm/min (Figure 3.5b), and  $6.4 \pm 2.6 \mu\text{m}$  at 50 mm/min (Figure 3.5c). Average circle diameters ( $\mu\text{m}$ ) decrease exponentially with the logarithm of the dipping speed (mm/min) as

$$\text{diameter}(\mu\text{m}) = 144e^{-\log(\text{dipspeed})/0.89} - 6.8$$

with  $R^2 = 0.92$ . Together, these results suggest the capability to pattern transfer using a combination of assembly on the aqueous subphase and factors that controllably modulate assembly during transfer.

### 3.2.2 Polymerization-Induced Cracking Reveals Lamellar Directionality.

A key element of the capability to achieve high-resolution SEM images of these sub-nanometer thick lying-down monolayers relates to the topochemical polymerization process and thus illuminates the propensity for polymerization of each domain. Previous literature on the topochemical polymerization of diacetylenes indicates that polymerization requires a high degree of order in the diynes [302, 303, 351]. As mentioned above, the polymerization process can be used either to generate molecular wires in the monolayer [290] or to stabilize it for further processing [319] and thus is a useful property to probe in the context of noncovalent 2D material functionalization.

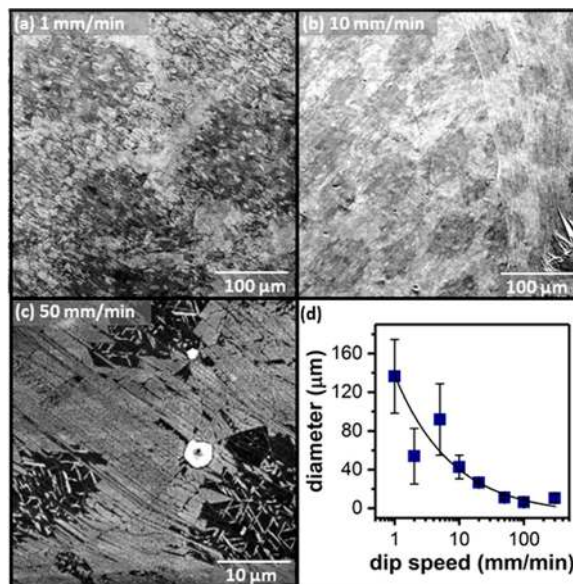


Figure 3.5. SEM images of PCDA film transferred with the substrate lowered onto subphase at (a) 1, (b) 10, and (c) 50 mm/min. (d) Average circle diameters vs dipping speed.

In SEM images acquired at the smallest scales probed (500 nm scale bar, Figure 3.6b) cracking defects are observed within ordered domains, revealing the directionality of the lamellar assemblies. These features are not typically evident in PCDA monolayers imaged by AFM (Figure 3.6a), although we have observed similar features in AFM images of large domains of diynoic phospholipids [322], which have lower surface mobility than PCDA. Such features appear to arise from slight narrowing of ordered lying-down lamellae as the diyne rehybridizes to form the ene-yne during polymerization (Figure 3.6c); such conformational changes are known to occur during polymerization of diynoic acids in the solid state [352,353]. For the experiments here, we have polymerized the PCDA films for 1 h under an 8 W UV lamp, similar to previous descriptions of such processes in the literature [17,315]; the appearance of additional cracking defects under the SEM electron beam would be consistent with additional polymerization events, plausible given the propensity of such molecules to polymerize under both beams of tunneling electrons in an STM [14,315] and X-ray irradiation [354].



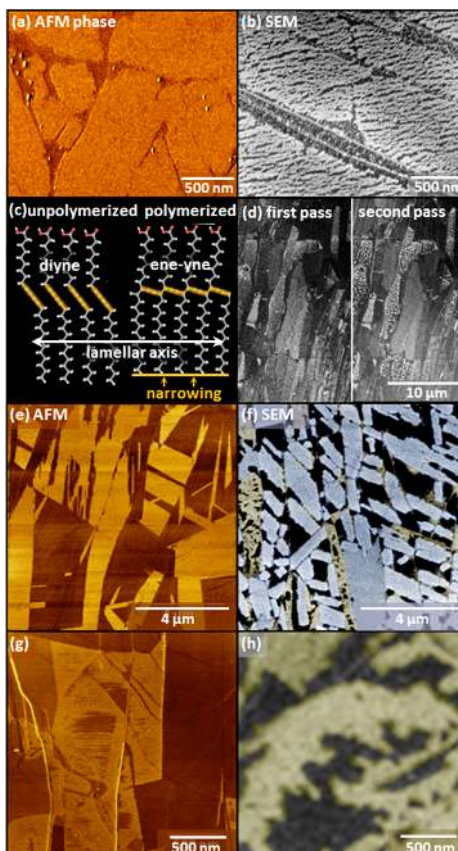


Figure 3.6. (a) AFM and (b) SEM images showing domain structure of PCDA transferred to HOPG and then photopolymerized; cracking defects visible in SEM image. (c) Minimized molecular models showing polymerization-induced lamellar narrowing that leads to cracking in (b). (d) Images illustrating beam-induced formation of dendritic phases in nonpolymerizable domains. (e, f) AFM and SEM images of large-scale domain morphology. (g, h) Comparison of AFM and SEM images of disordered amorphous domains.

Some domains (particularly in films transferred from Langmuir films with large mean molecular areas) do not evolve cracking defects and instead re-form into amorphous (globular, dendritic, or porous) structures during imaging. In Figure 3.6d, repeated imaging of the same area reveals that some domains have re-formed into globular structures, while others have developed cracking defects similar to Figure 3.6b. Overall, our experience suggests that ordered domains have similar gross morphologies in AFM (Figure 3.6e) and SEM (Figure 3.6f), while dendritic or other

amorphous structures in SEM images (Figure 3.6h, and light regions in Figure 3.6f) are correlated with areas of the substrate that appear streaky in AFM images (Figure 3.6g). Presumably these areas lack the high degree of molecular ordering required for topochemical polymerization. We note that in some molecular systems examined previously by others (e.g., standing phases of long-chain phosphonic acids on mica) [35], diffusion of molecules along the substrate following transfer can lead to dendritic domains structures similar to Figure 3.6h directly.

When we have performed SEM imaging of non-diyne fatty acids that have been transferred under conditions similar to those that lead to the circular vacancies shown in Figure 3.4, we observe qualitatively similar features in SEM images; areas of the film that appear to be monolayer exhibit nonlinear defects but do not rapidly evolve into dendritic domains of the type shown in Figure 3.6h. Although further experiments would be necessary to fully establish the behavior of nonpolymerizable films, this suggests that they can be transferred and characterized using techniques similar to those described here.

### **3.2.3 Correlation of Large-Scale Features in Langmuir Films Undergoing Collapse and Transferred Film Structures on HOPG.**

Although LC regions in the source monolayer undergo limited transfer in the LE-LC plateau, tighter molecular packing at or near the Langmuir film collapse point can result in the transfer of many small domains (suggesting rapid transfer) and/or standing phase or multilayer regions. Figure 3.7 compares a Brewster angle microscopy (BAM) image of a Langmuir film at 20 °C and 20 Å<sup>2</sup>/molecule (Figure 3.7a) with SEM images of a film on HOPG transferred under the same conditions (Figure 3.7b,c). In Figure 3.7a, the monolayer has undergone collapse, forming multilayer structures that appear as bright features in the BAM image, due to the large differences in local refractive index they create at the interface. Large-scale SEM images of films transferred under these conditions (Figure 3.7b) reveal bright features similar

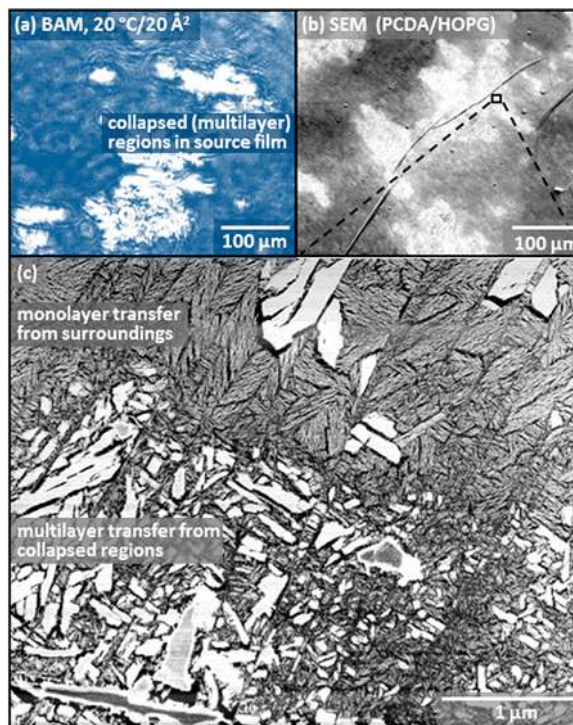


Figure 3.7. (a) BAM image of a Langmuir film of PCDA at 20 °C and 20 Å<sup>2</sup>/molecule. (b, c) SEM images of PCDA films transferred to HOPG under the conditions illustrated in (a) and then photopolymerized. (c) A high-resolution SEM image of the small area of (b) highlighted with a black box.

in terms of geometry and size to islands observed in the BAM image. High-resolution SEM images acquired at the periphery of one of the bright areas (Figure 3.7c) reveal bright rodlike features with characteristic lengths 100–1000 nm and widths 50–500 nm, which, based on increased topographic protrusions in AFM images, appear to be multilayers and standing phase transferred from the collapsed source film. The surrounding surface is occupied by lower contrast lying-down domains. When transfer is carried out at elevated surface pressures just prior to the collapse point (i.e., at conditions similar to those that would typically be used to transfer standing phases to other types of substrates), regions of both standing phase and lying-down phases are transferred. These findings point to the utility of transfer from less densely packed

films when the aim is to establish lying-down phase domains rather than standing phases on the HOPG substrate.

### 3.2.4 Nanoscopic Features in Transferred Films

For many applications (e.g., electronics), it is important not only to control surface chemistry at nanoscopic or microscopic scales but also to create microscopically organized nanostructural elements. Nanoscopic domain structures are not readily imaged using the optical techniques commonly used to illuminate ordering in Langmuir films. However, Langmuir-Blodgett transfer of standing phase lipid rafts with diameters  $< 100$  nm onto mica has been demonstrated previously [355,356], suggesting the feasibility of LS conversion onto materials such as HOPG.

Figure 3.8a illustrates a PCDA film transferred onto HOPG under conditions that produced large-scale Langmuir film structures visible in the BAM image in Figure 3.8b. In the AFM image, hierarchically ordered nanoscopic molecular domains with dimensions 500 nm or less and interdomain spacings of 1–2  $\mu\text{m}$  are arranged at approximately right angles (axes highlighted with white arrows in Figure 3.8a, example domains highlighted with boxes near center), congruent with the larger dendritic features visible in the BAM images (Figure 3.8b). Overall, these microscopically linked nanoscopic structural elements suggest a first step toward more arbitrary molecular pattern transfer, using molecular assembly and phase segregation within Langmuir films, which may be further modulated by the substrate during transfer as shown in Figure 3.5.

Near the top of the image (highlighted by dashed line), the background monolayer structure transitions from complete coverage (top) to a structure with many small (50–100 nm) rounded vacancies. This transition is not correlated with obvious substrate topographical features or the hexagonal symmetry of the HOPG lattice, suggesting the likelihood that the nanoscopic vacancies also arise due to a change in source film packing in the areas above and below the line.

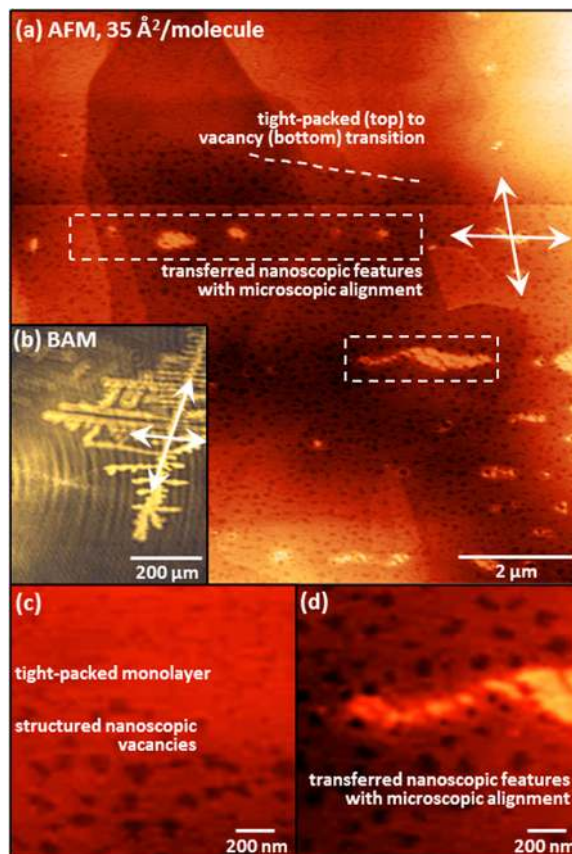


Figure 3.8. (a) AFM images of PCDA transferred to HOPG at 30 °C, 35 Å<sup>2</sup>/molecule and then photopolymerized. Crossed arrow pattern indicates axes of crosshatched pattern of nanoscale domains. White boxes highlight transition from full to monolayer coverage to nanoscopic vacancies (upper left), a representative transferred nanoscopic molecular area (lower right). (b) BAM image of PCDA on aqueous subphase acquired at 35 and 30 Å<sup>2</sup>/molecule, showing larger-scale dendritic pattern. (c) Enlargement of tight-packed/monolayer-vacancy boundary. (d) Enlargement of lower transferred nanoscopic feature highlighted in (a).

### 3.2.5 Identification of Transfer Parameters Leading to High Degrees of Ordered Domain Coverage and/or Large Domain Sizes.

Next, we examined criteria for transferring high surface coverage monolayers with large ordered domains. Transfer of standing phases utilizes relatively high dipping



surface pressures (ca. 30 mN/m for saturated fatty acids) [339, 340, 357] to ensure in-place transfer of a tightly packed, well-ordered film with few defects [338]. In contrast, lying-down phases have typically been transferred at lower pressures [14, 16, 32] consistent with the need for molecules to reorient during transfer. Because of the need for reorientation, temperature also represents a potentially useful parameter for controlling transfer.

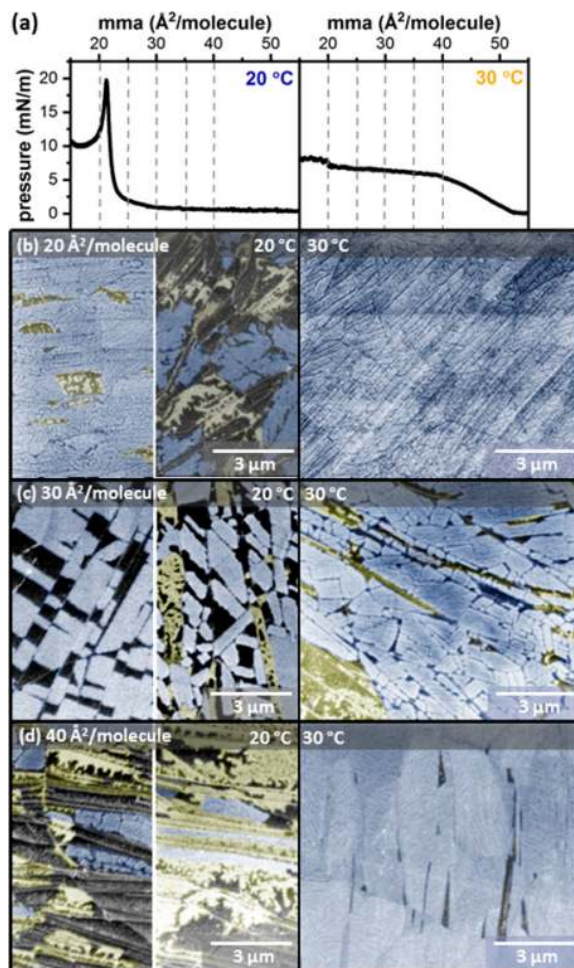


Figure 3.9. (a) Pressure-area isotherms for PCDA transferred from subphases at temperatures of 20 °C (left) and 30 °C (right). (b-d) SEM images of typical PCDA films transferred to HOPG at 20 °C (left) and 30 °C (right), at mean molecular areas of (b) 20, (c) 30, and (d) 40 Å<sup>2</sup>/molecule. Films were photopolymerized after transfer but prior to SEM imaging.

Here, we examined the impacts of both mean molecular area and temperature on transfer. Figure 3.9 compares representative SEM images of molecular transfer at 20 and 30 °C from source films with mean molecular areas of 20–40 Å<sup>2</sup>/molecule. In general, we observe greater transfer efficiency at 30 °C, resulting in large homogeneously functionalized areas of the substrate (Figure 3.9b–d, right).

Figure 4.10 quantifies molecular transfer to HOPG from Langmuir films with mean molecular areas from 20–100 Å<sup>2</sup>/molecule. The transfer ratio—the ratio of molecules transferred vs those present in the Langmuir film—is commonly used to assess the efficiency of LS transfer. Here, we quantify transfer ratios by measuring the HOPG fractional surface coverage of lamellar, amorphous, and standing or multilayer phases of PCDA in SEM images of transferred films and estimating molecular footprints for each type of coverage (see Experimental Methods for more detail).

At both 20 and 30 °C, transfer ratios are fairly low (Figure 3.10b), with values > 0.2 observed only for expanded films (>60 Å<sup>2</sup>/molecule) at 30 °C. Such behavior is not necessarily surprising or undesirable, for two reasons. Only the first lying-down layer of PCDA molecules on HOPG experiences the relatively strong  $\pi$ -alkyl interactions that occur between PCDA alkyl chains and the HOPG basal plane. Thus, there is substantially less energetic driving force for the formation of second (or subsequent) molecular layers during transfer.

Additionally, forming a lying-down monolayer requires very few molecules (1 PCDA/154 Å<sup>2</sup>) in comparison with a standing phase (here, molecular densities as great as 1 PCDA/20 Å<sup>2</sup>). Figure 3.10c illustrates the ratio of molecules available in the source film to those required for a lying-down monolayer (gray traces). At  $\text{mma} = 20 \text{ Å}^2/\text{molecule}$  in the Langmuir film, there are 7.7 as many PCDA molecules available as would be required to form a lying-down layer. Even at 100 Å<sup>2</sup>/molecule, there are 1.54 times as many molecules as required.

We quantify molecules remaining on the subphase after transfer (Figure 3.10c, black lines) by subtracting the total molecular transfer in Figure 3.10d (both structured and amorphous) from the initial average packing density (Figure 3.10c, gray

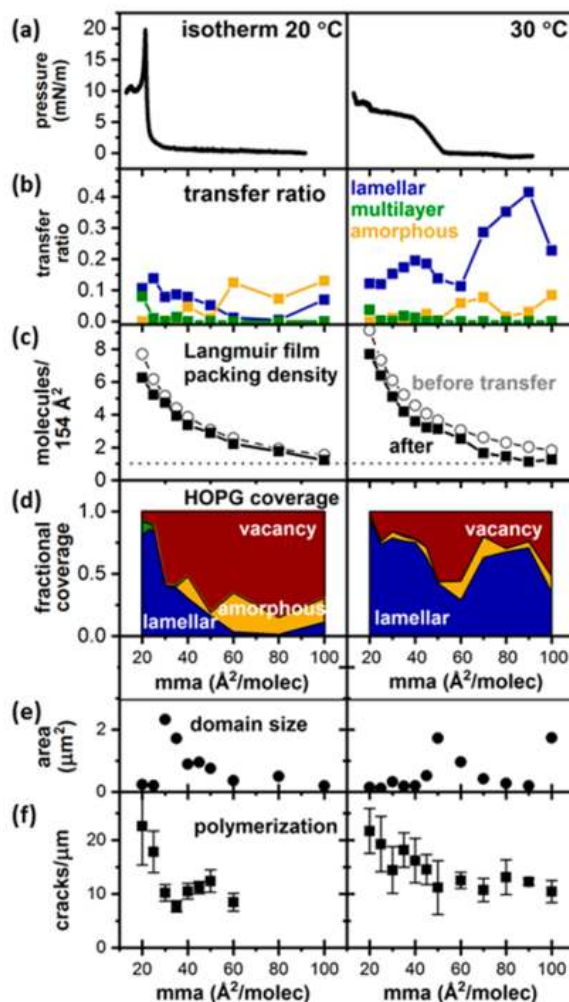


Figure 3.10. Analysis of film transfer at points along isotherms at 20 and 30 °C. (a) Isotherms, (b) transfer ratios, and (c) Langmuir film packing densities (expressed relative to ideal lying-down phase packing densities). (d) HOPG coverage after transfer, expressed as fractional coverage of lamellar (blue), amorphous (gold), and standing or multilayer (green) domain structure, with amount of vacant surface shown in red. (e) Average domain sizes for monolayers on HOPG and (f) polymerization-induced crack densities for monolayers on HOPG, expressed in cracks/ $\mu\text{m}$ .

lines). For all transfers tested, approximately 1 full lying-down monolayer of molecules remains on the aqueous subphase (dotted line on graph), which is reasonable given the high surface tension of water.



Because the goal of this type of transfer is typically to create an ordered molecular layer on HOPG, we next illustrate the fractional surface coverage of ordered, disordered, and standing or multilayer regions on the HOPG (Figure 3.10d). Blue regions in the graphs in Figure 3.10d represent ordered lamellar surface coverage, which is typically the type desired. Ordered coverage decreases rapidly for transfers at 20 °C (left) but remains high for subphase temperatures of 30 °C (right) across much of the range of mean molecular areas tested.

Mean lamellar domain sizes vary with  $\text{mma}$  at transfer (Figure 3.10e), with maxima at  $30 \text{ \AA}^2/\text{molecule}$  at 20 °C and  $50 \text{ \AA}^2/\text{molecule}$  at 30 °C. However, as illustrated in earlier figures, local mean domain sizes can vary substantially across the substrate in areas that contacted condensed or expanded phases in the Langmuir film, meaning that large domains may still be observed under transfer conditions with low mean values.

The ability to polymerize PCDA monolayers is often a significant consideration in promoting stability or achieving desired electronic properties. Thus, we also examined the density of polymerization-induced cracking in SEM images of large lamellar domains as a metric of ordering. Cracking decreases from  $\sim 20 \text{ cracks}/\mu\text{m}$  for densely packed films to  $\sim 10 \text{ cracks}/\mu\text{m}$  for transfers at larger  $\text{mma}$  values (Figure 3.10f), suggesting a somewhat lower degree of molecular ordering in such films.

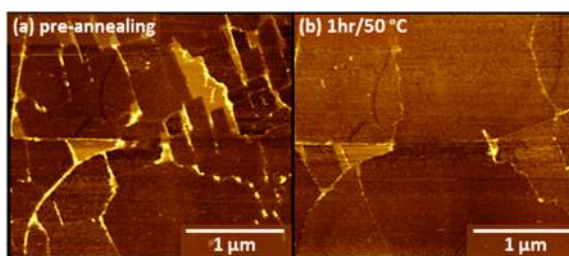


Figure 3.11. AFM images of PCDA film transferred at 20 °C and  $35 \text{ \AA}^2/\text{molecule}$ : (a) as-transferred film structure and (b) same area of film after annealing for 1 h at 50 °C.

Temperature control can also be leveraged after transfer to modulate molecular ordering. Transfer at slightly elevated temperatures (30 °C) produces higher coverage but can also result in smaller domain sizes due to more rapid transfer. Domain sizes in high-coverage transferred films can be further increased by thermal annealing; Figure 11 shows the impacts of post-transfer heating for 1 h at 50 °C. For larger amphiphiles that are less amenable to post-transfer thermal annealing, we have also found that it is possible to perform in situ annealing during transfer to rapidly increase domain sizes [322]. Together, these two strategies provide a means to create large homogeneous domains with high coverage, for applications that benefit from low defect densities.

### 3.3 Conclusion

Using LS conversion, we achieve hierarchical noncovalent patterning on 2D materials, controlling surface functionality on length scales from mm to  $< 10$  nm. Molecular ordering in the Langmuir film influences long-range structure (e.g., circular microscale vacancies or right-angle arrays of nanoscopic domains), while epitaxial assembly on the hexagonal HOPG lattice during LS conversion creates linear functional patterns with sub-10 nm pitch. SEM imaging illuminates not only details of lamellar orientation down to the few-nanometer scale but also differences between domains that are capable of polymerization and those that are not; this capability enables us to probe properties of the interface relevant to structured functionalization and stability at sub-10 nm scales. Polymerizable molecular domains can be assembled with both very high coverage and control over domain size, by controlling subphase temperature, source film packing density, and dipping rate, or by applying post-transfer thermal annealing. Taken together, these capabilities suggest a route for assembling molecular patterns on an aqueous subphase and converting them into striped lying down phases to modulate interactions between a 2D material and its environment. While levying additional requirements in regards to sample preparation, in relationship to other

methods for molecular self-assembly on 2D materials, LS conversion provides an additional level of control for applications in which microscale modulation of assembled structure across the entire substrate is desirable.

### 3.4 Experimentnal Methods

Detailed methods for LS conversion, AFM imaging and energy minimization can be found in Section 2.4. Below contains brief description of procedures followed specifically in this chapter.

**Langmuir-Schaefer Conversion.** LS conversion was performed using the previously describe method. At the target average molecular area (e.g.,  $25 \text{ \AA}^2/\text{molecule}$ ), the HOPG substrate was slowly (2 mm/min, unless otherwise stated in the paper) lowered onto the subphase with the cleaved surface facing down, nearly parallel to the liquid interface, using an automated dipper. Diacetylene-functionalized amphiphile monolayers prepared using the described procedure were photopolymerized prior to imaging in order to improve monolayer stability.

**Brewster Angle Microscopy (BAM).** The laser assembly of the custom-built Brewster angle microscope utilized here incorporates a 635 nm diode laser with variable power (4.5 mW maximum) as a light source. The beam passes through a spot focusing lens aligned along its elliptical axis with a Glan-Taylor polarizer (1000:1 extinction ratio) which passes p-polarized light. The laser assembly is fixed to a tip turn mount for fine X-Y translation of the spot into the optical imaging area; the assembly also incorporates a variable angle fine adjustment to optimize the incident angle of the beam. The entire laser arm is rigidly mounted to the optical imaging arm using a narrow metal beam, minimizing the footprint of the microscope above the trough. The optical imaging arm consists of a long-working-distance objective with a nominal  $10\times$  magnification and an infinity-correcting element that produces a collimated exiting beam. The collimated beam then passes through an extension tube and a linear film polarizer in a rotational mount. Additional extension tubes

and/or lenses may be placed in the beam path to increase the magnification. Image data are collected using a Point Gray Grasshopper 3 CMOS camera with  $2448 \times 2048$  pixel resolution.

**SEM Imaging** All SEM images were obtained on a FEI NOVA NanoSEM field emission SEM. Microscopy was performed at 5 keV accelerating energy at an  $\sim 3$  mm working distance, with an aperture of  $30 \mu\text{m}$  for a current of  $\sim 56$  pA. The substrates were mounted onto a standard  $12.7 \text{ mm} \times 8 \text{ mm}$  SEM pin stub mount with a double-coated carbon conductive tape (Ted Pella, Redding, CA). The substrate was then painted on three edges with PELCO conductive liquid silver paint (Ted Pella, Redding, CA) to increase conductivity from the face of the HOPG to the mount. All images acquired with a magnification  $< 8500\times$  utilized an Everhart-Thornley detector, and those with a magnification  $\geq 8500\times$  utilized a through-the-lens detector (TLD) with an immersion lens.

**AFM Imaging** All AFM measurements were performed under ambient conditions in air using a Bruker (Bruker Instruments, Billerica, MA) MultiMode AFM equipped with an E scanner or Asylum Cypher ES in tapping mode with Mikromasch (Sofia, Bulgaria) HQ:NSC18/AL BS tips (nominal force constant  $2.8 \text{ N/m}$  and radius of curvature  $< 10 \text{ nm}$ ). The cantilever oscillation phase shift was carefully monitored to ensure the tip was engaged in the attractive mode to improve imaging of lamellar structures within domains. The set point ratio was typically maintained between 0.4 and 0.7 and was rarely decreased below 0.4 to avoid tip sweeping effects.

**Image Analysis** Images were processed using Gwyddion [358] scanning probe microscopy data visualization and analysis software [358] and ImageJ analysis software [359] to perform median line corrections, plane flattening, scar artifact removal, and contrast adjustment. For large images (e.g.,  $60 \mu\text{m} \times 70 \mu\text{m}$  SEM images), local variations in contrast across the image area were often large enough to complicate automated segmentation and were not feasible to remove using polynomial background correction; in these cases, local brightness and contrast correction were applied in

Photoshop using guided region selection with automatic edge selection to flatten the background.

## 4. SPATIALLY CONTROLLED NONCOVALENT FUNCTIONALIZATION OF 2D MATERIALS BASED ON MOLECULAR ARCHITECTURE

A version of this chapter has been published in *Langmuir*

DOI: 10.1021/acs.langmuir.8b00553

### 4.1 Introduction

Exceptional physical and electronic properties of 2D materials suggest applications in nanostructured devices including transistors and photovoltaic cells [360–364]. Successful incorporation of 2D materials into such applications often requires precise control of surface chemistry to impart specific functionality. Noncovalent functionalization represents a scalable means of controlling the surface chemistry of 2D materials [10, 11, 365], modulating local electronic properties and interactions with the environment without disrupting extended  $\pi$  conjugation [366, 367]. For instance, long-chain diynoic acids (e.g., 10,12-pentacosadiynoic acid, PCDA) can assemble on highly oriented pyrolytic graphite (HOPG) or graphene with alkyl chains oriented parallel to the graphitic basal plane, creating lamellar functional patterns with a 5–6 nm periodicity [14, 17] (Figure 4.1). Each lamella represents a double row of lying-down molecules with 1 nm wide hydrogen-bonded rows of headgroups (Figure 4.1a). Monolayers are additionally stabilized through van der Waals interactions between adjacent chains and with the substrate, orienting epitaxially with the substrate to produce  $120^\circ$  angles between molecular domains (Figure 4.1a, bottom right). Ordering of the diynes along molecular rows enables topochemical photopolymerization [302, 368].

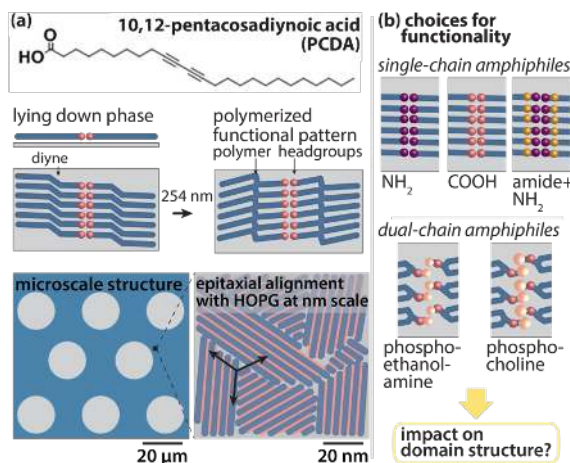


Figure 4.1. (a) Schematic of lying-down phase of PCDA on HOPG and hierarchical nanoscopic and microscopic assembly. (b) Schematic illustrating other amphiphile head and chain architectures for functionalization of 2D materials.

While work of this type has frequently focused on the ene-yne polymers as molecular wires [16, 290], polymerization also improves monolayer robustness [317, 318, 320], potentially important for solution processing. Stabilized monolayers can structure nanoscale interactions with the environment, based on the 1 nm wide rows of functional headgroups [321]. More broadly, the diversity of lipid headgroups (e.g., ethanolamine, choline, and serine) and tails [25] suggests the ability to exercise significant control over interfacial functionality using this approach.

In many applications, it would be useful to localize functionalization to specific regions of the surface and to control the types of functional groups displayed (Figure 4.1b). Biological membranes exhibit substantial structural heterogeneity, dynamically modulating their lipid compositions to pattern surface physicochemical properties in response to specific needs of the cell [36–38]. A rich literature on Langmuir films indicates that it is possible to achieve related molecular patterning in monolayers standing on an aqueous subphase and to transfer such patterns onto solid supports [369–372]. This can be achieved either by drawing a vertically oriented substrate through the monolayer (Langmuir-Blodgett, LB, transfer) or lowering a horizontally

oriented substrate onto the monolayer (Langmuir-Schaefer, LS, transfer). Thus, if molecules are organized into patterns of phase or structure within the Langmuir film, it should be possible to transfer molecules to form lying-down phases retaining spatially encoded patterns.

Here, we examine the relationship between molecular structure and molecular transfer from standing phase Langmuir films to form lying-down phases for noncovalent functionalization of 2D materials. Both LB and LS transfer have classically been used to deposit amphiphiles at high surface pressures (20–30 mN/m) to preserve the initial molecular ordering as standing phases [339, 373, 374]. The ability to preserve or create patterns in this type of direct standing-to-standing LS transfer is well-documented [330]. However, there are also a small number of reports of LS transfer being used to deliberately convert standing phases of diynoic acids into ordered lying-down phases on HOPG. Conversion to form lying-down phases operates substantially differently than direct transfer of standing phases and is usually carried out at lower surface pressures (typically  $< 10$  mN/m) [16, 33]. Even so, the source Langmuir film generally contains 3–7 times as many molecules as required to form a lying-down layer. The first layer of lying-down molecules is the only one to experience alkyl- $\pi$  interactions with the substrate; the limited formation of additional lying-down layers and partial layers observed for some molecules may then relate to the relative stabilities of molecules in the Langmuir film and the lying-down phase.

Most studies of LS conversion to form lying-down phases have examined nanoscopic ordering (scales  $\sim 100$  nm), characterizing structural and electronic properties by scanning tunneling microscopy (STM) for applications in molecular electronics. However, recently, we demonstrated that microscale molecular patterns in standing phase Langmuir films of PCDA can be converted into microscopic patterns of striped lying down phases on 2D materials [31]. Transfer occurs more rapidly from liquid expanded (LE) phases than from more ordered liquid condensed (LC) phases; when the two coexist, this produces round vacancies with controlled diameters 5–100  $\mu\text{m}$  based on transfer conditions [31].



To develop a foundation for designing Langmuir films for conversion to lying-down phases, we compare the LS transfer characteristics of five single- and dual-chain amphiphiles with a range of headgroup chemistries (Figure 4.2). Overall, we find that amphiphiles capable of forming strong lateral interactions (including internal amide H-bonding networks [375, 376]) exhibit more limited transfer, potentially useful for creating controlled vacancies in noncovalent 2D functionalization.

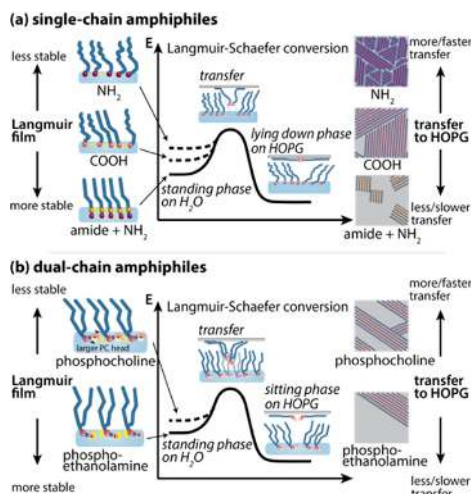


Figure 4.2. Schematic of LS conversion for (a) single-chain amphiphiles and (b) dual-chain amphiphiles, with schematics of expected domain structures (right).

## 4.2 Results and Discussion

### 4.2.1 Preparation and Characterization of Lying-Down and Sitting-Phase Monolayers

During LS conversion, molecules are deposited at the air-water interface and compressed to a desired packing density using moveable barriers. At the desired compression condition, a substrate is slowly lowered horizontally into contact with the interface, allowing a subset of the molecules to transfer to the substrate (Figure 4.2).

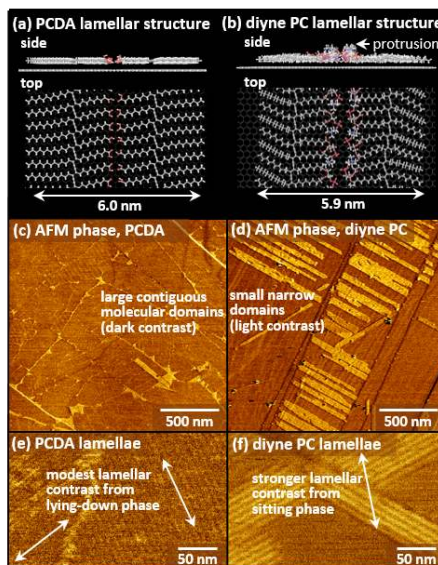


Figure 4.3. (a, b) Lamellar structures of (a) PCDA and (b) diyne PC on HOPG. (c, d) AFM images of nanoscopic domain structure for PCDA and diyne PC on HOPG after LS conversion. (e, f) AFM images showing limited contrast from headgroups in PCDA (e) vs diyne PC (f).

First, we illustrate that molecular structure plays a significant role in LS conversion by comparing transfer of two commercially available polymerizable amphiphiles: PCDA and 1,2-bis(10,12-tricosadiynoyl)-*sn*-glycero-3-phosphocholine (diyne PC). Figures 4.3a and 4.3b illustrate side and top views of monolayers of the two molecules on HOPG. PCDA (Figure 4.3a) adopts a true lying-down structure, while diyne PC (Figure 4.3b) adopts a “sitting” structure in which the terminal functional groups protrude from the monolayer [318]. AFM images of PCDA transferred to HOPG via LS conversion and subsequently photopolymerized (Figure 4.3c,e) reveal nanoscopic domains (dark regions in Figure 4.3c) with edge lengths of 500–1000 nm; higher-resolution imaging (Figure 4.3e) shows modest phase variations along the rows of headgroups in the lying-down phase. In contrast, diyne PC domains are long and narrow (typical dimensions 500 nm  $\times$  50 nm, light areas in Figure 4.3d), with larger contrast variations due to the protruding rows of headgroups (Figure 4.3f).

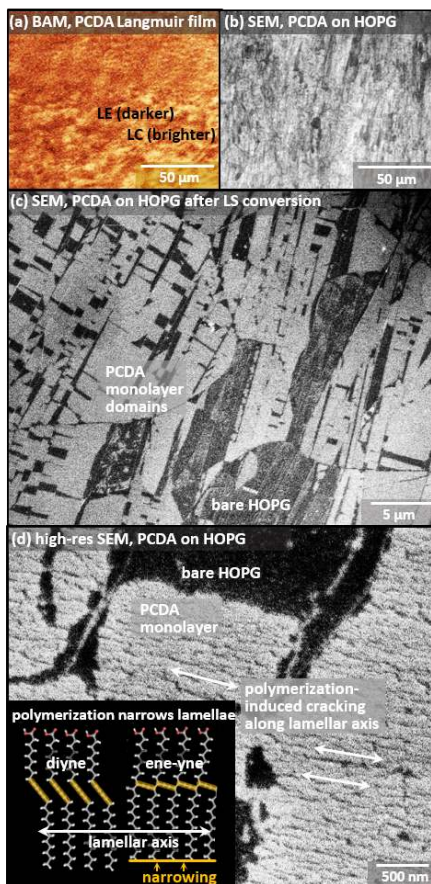


Figure 4.4. (a) BAM image of PCDA Langmuir film compressed to  $30 \text{ \AA}^2/\text{chain}$  at a subphase temperature of  $20^\circ\text{C}$ . (b–d) SEM images of PCDA film on HOPG after LS conversion. Inset in (d) shows molecular model of lamellar narrowing that leads to cracking visible in (d).

Recently, we have demonstrated that SEM imaging enables characterization of transferred domain structures over much larger scales than AFM [31]; here, we use this capability to compare transfer of PCDA (Figure 4.4) and diyne PC (Figure 4.5). Prior to transfer, platelike structures of LE (darker) and LC (brighter) phases of PCDA are visible in the Langmuir film based on Brewster angle microscopy (BAM, Figure 4.3a), which provides contrast based on local differences in refractive index. In SEM images (Figure 4.4b–d) of PCDA transferred to HOPG from a Langmuir film under the conditions shown in Figure 4.4a, transfer varies across the HOPG substrate.

Dark areas represent predominantly vacant areas of HOPG, in which the conductive substrate produces limited scattering of electrons to the detector. Surrounding the dark areas in the image, brighter areas represent lying-down lamellar domains of PCDA. Domain edges commonly align along step edges in the HOPG, creating the long linear features aligned from top to bottom in Figure 4.4c. Cracking defects in the monolayer emerge under the electron beam, highlighting the orientation of rows of molecules (Figure 4.4d; inset shows narrowing of lamellae during polymerization that leads to cracking). Molecular rows in such films are known to align in epitaxy with the HOPG substrate lattice [14, 290], producing the observed hexagonal symmetry. Previously, we have found that liquid condensed (LC) domains in Langmuir films of PCDA exhibit limited transfer in comparison with surrounding liquid expanded (LE) domains when the two coexist [31].

Diyne PC exhibits substantially different Langmuir film structure (Figure 4.5a) and transferred film properties (Figure 4.5b–d). In large-scale SEM images (Figure 4.5b), brighter features are observed at scales commensurate with LE phases visible in BAM images. Higher-resolution SEM images (Figure 4.5c,d) reveal that the brighter areas are indicative of regions of extensive transfer, with very different microscopic morphologies than those transferred from PCDA films. Also in contrast with PCDA, nanoscopic domains of diyne PC assembled under these conditions are much smaller ( $< 60$  nm, Figure 4.5d), with long, narrow domains (Figure 4.5d, right) assembling over areas corresponding to condensed phase regions in the Langmuir film.

Overall, these findings point to both substantial differences in transfer with molecular structure and the broad capability to create controlled vacancies on a 2D material surface during noncovalent functionalization, based on structure-dependent transfer from a Langmuir film with local differences in molecular ordering.

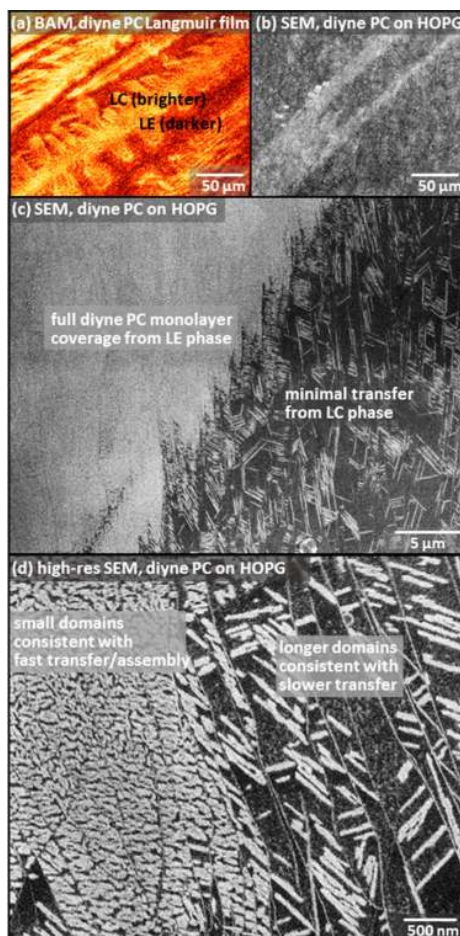


Figure 4.5. (a) BAM image of diyne PC Langmuir film compressed to  $30 \text{ \AA}^2/\text{chain}$  at a subphase temperature of  $20^\circ\text{C}$ . (b–d) SEM images of diyne PC film on HOPG after LS conversion illustrating local differences in extent of molecular transfer and domain shapes.

#### 4.2.2 Comparison of LS Transfer Efficiency with Molecular Structure.

To further examine the relationship between molecular structure and LS transfer efficiency, we compared transfer of amphiphiles with different polar headgroup architectures that would be expected to impact condensation in Langmuir films. The three single-chain polymerizable amphiphiles utilized are shown in Figure 6: 10,12-pentacosadiyn-1-amine (PCD-NH<sub>2</sub>), 10,12-pentacosadiynoic acid (PCDA), and N-(2-aminoethyl)-10,12-diynamide (NAPDA). We then additionally compared transfer

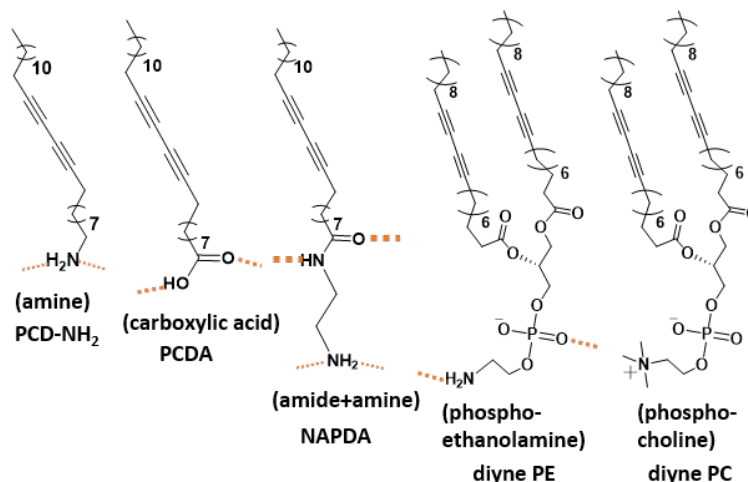


Figure 4.6. Chemical structures of the five amphiphiles used in LS transfer experiments (from left to right): PCD-NH<sub>2</sub>, PCDA, NAPDA, diyne PE, and diyne PC.

results with those for two dual-chain phospholipids with polyfunctional headgroups: 1,2-bis(10,12-tricosadiynoyl)-*sn*-glycero-3-phosphoethanolamine (diyne PE) and 1,2-bis(10,12-tricosadiynoyl)-*sn*-glycero-3-phosphocholine (diyne PC).

Attractive lateral interaction strengths for the single chain amphiphiles are expected to vary as  $E_{PCDNH_2} < E_{PCDA} < E_{NAPDA}$ ; because they have the same parent chain structure, this ordering is based on the lower strength of NH<sub>2</sub> H-bonding interactions vs COOH interactions (2.3 kcal/mol·H-bond (CH<sub>3</sub>NH<sub>2</sub> ··· CH<sub>3</sub>NH<sub>2</sub>) [377,378] vs 7–8 kcal/mol·H-bond (CH<sub>3</sub>COOH dimer)) [379] and the additional stability conferred by lateral H-bonding between NAPDA amides (5–7.3 kcal/mol, CH<sub>3</sub>CONHCH<sub>3</sub> ··· CH<sub>3</sub>CONHCH<sub>3</sub>) [380]. Headgroup-water interactions follow a similar trend [380–382]. Amine and carboxylic acid headgroups may also ionize, though  $pK_a$  shifts in Langmuir films decrease charge density for both groups [383,384]. Overall, because lateral interactions between headgroups can promote condensation, leading to increased chain-chain interactions, we would predict lateral interaction strength to be an important contributing factor in molecular transfer.



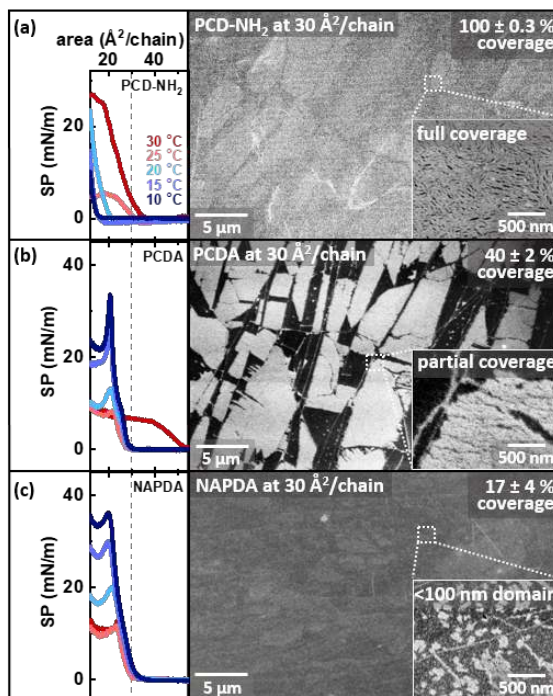


Figure 4.7. Isotherms of Langmuir films of single-chain amphiphiles from 10–30  $^{\circ}\text{C}$  (left) and SEM images of molecules assembled on HOPG after LS transfer at 20  $^{\circ}\text{C}$ , 30  $\text{\AA}^2/\text{chain}$  (right), for the following amphiphiles: (a) PCD-NH<sub>2</sub>, (b) PCDA, and (c) NAPDA. Insets show nanoscale domain structures. Color codes for temperatures shown in (a) are the same for each panel.

The predicted ordering of lateral interaction strength is consistent with changes in isotherms observed with increasing temperature. PCD-NH<sub>2</sub>, predicted to experience relatively weak lateral interactions, exhibits shifts in its lift-off point with increasing temperature, from 15  $\text{\AA}^2/\text{chain}$  at  $\leq 15$   $^{\circ}\text{C}$  to 22  $\text{\AA}^2/\text{chain}$  at 20  $^{\circ}\text{C}$  (Figure 4.7a, left); at 25  $^{\circ}\text{C}$ , the isotherm begins to exhibit a plateau. In contrast, collapse points are easily identifiable for PCDA up to 20  $^{\circ}\text{C}$  (Figure 4.7b, left); plateaus appear at 30  $^{\circ}\text{C}$ . NAPDA, predicted to have the strongest lateral interactions among the three single-chained amphiphiles, retains equivalent lift-off points in isotherms at all temperatures tested, although the surface pressure of the collapse point decreases at elevated temperatures (Figure 4.7c, left), as for PCDA.

Percent surface coverages of transferred molecules on HOPG were measured from SEM images (acquired in three macroscopically separated areas of 1–2 samples, with representative images shown in Figure 4.7a–c, right). Coverages were consistent with the prediction that weaker lateral interactions in Langmuir films lead to facile transfer, presumably by increasing disordering in the terminal regions of the alkyl chains and facilitating initial contact with the HOPG. For similar transfer conditions (Langmuir film densities of  $30 \text{ \AA}^2/\text{chain}$  and subphase temperatures of  $20 \text{ }^\circ\text{C}$ ), average transferred coverages of single-chain amphiphiles to HOPG were  $C_{PCDNH_2/HOPG} (100 \pm 0.3 \%) > C_{PCDA/HOPG} (40 \pm 2 \%) > C_{NAPDA/HOPG} (17 \pm 4 \%)$ .

Transfer results for phospholipids are also consistent with strong lateral interactions between molecules decreasing transfer. Two factors may contribute in this case: first, lateral hydrogen-bonding networks are possible for PE (but not PC) [41, 385], with reported interaction strengths similar to those estimated for the lateral H-bond networks formed by NAPDA ( $\sim 7.2 \text{ kcal/mol}\cdot\text{H-bond}$ , based on  $\text{CH}_3\text{NH}_2 \cdots \text{HPO}_4(\text{CH}_3)_2$ ) [386]. Although both phospholipids interact through charge pairing and water bridging [387, 388], these interactions are also expected to be stronger for diyne PE [389]. Moreover, the bulky quaternary tetramethylammonium in the choline headgroup introduces steric clashes at high packing densities ( $50 \text{ \AA}^2/\text{PC head}$  vs  $39 \text{ \AA}^2/\text{PE head}$ ) [390, 391] and incurs additional entropic costs when submerged in water [388, 392].

The minimal changes in PE isotherms collected from  $10\text{--}30 \text{ }^\circ\text{C}$  (Figure 4.8a, left) are congruent with enhanced film stability in comparison with diyne PC, which exhibits significant changes in isotherm shape at  $25 \text{ }^\circ\text{C}$  (Figure 4.8b, left). Similar to the single-chain amphiphiles, strong lateral interactions are correlated to lower molecular coverages on HOPG after transfer from Langmuir films at  $30 \text{ \AA}^2/\text{chain}$ ,  $20 \text{ }^\circ\text{C}$ :  $C_{diynePC} (65 \pm 20 \%) > C_{diynePE} (19 \pm 10 \%)$ . Differences in domain shapes and sizes are evident in the transferred films, even at similar coverage (e.g., PCDA vs diyne PC, Figures 4.7b and 4.8b), which is considered in more detail below.



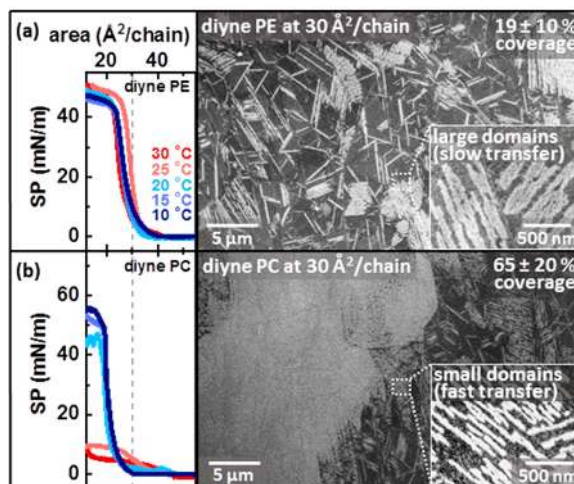


Figure 4.8. Isotherms of Langmuir films of phospholipids from 10–30 °C (left) and SEM images of molecules assembled on HOPG after LS transfer at 20 °C, 30 Å<sup>2</sup>/chain (right), for the following amphiphiles: (a) diyne PE and (b) diyne PC. Insets show nanoscale domain structures. Color codes for temperatures shown in (a) are the same for each panel.

LS transfer efficiency of phospholipids can be modulated based on molecular packing densities and ion-lipid interactions, similar to our previous observations for PCDA. Performing LS conversion from Langmuir films with a range of mean molecular areas from 22–60 Å<sup>2</sup>/molecule, we observe differences in the transfer across the range of packing densities (Figure 4.9). We compare these in terms of transfer ratio ( $\alpha$ ), the parameter classically used to quantify LS and LB transfer efficiency; we also examine the fraction of the HOPG surface covered with ordered lamellar domains ( $\chi_{\text{lamellar}}$ ), amorphous domains ( $\chi_{\text{amorphous}}$ ), and standing phase domains ( $\chi_{\text{standing}}$ ), which is relevant to the subsequent utility of the noncovalently functionalized 2D material.

Figure 4.9a shows isotherms for diyne PE (left) and diyne PC (right) with mean molecular areas evaluated in Å<sup>2</sup>/chain to facilitate comparison with single-chain amphiphiles. To illustrate why relatively low transfer efficiencies in LS conversion can actually be desirable (unlike in classical LS transfer of standing phases), in Figure 4.9b we graph the density of molecules available in the Langmuir film in comparison

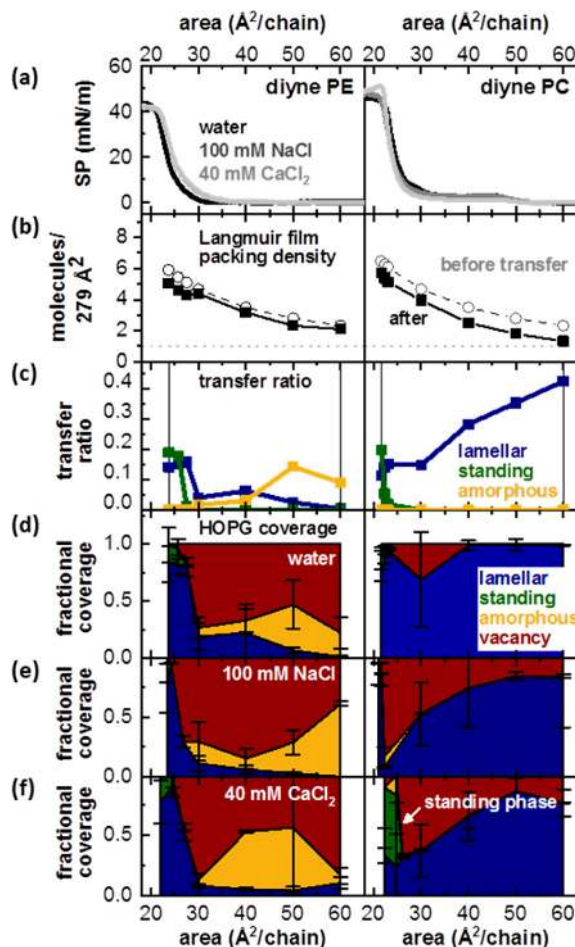


Figure 4.9. (a) Isotherms for diyne PE (left) and diyne PC (right) on subphases of pure water, 100 mM NaCl, and 40 mM  $\text{CaCl}_2$ . (b) Langmuir film packing density, expressed as a ratio with the number of molecules required to form a full lying-down phase. (c) Transfer ratios for molecules undergoing LS transfer from a pure water subphase onto HOPG, with lamellar (blue), amorphous (yellow), and standing (green) phases quantified individually. (d–f) Fractional surface coverage of diyne PE (left) and diyne PC (right) on HOPG after transfer from subphases composed of (d) pure water, (e) 100 mM NaCl, and (f) 40 mM  $\text{CaCl}_2$ .

with the molecular density in a complete lying-down monolayer of phospholipid (1 molecule/ $279 \text{ \AA}^2$ ). In the most expanded films probed, the average molecular density in the Langmuir film is  $\sim 2.5$  times that required to form a lying-down monolayer, increasing to a nearly 6-fold excess in the most compressed films.

For a pure water subphase,  $\alpha_{lamellar, dienePE} < 0.2$  under all compression conditions tested (Figure 4.9c left, blue line), while lamellar, diene PC ranges from 0.15 to 0.4 (Figure 4.9c right, blue line). Considered in terms of fraction of the HOPG surface that is functionalized with each phase,  $(\chi_{lamellar}), diene PE \sim 80$  transfers from the most tightly packed Langmuir films tested ( $< 30 \text{ \AA}^2/\text{chain}$ , Figure 4.9d left, blue area of graph), but at these packing densities, there is also a significant amount of standing phase transferred (green). Transfer from Langmuir films with mean molecular areas  $\geq 30 \text{ \AA}^2/\text{chain}$  results in  $(\chi_{lamellar}), diene PE < 20 \%$ . In contrast, for diene PC, nearly complete lamellar coverage is achieved across most Langmuir film packing densities tested (Figure 4.9d right, blue area of graph), with a minimum  $(\chi_{lamellar}), diene PC \sim 75 \%$  coverage at  $30 \text{ \AA}^2/\text{chain}$ . The overall trend of decreased transfer with increased packing density, followed by a final increase in transfer at the highest packing densities, is consistent with our previous observations of PCDA transfer [31, 31].

We also examined the possibility of introducing cations into the subphase as a means to turn off molecular transfer by inducing condensation through ion-pairing with negatively charged moieties in the phospholipid headgroups. Two electrolyte solutions—100 mM NaCl and 40 mM  $\text{CaCl}_2$ —were utilized. Stabilization of the Langmuir film through ion-lipid interactions reduced  $(\chi_{lamellar})$  for both diene PE and diene PC (Figure 4.9e,f, blue areas of graph). In the most compressed Langmuir films of diene PC ( $< 25 \text{ \AA}^2/\text{chain}$ ),  $\text{Ca}^{2+}$  ions (which form stable ion-lipid complexes [393–395]) increased  $(\chi_{standing})$  above 50 % (Figure 4.9f, right, green area) from  $\sim 10 \%$  for pure water subphases (Figure 4.9d, right, green area).

Overall, this may suggest that weakly condensing ions such as  $\text{Na}^+$  are more effective agents for inducing structured vacancies in monolayers without promoting transfer of (typically unwanted) standing phases in noncovalent functionalization of 2D materials.

Conversely, the extent of transfer may be increased either mechanically, by increasing the rate at which the dipper brings the HOPG substrate into contact with the subphase [31], or thermally, using an in situ thermal annealing process we have

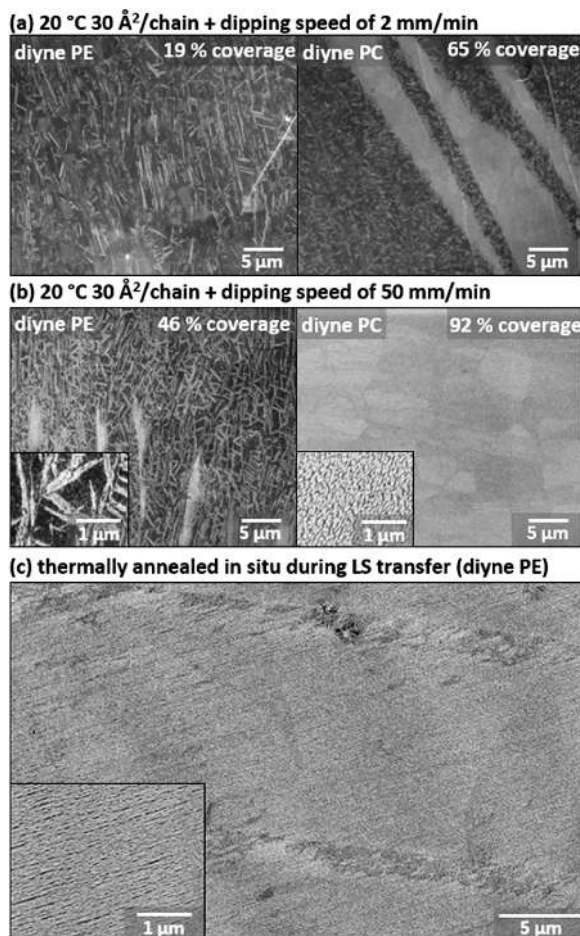


Figure 4.10. SEM images of diene PE (left) and diene PC (right) transferred at 20 °C and 30 Å<sup>2</sup>/chain using a dipping speed of (a) 2 mm/min and (b) 50 mm/min. (c) SEM image of diene PE prepared via in situ thermal annealing. The subphase, aqueous 5 mM MnCl<sub>2</sub> solution, was heated to 30 °C while the substrate was also heated to 70 °C throughout deposition.

demonstrated previously [322]. Figure 4.10a,b illustrates that increasing the rate at which the dipper comes into contact with the subphase from 2 to 50 mm/min increases transfer efficiency by more than 2-fold for diene PE; under these conditions, lamellar coverage of diene PC exceeds 90 %. Figure 4.10c illustrates that full coverage can be achieved for diene PE as well, when the temperatures of the substrate and subphase are raised to induce thermal annealing effects.

### 4.2.3 Adsorption, Diffusion, and Nucleation Rates Modulate Domain Structure.

After transfer to the HOPG, molecules diffuse across the substrate until they either join a growing molecular domain or nucleate a new domain. As a result, diffusion rates and critical nucleus sizes also modulate structures in molecular films during LS transfer. Previous studies of submonolayer island nucleation and growth have indicated that the relative rates of adsorption ( $F$ ) and diffusion ( $D$ ) influence the number density of domains on the surface ( $N$ ) [34], with

$$N \propto \left( \frac{F}{4D} \right)^{\frac{1}{3}}$$

Thus, rapid adsorption (e.g., via rapid transfer from weakly ordered areas of Langmuir films) should promote high values of  $N$ , while rapid diffusion (e.g., smaller or more weakly adsorbed molecules) promotes the formation of larger domains and a lower value of  $N$ . While differences in molecular structure can impact both LS transfer rates and diffusion rates, comparing values of  $N$  for pairs of molecules across a range of surface coverage enables us to estimate bounds on the parameters if they varied individually. Smaller critical nuclei (i.e., number of molecules required to nucleate a domain) also result in larger values of  $N$ . We note that surface defects such as HOPG step edges can also serve as nucleation sites.

Representative AFM images of the three single-chain amphiphiles (PCD-NH<sub>2</sub>, PCDA, and NAPDA) are shown in Figure 4.11a. On the basis of our observation that stronger lateral intermolecular interactions limit transfer, we would expect adsorption rates  $F_{PCDNH_2} > F_{PCDA} > F_{NAPDA}$ , meaning that  $N_{PCDNH_2} > N_{PCDA} > N_{NAPDA}$ , if diffusion rates and critical nucleus sizes are similar. This trend appears to be borne out by the high density of very small domains for PCD-NH<sub>2</sub>;  $N_{PCDNH_2}$  is not quantified in the graphs in Figure 4.11b since domain boundaries are not always well-resolved but is typically  $> 10/\mu m^2$  vs values 0.01–1/ $\mu m^2$  for PCDA. If diffusion rates

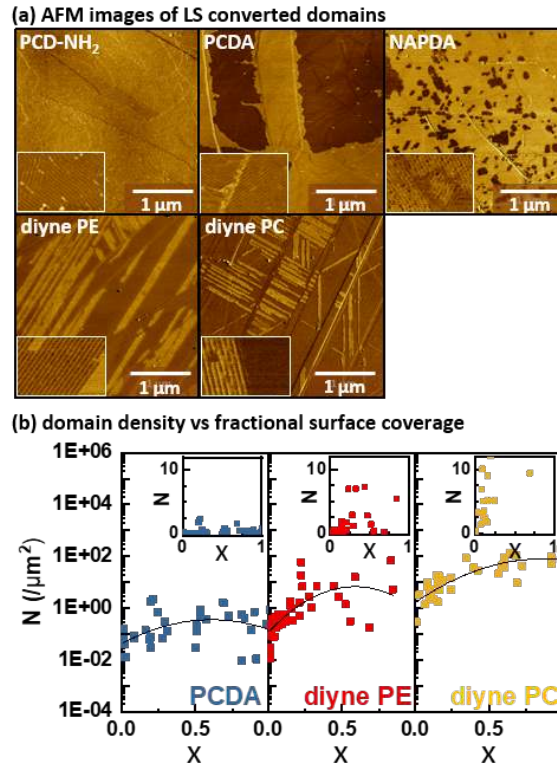


Figure 4.11. (a) Representative AFM images of domain structures of PCDA, PCD-NH<sub>2</sub>, NAPDA, diyne PE, and diyne PC. Insets ( $80 \text{ nm} \times 120 \text{ nm}$ ) show nanoscopic lamellar structure and domain edges. (b) Number density of domains ( $\log(N)$ ) vs fractional surface coverage for PCDA (blue), diyne PE (red), and diyne PC (yellow). Insets illustrate the portion of the vertical scale from 0 to 11.

and domain nucleus sizes are similar,  $N_{PCDNH_2} \approx 10 \times N_{PCDA}$  would imply as much as a 1000-fold greater transfer rate for PCD-NH<sub>2</sub> in comparison with PCDA.

Interestingly, although the extent of transfer for NAPDA is very low, presumably leading to  $F_{NAPDA} < F_{PCDA}$ , NAPDA forms very small domains ( $\sim 60 \text{ nm} \times 60 \text{ nm}$ ), leading to a high value of  $N_{NAPDA}$  ( $> 30/\mu\text{m}^2$ ). At least two possibilities may account for this difference. First, the same lateral H-bonding interactions that stabilize NAPDA in the Langmuir film may contribute to smaller critical nuclei on HOPG, increasing the probability of nucleating small domains. Second, NAPDA

Langmuir films may produce points with high transfer rates, either due to defects in the source film or possibly due to coupled transfer events.

Diffusion rates of large, dual-chain phospholipids (e.g., diyne PE, diyne PC) are expected to be lower than those of single-chain amphiphiles (e.g., PCDA). Critical nucleus sizes should also be lower, both factors favoring larger values of  $N$ . On the basis of previously reported molecular dynamics simulations of alkanes on HOPG [396–398], we estimate diffusion coefficients of  $\sim 4.0 \mu\text{m}^2/\text{s}$  for 25 carbon PCDA and PCD-NH<sub>2</sub> monomers and  $\sim 2.3 \mu\text{m}^2/\text{s}$  for 27 carbon NAPDA. The value for PCDA is  $\sim 300$ -fold higher than diffusion coefficients estimated for the phospholipids utilized here ( $\sim 0.013 \mu\text{m}^2/\text{s}$ , based on two 23 carbon tails), using a similar approach. This would suggest that differences in diffusion could contribute to up to a 7-fold smaller value of  $N_{PCDA}$  vs  $N_{diynePE}$  and  $N_{diynePC}$ . Figure 4.11a shows representative AFM images illustrating domain structures for PCDA and diyne PE, consistent with predicted differences in domain structure.

Figure 4.11b graphs local average domain sizes for PCDA (blue), diyne PE (red), and diyne PC (yellow) across a range of surface coverages ( $\chi$ ). Although there is clearly a broad distribution of domain sizes across the range of fractional surface coverage, polynomial fits illustrate larger values of  $N$  for phospholipids (particularly diyne PC) in comparison with PCDA:

$$\log(N_{PCDA}) = -2.5x_{PCDA}^2 + 3.1x_{PCDA} - 1.4$$

$$\log(N_{diynePE}) = -5.2x_{diynePE}^2 + 6.1x_{diynePE} - 0.9$$

$$\log(N_{diynePC}) = -2.3x_{diynePC}^2 + 3.9x_{diynePC} + 0.2$$

Overall, we typically observe a 1–2 order of magnitude larger density of domains for diyne PC than for PCDA.

Conversely, diyne PE and diyne PC would be predicted to have similar surface diffusion rates and critical nucleus sizes based on structural similarities. However, the results presented above indicate that diyne PC transfers to HOPG more extensively

than diyne PE across a range of transfer conditions. Comparing domain number density versus coverage for the two molecules reveals an  $\sim 4$ -fold larger value of  $N$  for diyne PC (at fractional coverages below 0.5), suggesting as much as a 64-fold difference in local transfer rates in areas with similar extents of coverage.

### 4.3 Conclusions

We have shown that molecules that can participate in lateral hydrogen-bonding networks exhibit reduced transfer efficiency in LS conversion to form lying-down phases on 2D materials. In particular, areas of condensed phases in the Langmuir film result in very little molecular transfer, allowing condensed phase patterns to produce controlled vacancies on noncovalently functionalized 2D materials. Condensed phases can be created through appropriate combinations of molecular structure, Langmuir film packing densities, and ions in the subphase. Molecular structure also impacts domain assembly after adsorption. Large molecules with lower diffusion rates or molecules with strong intermolecular interactions with the potential to decrease critical nucleus size typically form smaller molecular domains. Together, these findings suggest the possibility of tailoring microscopic and nanoscopic noncovalent functionalization by controlling molecular structure in the noncovalent chemical patterns created by polymerizable amphiphiles on 2D substrates.

### 4.4 Experimental Methods

Detailed procedure for LS conversion, AFM imaging, SEM imaging, image analysis and energy minimization is given in section 2.4 and 3.4.

**Materials** 10,12-Pentacosadiynoic acid (PCDA), chloroform, ethylamine, oxalyl chloride, tetrahydrofuran (THF), lithium aluminum hydride, N-hydroxysuccinimide, N-(3-(dimethylamino)- propyl)-N-ethylcarbodiimide hydrochloride, and ammonium hydroxide were purchased from Sigma-Aldrich (St. Louis, MO) and used as received. Methanol, diethyl ether, dichloromethane (DCM), tetrahydrofuran (THF),



ethyl acetate, ammonium chloride, sodium bicarbonate, sodium sulfate, sodium chloride, manganese chloride, and magnesium sulfate were purchased from Fisher (Fair Lawn, NJ) and used as received. Silica gel was purchased from Machery Nagel (Bethlehem, PA) and used as received. 1,2-Bis(10,12-tricosadiynoyl)-sn-glycero-3-phosphocholine (diyne PC, > 99 % purity) and 1,2-bis(10,12-tricosadiynoyl)-sn-glycero-3-phosphoethanolamine (diyne PE, > 99 % purity) were purchased from Avanti Polar Lipids (Alabaster, AL). PCDA was filtered before use, using a 13 mm syringe filter with a PTFE membrane and 0.2  $\mu\text{m}$  pores (VWR, Radnor, PA). Highly oriented pyrolytic graphite substrates (HOPG ZYB grade; MikroMasch, Watsonville, CA) were used for all experiments. PELCO conductive liquid silver paint, standard SEM pin stub mounts, and double-coated carbon conductive tape were purchased from Ted Pella (Redding, CA). Synthesis of 10,12-Pentacosadiynamine (PCD-NH<sub>2</sub>). The twostep reaction was adapted from a protocol reported previously [399]. In a typical reaction, PCDA (1.88 mmol) was dissolved in DCM (25 mL) followed by the addition of oxalyl chloride (26.33 mmol) under a nitrogen atmosphere. Several drops of DMF were added, and the mixture was stirred at room temperature overnight. Subsequently, the solvent was removed, and the crude product was dissolved in dry THF (25 mL). This solution was then added dropwise into a solution of 38 mL of ammonium hydroxide (25 %) in an ice bath overnight. The solvent was evaporated, extracted with DCM three times, and dried over MgSO<sub>4</sub>. The product isolated from the reaction described above was dissolved in 100 mL of diethyl ether in an ice bath. LiAlH<sub>4</sub> (17.9 mmol) was added to the chilled solution. The solution was stirred overnight, and the organic layer was extracted with a saturated NH<sub>4</sub>Cl solution. The aqueous layer was then extracted with ethyl acetate. Both organic layers were combined and dried over MgSO<sub>4</sub>. The filtered residue was purified with a silica column with an initial mobile phase of 9:1 CHCl<sub>3</sub>:MeOH followed by 2 % ammonium hydroxide in 9:1 CHCl<sub>3</sub>:MeOH.

**Synthesis of N-(2-Aminoethyl)pentacosa-10,12-diynamide (NAPDA)** The reaction was adapted from previously reported protocols [400,401]. In a typical reac-

tion, N-hydroxysuccinimide (1.64 mmol) and N-(3-diamethylaminopropyl)-N-ethylcarbodiimide hydrochloride (3.1 mmol) were dissolved in DCM (8 mL) and added to a solution of PCDA (1.37) in DCM (8 mL) dropwise. The reaction mixture was stirred in an ice bath for 12 h, then poured into DCM (80 mL), and extracted with water ( $4 \times 40$  mL). The organic layer was dried over  $\text{Na}_2\text{SO}_4$ , and the residue was dried using rotary evaporation. The crude product (1.16 mmol) was dissolved in DCM (11 mL) and added dropwise to a solution of ethylenediamine (6.07 mmol) in DCM (4 mL). The reaction mixture was stirred at room temperature for 4 h, after which the reaction was poured into DCM (100 mL) and extracted with saturated sodium carbonate (100 mL) followed by distilled water ( $4 \times 50$  mL). The organic layer was then dried over  $\text{Na}_2\text{SO}_4$  and purified using column chromatography with 20:1 DCM:MeOH as an eluent to afford NAPDA.

**Langmuir-Schaefer Transfer** HOPG substrates were freshly cleaved immediately prior to sample deposition. All sample preparation steps were performed using a KSV-NIMA Langmuir–Blodgett trough (Biolin Scientific, Stockholm, Sweden) under UV-filtered light to prevent polymerization in solution. For the deposition of amphiphiles, 18  $\mu\text{L}$  of 0.5 mg/mL chloroformic solution of the desired amphiphile was deposited on a subphase of deionized water ( $\sim 18 \text{ M}\Omega\cdot\text{cm}$ ), aqueous 100 mM NaCl, or aqueous 40 mM  $\text{CaCl}_2$ . The trough barriers were swept inward to reach the target mean molecular area. the freshly cleaved side of the HOPG was brought into contact with the subphase. All samples were photopolymerized with a 254 nm 8 W UV lamp for 60 min.

**In Situ Thermal Annealing** A freshly cleaved HOPG substrate was placed on a custom heated dipping attachment and heated to 60 °C. Langmuir film preparation was carried out similar to the procedure described above, with the following modifications: 30  $\mu\text{L}$  of 0.50 mg/mL of chloroformic diyne PE solution was deposited onto a 5 mM  $\text{MnCl}_2$  subphase. The subphase temperature was maintained at 30 °C. After 30 min of evaporation time, the barriers were compressed at 3 mm/min to reach a target surface pressure of 30 mN/m. The substrate was brought into contact with the

surface at 4 mm/min and maintained in contact for 1 min prior to being withdrawn from contact with the subphase.

## REFERENCES

- [1] S Z Butler, S M Hollen, L Y Cao, Y Cui, J A Gupta, H R Gutierrez, T F Heinz, S S Hong, J X Huang, A F Ismach, E Johnston-Halperin, M Kuno, V V Plashnitsa, R D Robinson, R S Ruoff, S Salahuddin, J Shan, L Shi, M G Spencer, M Terrones, W Windl, and J E Goldberger. Progress, Challenges, and Opportunities in Two-Dimensional Materials Beyond Graphene. *ACS nano*, 7(4):2898–2926, 2013.
- [2] A K Geim. Graphene: status and prospects. *Science (New York, N.Y.)*, 324(5934):1530–1534, 2009.
- [3] Chul-Ho Lee, Gwan-Hyoung Lee, Arend M. van der Zande, Wenchao Chen, Yilei Li, Minyong Han, Xu Cui, Ghidewon Arefe, Colin Nuckolls, Tony F. Heinz, Jing Guo, James Hone, and Philip Kim. Atomically thin pn junctions with van der Waals heterointerfaces. *Nature Nanotechnology*, 9(9):676–681, 9 2014.
- [4] Branimir Radisavljevic, Michael Brian Whitwick, and Andras Kis. Integrated Circuits and Logic Operations Based on Single-Layer MoS<sub>2</sub>. *ACS Nano*, 5(12):9934–9938, 12 2011.
- [5] Shuping Pang, Yenny Hernandez, Xinliang Feng, and Klaus Müllen. Graphene as Transparent Electrode Material for Organic Electronics. *Advanced Materials*, 23(25):2779–2795, 7 2011.
- [6] F N Xia, H Wang, D Xiao, M Dubey, and A Ramasubramaniam. Two-dimensional material nanophotonics. *Nature Photonics*, 8(12):899–907, 2014.
- [7] Oleksandr V. Mikhnenko, Paul W. M. Blom, and Thuc-Quyen Nguyen. Exciton diffusion in organic semiconductors. *Energy & Environmental Science*, 8(7):1867–1888, 7 2015.
- [8] Birgit Päivänranta, Andreas Langner, Eugenie Kirk, Christian David, and Yasin Ekinci. Sub-10 nm patterning using EUV interference lithography. *Nanotechnology*, 22(37):375302, 9 2011.
- [9] Li Li, Xuan Liu, Shyam Pal, Shulan Wang, Christopher K. Ober, and Emmanuel P. Giannelis. Extreme ultraviolet resist materials for sub-7 nm patterning. *Chemical Society Reviews*, 46(16):4855–4866, 8 2017.
- [10] J M MacLeod and F Rosei. Molecular Self-Assembly on Graphene. *Small*, 10(6):1038–1049, 2014.

- [11] J A Mann and W R Dichtel. Noncovalent Functionalization of Graphene by Molecular and Polymeric Adsorbates. *Journal of Physical Chemistry Letters*, 4(16):2649–2657, 2013.
- [12] L C Giancarlo and G W Flynn. Scanning tunneling and atomic force microscopy probes of self-assembled, physisorbed monolayers: peeking at the peaks. *Annual review of physical chemistry*, 49:297–336, 1 1998.
- [13] Yanhu Wei, Kavita Kannappan, George W Flynn, and Matthew B Zimmt. Scanning Tunneling Microscopy of Prochiral Anthracene Derivatives on Graphite: Chain Length Effects on Monolayer Morphology. *Journal of the American Chemical Society*, 126(16):5318–5322, 2004.
- [14] Y Okawa and M Aono. Linear chain polymerization initiated by a scanning tunneling microscope tip at designated positions. *Journal of Chemical Physics*, 115(5):2317–2322, 2001.
- [15] P C M Grim, S De Feyter, A Gesquiere, P Vanoppen, M Rucker, S Valiyaveetil, G Moessner, K Mullen, and F C De Schryver. Submolecularly resolved polymerization of diacetylene molecules on the graphite surface observed with scanning tunneling microscopy. *Angewandte Chemie-International Edition*, 36(23):2601–2603, 1997.
- [16] M. Akai-Kasaya, K. Shimizu, Y. Watanabe, A. Saito, M. Aono, and Y. Kuwahara. Electronic Structure of a Polydiacetylene Nanowire Fabricated on Highly Ordered Pyrolytic Graphite. *Physical Review Letters*, 91(25):255501, 12 2003.
- [17] Rajiv Giridharagopal and Kevin F Kelly. Substrate-dependent properties of polydiacetylene nanowires on graphite and MoS<sub>2</sub>. *ACS nano*, 2(8):1571–80, 8 2008.
- [18] Dawn A. Bonnell. *Scanning probe microscopy and spectroscopy : theory, techniques, and applications*. Wiley-VCH, 2nd edition, 2000.
- [19] Dawn A Bonnell, D N Basov, Matthias Bode, Ulrike Diebold, Sergei V Kalinin, Vidya Madhavan, Lukas Novotny, Miquel Salmeron, Udo D Schwarz, and Paul S Weiss. Imaging physical phenomena with local probes: From electrons to photons. *Reviews of Modern Physics*, 84(3), 2012.
- [20] Nina Balke, Dawn Bonnell, David S Ginger, and Martijn Kemerink. Scanning probes for new energy materials: Probing local structure and function. *Mrs Bulletin*, 37(7):633–637, 2012.
- [21] Annette F Raigoza, Jason W Dugger, and Lauren J Webb. Review: Recent Advances and Current Challenges in Scanning Probe Microscopy of Biomolecular Surfaces and Interfaces. *ACS Applied Materials & Interfaces*, 5(19):9249–9261, 2013.
- [22] Wilhelm Melitz, Jian Shen, Andrew C Kummel, and Sangyeob Lee. Kelvin probe force microscopy and its application. *Surface Science Reports*, 66(1):1–27, 2011.
- [23] D Anselmetti, R Luthi, E Meyer, T Richmond, M Dreier, J E Frommer, and H J Guntherodt. Attractive-mode imaging of biological materials with dynamic force microscopy. *Nanotechnology*, 5(2):87–94, 4 1994.

- [24] Ricardo García and Alvaro San Paulo. Attractive and repulsive tip-sample interaction regimes in tapping-mode atomic force microscopy. *Physical Review B*, 60(7):4961–4967, 8 1999.
- [25] Mary Luckey. *Membrane structural biology : with biochemical and biophysical foundations*. Cambridge University Press, 2008.
- [26] Swapan K Mandal, Yuji Okawa, Tsuyoshi Hasegawa, and Masakazu Aono. Rate-Determining Factors in the Chain Polymerization of Molecules Initiated by Local Single-Molecule Excitation. *ACS nano*, 5(4):2779–2786, 2011.
- [27] Shawn P. Sullivan, Albert Schnieders, Samuel K. Mbugua, , and Jr\* Thomas P. Beebe. Controlled Polymerization of Substituted Diacetylene Self-Organized Monolayers Confined in Molecule Corrals. 2004.
- [28] Daisuke Takajo, \*, \* Yuji Okawa, Tsuyoshi Hasegawa, , and Masakazu Aono. Chain Polymerization of Diacetylene Compound Multilayer Films on the Top-most Surface Initiated by a Scanning Tunneling Microscope Tip. 2007.
- [29] Younan Xia and George M Whitesides. Soft lithography. *Annual Review of Materials Science*, 28:153–184, 1998.
- [30] Irving Langmuir and Vincent J Schaefer. Activities of urease and pepsin monolayers. *Journal of the American Chemical Society*, 60:1351–1360, 1938.
- [31] Tyson C. Davis, Jae Jin Bang, Jacob T. Brooks, David G. McMillan, and Shelley A. Claridge. Hierarchically Patterned Noncovalent Functionalization of 2D Materials by Controlled LangmuirSchaefer Conversion. *Langmuir*, page acs.langmuir.7b03845, 1 2018.
- [32] A Miura, S De Feyter, M M S Abdel-Mottaleb, A Gesquiere, P C M Grim, G Moessner, M Sieffert, M Klapper, K Mullen, and F C De Schryver. Light- and STM-tip-induced formation of one-dimensional and two-dimensional organic nanostructures. *Langmuir*, 19(16):6474–6482, 2003.
- [33] Rajiv Giridharagopal and Kevin F Kelly. STM-Induced desorption of polydiacetylene nanowires and reordering via molecular cascades. *Journal of Physical Chemistry C*, 111(17):6161–6166, 2007.
- [34] I Doudevski, W A Hayes, and D K Schwartz. Submonolayer island nucleation and growth kinetics during self-assembled monolayer formation. *Physical Review Letters*, 81(22):4927–4930, 1998.
- [35] I Doudevski, W A Hayes, J T Woodward, and D K Schwartz. Atomic force microscope imaging of molecular aggregation during self-assembled monolayer growth. *Colloids and Surfaces, A: Physicochemical and Engineering Aspects*, 174(1-2):233–243, 2000.
- [36] D Lingwood and K Simons. Lipid Rafts As a Membrane-Organizing Principle. *Science*, 327(5961):46–50, 2010.
- [37] Harvey T McMahon and Jennifer L Gallop. Membrane curvature and mechanisms of dynamic cell membrane remodeling. *Nature (London, United Kingdom)*, 438(7068):590–596, 2005.

- [38] E Sezgin, I Levental, S Mayor, and C Eggeling. The mystery of membrane organization: composition, regulation and roles of lipid rafts. *Nature Reviews Molecular Cell Biology*, 18(6):361–374, 2017.
- [39] G Ma and H C Allen. Condensing effect of palmitic acid on DPPC in mixed Langmuir monolayers. *Langmuir*, 23(2):589–597, 2007.
- [40] D Vollhardt. Brewster angle microscopy: A preferential method for mesoscopic characterization of monolayers at the air/water interface. *Current Opinion in Colloid & Interface Science*, 19:183–197, 2014.
- [41] K J Seu, L R Cambrea, R M Everly, and J S Hovis. Influence of lipid chemistry on membrane fluidity: Tail and headgroup interactions. *Biophysical journal*, 91(10):3727–3735, 2006.
- [42] N R Pallas and B A Pethica. Liquid-Expanded to Liquid-Condensed Transitions in Lipid Monolayers at the Air Water Interface. *Langmuir*, 1(4):509–513, 1985.
- [43] R Volinsky, F Gaboriaud, A Berman, and R Jelinek. Morphology and organization of phospholipid/diacetylene Langmuir films studied by Brewster angle microscopy and fluorescence microscopy. *Journal of Physical Chemistry B*, 106(36):9231–9236, 2002.
- [44] Roland Wiesendanger. *Scanning Probe Microscopy and Spectroscopy*. Cambridge University Press, Cambridge, 1994.
- [45] C. Julian. Chen. *Introduction to scanning tunneling microscopy*. Oxford University Press, 1993.
- [46] Chunli. Bai. *Scanning tunneling microscopy and its application*. Springer, 2000.
- [47] G Binnig, H Rohrer, C Gerber, and E Weibel. Tunneling through a Controllable Vacuum Gap. *Applied Physics Letters*, 40(2):178–180, 1982.
- [48] G Binnig and H Rohrer. Scanning tunneling microscopy. *Helvetica Physica Acta*, 55(6):726–735, 1982.
- [49] G Binnig, H Rohrer, C Gerber, and E Weibel. 7X7 Reconstruction on Si(111) resolved in real space. *Physical Review Letters*, 50(2):120–123, 1983.
- [50] Johannes V Barth. Molecular architectonic on metal surfaces. In *Annual Review of Physical Chemistry*, volume 58, pages 375–407. 2007.
- [51] J V Barth, H Brune, G Ertl, and R J Behm. Scanning tunneling microscopy observations on the reconstructed Au(111) surface - atomic structure, long-range superstructure, rotational domains, and surface-defects. *Physical Review B*, 42(15):9307–9318, 1990.
- [52] R M Feenstra. Band-gap of the Ge(111)2 X 1 and Si(111)2 X 1 surfaces by scanning tunneling spectroscopy. *Physical Review B*, 44(24):13791–13794, 1991.
- [53] G Binnig, C F Quate, and C Gerber. Atomic force microscope. *Physical Review Letters*, 56(9):930–933, 1986.

- [54] Shelley A Claridge, Jeffrey J Schwartz, and Paul S Weiss. Electrons, Photons, and Force: Quantitative Single-Molecule Measurements from Physics to Biology. *ACS Nano*, 5(2):693–729, 2011.
- [55] Z J Donhauser, B A Mantooth, K F Kelly, L A Bumm, J D Monnell, J J Stapleton, D W Price, A M Rawlett, D L Allara, J M Tour, and P S Weiss. Conductance switching in single molecules through conformational changes. *Science*, 292(5525):2303–2307, 2001.
- [56] Ajeet S Kumar, Tao Ye, Tomohide Takami, Byung-Chan Yu, Austen K Flatt, James M Tour, and Paul S Weiss. Reversible photo-switching of single azobenzene molecules in controlled nanoscale environments. *Nano Letters*, 8(6):1644–1648, 2008.
- [57] Bala Krishna Pathem, Shelley A Claridge, Yue Bing Zheng, and Paul S Weiss. Molecular Switches and Motors on Surfaces. In M A Johnson and T J Martinez, editors, *Annual Review of Physical Chemistry, Vol 64*, volume 64, pages 605–630. 2013.
- [58] Shelley A Claridge, Wei-Ssu Liao, John C Thomas, Yuxi Zhao, Huan H Cao, Sarawut Cheunkar, Andrew C Serino, Anne M Andrews, and Paul S Weiss. From the bottom up: dimensional control and characterization in molecular monolayers. *Chemical Society Reviews*, 42(7):2725–2745, 2013.
- [59] Nataliya Kalashnyk, Jakob T Nielsen, Erik H Nielsen, Troels Skrydstrup, Daniel E Otzen, Erik Laegsgaard, Chen Wang, Flemming Besenbacher, Niels Chr Nielsen, and Trolle R Linderoth. Scanning Tunneling Microscopy Reveals Single-Molecule Insights into the Self-Assembly of Amyloid Fibrils. *ACS Nano*, 6(8):6882–6889, 2012.
- [60] Annette F Raigoza and Lauren J Webb. Molecularly Resolved Images of Peptide-Functionalized Gold Surfaces by Scanning Tunneling Microscopy. *Journal of the American Chemical Society*, 134(47):19354–19357, 2012.
- [61] Shelley a. Claridge, John C. Thomas, Miles a. Silverman, Jeffrey J. Schwartz, Yanlian Yang, Chen Wang, and Paul S. Weiss. Differentiating amino acid residues and side chain orientations in peptides using scanning tunneling microscopy. *Journal of the American Chemical Society*, 135:18528–18535, 2013.
- [62] Daniel J. Müller, J. Bernard Heymann, Filipp Oesterhelt, Clemens Möller, Hermann Gaub, Georg Büldt, and Andreas Engel. Atomic force microscopy of native purple membrane. *Biochimica et Biophysica Acta (BBA) - Bioenergetics*, 1460(1):27–38, 2000.
- [63] Daniel J Mueller and Andreas Engel. Atomic force microscopy and spectroscopy of native membrane proteins. *Nature Protocols*, 2(9):2191–2197, 2007.
- [64] Andreas Engel and Hermann E Gaub. Structure and mechanics of membrane proteins. In *Annual Review of Biochemistry*, volume 77, pages 127–148. 2008.
- [65] T Ando, N Kodera, E Takai, D Maruyama, K Saito, and A Toda. A high-speed atomic force microscope for studying biological macromolecules. *Proceedings of the National Academy of Sciences of the United States of America*, 98(22):12468–12472, 2001.



- [66] Takayuki Uchihashi, Ryota Iino, Toshio Ando, and Hiroyuki Noji. High-Speed Atomic Force Microscopy Reveals Rotary Catalysis of Rotorless F-1-ATPase. *Science*, 333(6043):755–758, 2011.
- [67] Toshio Ando, Takayuki Uchihashi, and Simon Scheuring. Filming Biomolecular Processes by High-Speed Atomic Force Microscopy. *Chemical Reviews*, 114(6):3120–3188, 2014.
- [68] Benjamin P Brown, Loren Picco, Mervyn J Miles, and Charl F J Faul. Opportunities in High-Speed Atomic Force Microscopy. *Small*, 9(19):3201–3211, 2013.
- [69] Leo Gross, Fabian Mohn, Nikolaj Moll, Peter Liljeroth, and Gerhard Meyer. The chemical structure of a molecule resolved by atomic force microscopy. *Science (New York, N.Y.)*, 325(5944):1110–4, 8 2009.
- [70] Gerhard Meyer, Leo Gross, Fabian Mohn, and Jascha Repp. Scanning Probe Microscopy of Atoms and Molecules on Insulating Films: From Imaging to Molecular Manipulation. *Chimia*, 66(1-2):10–15, 2012.
- [71] A Engel and D J Muller. Observing single biomolecules at work with the atomic force microscope. *Nature Structural Biology*, 7(9):715–718, 2000.
- [72] R M Overney, E Meyer, J Frommer, H J Guntherodt, M Fujihira, H Takano, and Y Gotoh. Force microscopy study of friction and elastic compliance of phase-separated organic thin-films. *Langmuir*, 10(4):1281–1286, 1994.
- [73] J L Wilbur, H A Biebuyck, J C Macdonald, and G M Whitesides. Scanning force microscopies can image patterned self-assembled monolayers. *Langmuir*, 11(3):825–831, 1995.
- [74] Barry C Thompson and Jean M J Frechet. Organic photovoltaics - Polymer-fullerene composite solar cells. *Angewandte Chemie-International Edition*, 47(1):58–77, 2008.
- [75] Ye Huang, Edward J Kramer, Alan J Heeger, and Guillermo C Bazan. Bulk Heterojunction Solar Cells: Morphology and Performance Relationships. *Chemical Reviews*, 114(14):7006–7043, 2014.
- [76] Liam S C Pingree, Obadiah G Reid, and David S Ginger. Electrical Scanning Probe Microscopy on Active Organic Electronic Devices. *Advanced Materials*, 21(1):19–28, 2009.
- [77] D A Bonnell, S V Kalinin, A L Kholkin, and A Gruverman. Piezoresponse Force Microscopy: A Window into Electromechanical Behavior at the Nanoscale. *Mrs Bulletin*, 34(9):648–657, 2009.
- [78] D A Bonnell and S V Kalinin, editors. *Scanning Probe Microscopy for Energy Research*, volume 7. 2013.
- [79] Liam S C Pingree, Bradley A MacLeod, and David S Ginger. The changing face of PEDOT : PSS films: Substrate, bias, and processing effects on vertical charge transport. *Journal of Physical Chemistry C*, 112(21):7922–7927, 2008.

- [80] Liam S C Pingree, Obadiah G Reid, and David S Ginger. Imaging the Evolution of Nanoscale Photocurrent Collection and Transport Networks during Annealing of Polythiophene/Fullerene Solar Cells. *Nano Letters*, 9(8):2946–2952, 2009.
- [81] C Ionescu-Zanetti, A Mechler, S A Carter, and R Lal. Semiconductive polymer blends: Correlating structure with transport properties at the nanoscale. *Advanced Materials*, 16(5):385–+, 2004.
- [82] Y Martin, C C Williams, and H K Wickramasinghe. Atomic force microscope force mapping and profiling on a sub 100-Å scale. *Journal of Applied Physics*, 61(10):4723–4729, 1987.
- [83] V Palermo, M Palma, and P Samori. Electronic characterization of organic thin films by Kelvin probe force microscopy. *Advanced Materials*, 18(2):145–164, 2006.
- [84] T D Krauss and L E Brus. Charge, polarizability, and photoionization of single semiconductor nanocrystals. *Physical Review Letters*, 83(23):4840–4843, 1999.
- [85] T D Krauss, S O’Brien, and L E Brus. Charge and photoionization properties of single semiconductor nanocrystals. *Journal of Physical Chemistry B*, 105(9):1725–1733, 2001.
- [86] Jin Ok Hwang, Duck Hyun Lee, Ju Young Kim, Tae Hee Han, Bong Hoon Kim, Moonkyu Park, Kwangsoo No, and Sang Ouk Kim. Vertical ZnO nanowires/graphene hybrids for transparent and flexible field emission. *Journal of Materials Chemistry*, 21(10):3432–3437, 2011.
- [87] Andres Castellanos-Gomez, Emmanuele Cappelluti, Rafael Roldan, Nicolas Agrait, Francisco Guinea, and Gabino Rubio-Bollinger. Electric-Field Screening in Atomically Thin Layers of MoS<sub>2</sub>: the Role of Interlayer Coupling. *Advanced Materials*, 25(6):899–903, 2013.
- [88] Evan J Spadafora, Renaud Demadrille, Bernard Ratier, and Benjamin Grevin. Imaging the Carrier Photogeneration in Nanoscale Phase Segregated Organic Heterojunctions by Kelvin Probe Force Microscopy. *Nano Letters*, 10(9):3337–3342, 2010.
- [89] Sahwan Hong, Taekjib Choi, Ji Hoon Jeon, Yunseok Kim, Hosang Lee, Ho-Young Joo, Inrok Hwang, Jin-Soo Kim, Sung-Oong Kang, Sergei V Kalinin, and Bae Ho Park. Large Resistive Switching in Ferroelectric BiFeO<sub>3</sub> Nano-Island Based Switchable Diodes. *Advanced Materials*, 25(16):2339–2343, 2013.
- [90] L Burgi, H Sirringhaus, and R H Friend. Noncontact potentiometry of polymer field-effect transistors. *Applied Physics Letters*, 80(16):2913–2915, 2002.
- [91] L Burgi, T J Richards, R H Friend, and H Sirringhaus. Close look at charge carrier injection in polymer field-effect transistors. *Journal of Applied Physics*, 94(9):6129–6137, 2003.
- [92] David C Coffey, Obadiah G Reid, Deanna B Rodovsky, Glenn P Bartholomew, and David S Ginger. Mapping local photocurrents in polymer/fullerene solar cells with photoconductive atomic force microscopy. *Nano Letters*, 7(3):738–744, 2007.

- [93] I Lee, J W Lee, A Stubna, and E Greenbaum. Measurement of electrostatic potentials above oriented single photosynthetic reaction centers. *Journal of Physical Chemistry B*, 104(11):2439–2443, 2000.
- [94] C C Williams, J Slinkman, W P Hough, and H K Wickramasinghe. Lateral dopant profiling with 200 nm resolution by scanning capacitance microscopy. *Applied Physics Letters*, 55(16):1662–1664, 1989.
- [95] J R Matey and J Blanc. Scanning capacitance microscopy. *Journal of Applied Physics*, 57(5):1437–1444, 1985.
- [96] C C Williams, W P Hough, and S A Rishton. Scanning capacitance microscopy on a 25 nm scale. *Applied Physics Letters*, 55(2):203–205, 1989.
- [97] C C Williams. Two-dimensional dopant profiling by scanning capacitance microscopy. *Annual Review of Materials Science*, 29:471–504, 1999.
- [98] Kendra Kathan-Galipeau, Sanjini Nanayakkara, Paul A O’Brian, Maxim Niki-forov, Bohdana M Discher, and Dawn A Bonnell. Direct Probe of Molecular Polarization in De Novo Protein-Electrode Interfaces. *ACS Nano*, 5(6):4835–4842, 2011.
- [99] Anthony R. West. *Solid state chemistry and its applications*. Wiley, 1984.
- [100] Eiji. Nakamura, M. Adachi, Y. Akishige, K. Deguchi, J. Harada, T. Ikeda, M. Okuyama, E. Sawaguchi, Y. Shiozaki, K. Toyoda, T. Yamada, K. Gesi, T. Hikita, Y. Makita, T. Shigenari, I. Tatsuzaki, and T. Yagi. *Landolt-Bornstein Zahlenwerte und Funktionen aus Naturwissenschaften und Technik: Neue Serie, Subvolume: Oxides*. Springer, 1990.
- [101] E Fukada and I Yasuda. On the piezoelectric effect of bone. *Journal of the Physical Society of Japan*, 12(10):1158–1162, 1957.
- [102] C Halperin, S Mutchnik, A Agronin, M Molotskii, P Urenski, M Salai, and G Rosenman. Piezoelectric effect in human bones studied in nanometer scale. *Nano Letters*, 4(7):1253–1256, 2004.
- [103] S V Kalinin and D A Bonnell. Imaging mechanism of piezoresponse force microscopy of ferroelectric surfaces. *Physical Review B*, 65(12), 2002.
- [104] S Jesse, A P Baddorf, and S V Kalinin. Dynamic behaviour in piezoresponse force microscopy. *Nanotechnology*, 17(6):1615–1628, 2006.
- [105] Stephen Jesse, Brian J Rodriguez, Samrat Choudhury, Arthur P Baddorf, Ionela Vrejoiu, Dietrich Hesse, Marin Alexe, Eugene A Eliseev, Anna N Morozovska, Jingxian Zhang, Long-Qing Chen, and Sergei V Kalinin. Direct imaging of the spatial and energy distribution of nucleation centres in ferroelectric materials. *Nature Materials*, 7(3):209–215, 2008.
- [106] N Balke, S Jesse, A N Morozovska, E Eliseev, D W Chung, Y Kim, L Adamczyk, R E Garcia, N Dudney, and S V Kalinin. Nanoscale mapping of ion diffusion in a lithium-ion battery cathode. *Nat Nanotechnol*, 5(10):749–754, 2010.

- [107] S V Kalinin, B J Rodriguez, J Shin, S Jesse, V Grichko, T Thundat, A P Baddorf, and A Gruverman. Bioelectromechanical imaging by scanning probe microscopy: Galvani's experiment at the nanoscale. *Ultramicroscopy*, 106(4-5):334–340, 2006.
- [108] Sergei V Kalinin, Brian J Rodriguez, Stephen Jesse, Edgar Karapetian, Boris Mirman, Eugene A Eliseev, and Anna N Morozovska. Nanoscale electromechanics of ferroelectric and biological systems: A new dimension in scanning probe microscopy. In *Annual Review of Materials Research*, volume 37, pages 189–238. 2007.
- [109] S V Kalinin, B J Rodriguez, S Jesse, T Thundat, and A Gruverman. Electromechanical imaging of biological systems with sub-10 nm resolution. *Applied Physics Letters*, 87(5), 2005.
- [110] Shigeru Amemiya, Allen J Bard, Fu-Ren F Fan, Michael V Mirkin, and Patrick R Unwin. Scanning Electrochemical Microscopy. In *Annual Review of Analytical Chemistry*, volume 1, pages 95–131. 2008.
- [111] A J Bard, F R F Fan, J Kwak, and O Lev. Scanning electrochemical microscopy - Introduction and principles. *Analytical Chemistry*, 61(2):132–138, 1989.
- [112] M V Mirkin and B R Horrocks. Electroanalytical measurements using the scanning electrochemical microscope. *Analytica Chimica Acta*, 406(2):119–146, 2000.
- [113] J V Macpherson and P R Unwin. Combined scanning electrochemical-atomic force microscopy. *Analytical Chemistry*, 72(2):276–285, 2000.
- [114] Michael V. Mirkin and Shigeru. Amemiya. *Nanoelectrochemistry*. CRC Press, 2017.
- [115] C Kranz, G Friedbacher, and B Mizaikoff. Integrating an ultramicroelectrode in an AFM cantilever: Combined technology for enhanced information. *Analytical Chemistry*, 73(11):2491–+, 2001.
- [116] A Kueng, C Kranz, A Lugstein, E Bertagnolli, and B Mizaikoff. Integrated AFM-SECM in tapping mode: Simultaneous topographical and electrochemical imaging of enzyme activity. *Angewandte Chemie-International Edition*, 42(28):3238–3240, 2003.
- [117] J V Macpherson and P R Unwin. Noncontact electrochemical imaging with combined scanning electrochemical atomic force microscopy. *Analytical Chemistry*, 73(3):550–557, 2001.
- [118] Maksymilian A Derylo, Kirstin C Morton, and Lane A Baker. Parylene Insulated Probes for Scanning Electrochemical-Atomic Force Microscopy. *Langmuir*, 27(22):13925–13930, 2011.
- [119] A Davoodi, J Pan, C Leygraf, and S Norgren. The role of intermetallic particles in localized corrosion of an aluminum alloy studied by SKPFM and integrated AFM/SECM. *Journal of the Electrochemical Society*, 155(5):C211–C218, 2008.
- [120] B Cappella and G Dietler. Force-distance curves by atomic force microscopy. *Surface Science Reports*, 34(1-3):1–+, 1999.

- [121] Hans-Jrgen Butt, Brunero Cappella, and Michael Kappl. Force measurements with the atomic force microscope: Technique, interpretation and applications. *Surface Science Reports*, 59(1-6):1–152, 10 2005.
- [122] M Rief, H Clausen-Schaumann, and H E Gaub. Sequence-dependent mechanics of single DNA molecules. *Nature Structural Biology*, 6(4):346–349, 1999.
- [123] H Schonherr and G J Vancso. *Scanning Force Microscopy of Polymers*. 2010.
- [124] M R VanLandingham, J S Villarrubia, W F Guthrie, and G F Meyers. Nanoin-dentation of polymers: An overview. *Macromolecular Symposia*, 167:15–43, 2001.
- [125] M R VanLandingham. Review of instrumented indentation. *Journal of Research of the National Institute of Standards and Technology*, 108(4):249–265, 2003.
- [126] M Stolz, R Raiteri, A U Daniels, M R VanLandingham, W Baschong, and U Aebi. Dynamic elastic modulus of porcine articular cartilage determined at two different levels of tissue organization by indentation-type atomic force microscopy. *Biophysical Journal*, 86(5):3269–3283, 2004.
- [127] M Rief, M Gautel, F Oesterhelt, J M Fernandez, and H E Gaub. Reversible unfolding of individual titin immunoglobulin domains by AFM. *Science*, 276(5315):1109–1112, 1997.
- [128] M Grandbois, M Beyer, M Rief, H Clausen-Schaumann, and H E Gaub. How strong is a covalent bond? *Science*, 283(5408):1727–1730, 1999.
- [129] A Ebner, F Kienberger, G Kada, C M Stroh, M Geretschlager, A S M Kamruz-zahan, L Wildling, W T Johnson, B Ashcroft, J Nelson, S M Lindsay, H J Gruber, and P Hinterdorfer. Localization of single avidin-biotin interactions using simultaneous topography and molecular recognition imaging. *Chemphyschem*, 6(5):897–900, 2005.
- [130] P Hinterdorfer, W Baumgartner, H J Gruber, K Schilcher, and H Schindler. Detection and localization of individual antibody-antigen recognition events by atomic force microscopy. *Proceedings of the National Academy of Sciences of the United States of America*, 93(8):3477–3481, 1996.
- [131] G J Schutz, M Sonnleitner, P Hinterdorfer, and H Schindler. Single molecule microscopy of biomembranes (review). *Molecular Membrane Biology*, 17(1):17–29, 2000.
- [132] F Kienberger, A Ebner, H J Gruber, and P Hinterdorfer. Molecular recognition imaging and force spectroscopy of single biomolecules. *Accounts of Chemical Research*, 39(1):29–36, 2006.
- [133] Daniel J Mueller, Jonne Helenius, David Alsteens, and Yves F Dufrene. Force probing surfaces of living cells to molecular resolution. *Nature Chemical Biology*, 5(6):383–390, 2009.
- [134] E. L. Florin, V. T. Moy, and H. E. Gaub. Adhesion forces between individual ligand-receptor pairs. *Science*, 264(5157):415–417, 1994.

- [135] Gil U. Lee, Linda A. Chrisey, and Richard J. Colton. Direct measurement of the forces between complementary strands of DNA. *Science*, 266(5186):771–773, 1994.
- [136] Sabyasachi Rakshit, Yunxiang Zhang, Kristine Manibog, Omer Shafraz, and Sanjeevi Sivasankar. Ideal, catch, and slip bonds in cadherin adhesion. *Proceedings of the National Academy of Sciences of the United States of America*, 109(46):18815–18820, 2012.
- [137] Peter Hinterdorfer and Yves F Dufrêne. Detection and localization of single molecular recognition events using atomic force microscopy. *Nature methods*, 3(5):347–55, 5 2006.
- [138] Arvind Raman, John Melcher, and Ryan Tung. Cantilever dynamics in atomic force microscopy. *Nano Today*, 3(1-2):20–27, 2008.
- [139] Ricardo Garcia and Elena T Herruzo. The emergence of multifrequency force microscopy. *Nature nanotechnology*, 7(4):217–26, 4 2012.
- [140] Shuai Zhang, Husnu Aslan, Flemming Besenbacher, and Mingdong Dong. Quantitative biomolecular imaging by dynamic nanomechanical mapping. *Chemical Society Reviews*, 43(21):7412–7429, 2014.
- [141] Elena T Herruzo, Alma P Perrino, and Ricardo Garcia. Fast nanomechanical spectroscopy of soft matter. *Nat Commun*, 5, 2014.
- [142] M Penedo, A Raman, S Hormeno, I Fernandez-Martinez, M Luna, and F Briones. Enhanced efficiency in the excitation of higher modes for atomic force microscopy and mechanical sensors operated in liquids. *Applied Physics Letters*, 105(17), 2014.
- [143] Robert D Turner, Jennifer Kirkham, Deirdre Devine, and Neil H Thomson. Second harmonic atomic force microscopy of living *Staphylococcus aureus* bacteria. *Applied Physics Letters*, 94(4), 2009.
- [144] A Raman, S Trigueros, A Cartagena, A P Z Stevenson, M Susilo, E Nauman, and S Antoranz Contera. Mapping nanomechanical properties of live cells using multi-harmonic atomic force microscopy. *Nature nanotechnology*, 6(12):809–14, 12 2011.
- [145] Ricardo Garcia and Roger Proksch. Nanomechanical mapping of soft matter by bimodal force microscopy. *European Polymer Journal*, 49(8):1897–1906, 2013.
- [146] Christian Dietz, Elena T Herruzo, Jose R Lozano, and Ricardo Garcia. Nanomechanical coupling enables detection and imaging of 5 nm superparamagnetic particles in liquid. *Nanotechnology*, 22(12), 2011.
- [147] D. Martinez-Martin, E. T. Herruzo, C. Dietz, J. Gomez-Herrero, and R. Garcia. Noninvasive Protein Structural Flexibility Mapping by Bimodal Dynamic Force Microscopy. *Physical Review Letters*, 106(19):198101, 5 2011.
- [148] Daniel Platz, Erik A Tholen, Devrim Pesen, and David B Haviland. Intermodulation atomic force microscopy. *Applied Physics Letters*, 92(15), 2008.

- [149] Carsten Hutter, Daniel Platz, E A Tholen, T H Hansson, and D B Haviland. Reconstructing Nonlinearities with Intermodulation Spectroscopy. *Physical Review Letters*, 104(5), 2010.
- [150] Brian J Rodriguez, Clint Callahan, Sergei V Kalinin, and Roger Proksch. Dual-frequency resonance-tracking atomic force microscopy. *Nanotechnology*, 18(47), 2007.
- [151] S Jesse, R K Vasudevan, L Collins, E Strelcov, M B Okatan, A Belianinov, A P Baddorf, R Proksch, and S V Kalinin. Band Excitation in Scanning Probe Microscopy: Recognition and Functional Imaging. In M A Johnson and T J Martinez, editors, *Annual Review of Physical Chemistry, Vol 65*, volume 65, pages 519–536. 2014.
- [152] Hendrik Dietz, Felix Berkemeier, Morten Bertz, and Matthias Rief. Anisotropic deformation response of single protein molecules. *Proceedings of the National Academy of Sciences of the United States of America*, 103(34):12724–12728, 2006.
- [153] Laurene Tetard, Ali Passian, Rachel M Lynch, Brynn H Voy, Gajendra Shekhawat, Vinayak Dravid, and Thomas Thundat. Elastic phase response of silica nanoparticles buried in soft matter. *Applied Physics Letters*, 93(13), 2008.
- [154] Sudhir Husale, Henrik H J Persson, and Ozgur Sahin. DNA nanomechanics allows direct digital detection of complementary DNA and microRNA targets. *Nature*, 462(7276):1075–U138, 2009.
- [155] Mingdong Dong, Sudhir Husale, and Ozgur Sahin. Determination of protein structural flexibility by microsecond force spectroscopy. *Nat Nanotechnol*, 4(8):514–517, 2009.
- [156] L Tetard, A Passian, and T Thundat. New modes for subsurface atomic force microscopy through nanomechanical coupling. *Nat Nanotechnol*, 5(2):105–109, 2010.
- [157] G S Shekhawat and V P Dravid. Nanoscale imaging of buried structures via scanning near-field ultrasound holography. *Science*, 310(5745):89–92, 2005.
- [158] Laurene Tetard, Ali Passian, Katherine T Venmar, Rachel M Lynch, Brynn H Voy, Gajendra Shekhawat, Vinayak P Dravid, and Thomas Thundat. Imaging nanoparticles in cells by nanomechanical holography. *Nat Nanotechnol*, 3(8):501–505, 2008.
- [159] A Dazzi, R Prazeres, E Glotin, and J M Ortega. Local infrared microspectroscopy with subwavelength spatial resolution with an atomic force microscope tip used as a photothermal sensor. *Optics Letters*, 30(18):2388–2390, 2005.
- [160] Alexandre Dazzi, Craig B Prater, Qichi Hu, D Bruce Chase, John F Rabolt, and Curtis Marcott. AFM-IR: Combining Atomic Force Microscopy and Infrared Spectroscopy for Nanoscale Chemical Characterization. *Applied Spectroscopy*, 66(12):1365–1384, 2012.
- [161] Matthew D Sonntag, Eric A Pozzi, Nan Jiang, Mark C Hersam, and Richard P Van Duyne. Recent Advances in Tip-Enhanced Raman Spectroscopy. 2014.

- [162] Zachary D Schultz, James M Marr, and Hao Wang. Tip enhanced Raman scattering: plasmonic enhancements for nanoscale chemical analysis. *Nanophotonics*, 3(1-2):91–104, 2014.
- [163] Liying Jiao, Li Zhang, Xinran Wang, Georgi Diankov, and Hongjie Dai. Narrow graphene nanoribbons from carbon nanotubes. *Nature*, 458(7240):877–880, 2009.
- [164] Hans A Bechtel, Eric A Muller, Robert L Olmon, Michael C Martin, and Markus B Raschke. Ultrabroadband infrared nanospectroscopic imaging. *Proceedings of the National Academy of Sciences of the United States of America*, 111(20):7191–7196, 2014.
- [165] Olga S Ovchinnikova, Kevin Kjoller, Gregory B Hurst, Dale A Pelletier, and Gary J Van Berkel. Atomic Force Microscope Controlled Topographical Imaging and Proximal Probe Thermal Desorption/Ionization Mass Spectrometry Imaging. *Analytical Chemistry*, 86(2):1083–1090, 2014.
- [166] V F Puentes, P Gorostiza, D M Aruguete, N G Bastus, and A P Alivisatos. Collective behaviour in two-dimensional cobalt nanoparticle assemblies observed by magnetic force microscopy. *Nature Materials*, 3(4):263–268, 2004.
- [167] N Anderson, A Hartschuh, S Cronin, and L Novotny. Nanoscale vibrational analysis of single-walled carbon nanotubes. *Journal of the American Chemical Society*, 127(8):2533–2537, 2005.
- [168] Neil Anderson, Achim Hartschuh, and Lukas Novotny. Chirality changes in carbon nanotubes studied with near-field Raman spectroscopy. *Nano Letters*, 7(3):577–582, 2007.
- [169] J N Chen, M Badioli, P Alonso-Gonzalez, S Thongrattanasiri, F Huth, J Osmond, M Spasenovic, A Centeno, A Pesquera, P Godignon, A Z Elorza, N Camara, F J G de Abajo, R Hillenbrand, and F H L Koppens. Optical nano-imaging of gate-tunable graphene plasmons. *Nature*, 487(7405):77–81, 2012.
- [170] Y Martin and H K Wickramasinghe. Magnetic imaging by force microscopy with 1000-Å resolution. *Applied Physics Letters*, 50(20):1455–1457, 1987.
- [171] G A Medvedkin, T Ishibashi, T Nishi, K Hayata, Y Hasegawa, and K Sato. Room temperature ferromagnetism in novel diluted magnetic semiconductor Cd<sub>1-x</sub>MnxGeP<sub>2</sub>. *Japanese Journal of Applied Physics Part 2-Letters*, 39(10A):L949–L951, 2000.
- [172] D Rugar, C S Yannoni, and J A Sidles. Mechanical detection of magnetic-resonance. *Nature*, 360(6404):563–566, 1992.
- [173] D Rugar, R Budakian, H J Mamin, and B W Chui. Single spin detection by magnetic resonance force microscopy. *Nature*, 430(6997):329–332, 2004.
- [174] H J Mamin, M Poggio, C L Degen, and D Rugar. Nuclear magnetic resonance imaging with 90-nm resolution. *Nat Nanotechnol*, 2(5):301–306, 2007.
- [175] C L Degen, M Poggio, H J Mamin, C T Rettner, and D Rugar. Nanoscale magnetic resonance imaging. *Proceedings of the National Academy of Sciences of the United States of America*, 106(5):1313–1317, 2009.



- [176] W P King, T W Kenny, K E Goodson, G Cross, M Despont, U Durig, H Rothuizen, G K Binnig, and P Vettiger. Atomic force microscope cantilevers for combined thermomechanical data writing and reading. *Applied Physics Letters*, 78(9):1300–1302, 2001.
- [177] B A Nelson and W P King. Measuring material softening with nanoscale spatial resolution using heated silicon probes. *Review of Scientific Instruments*, 78(2), 2007.
- [178] Kyle L Grosse, Myung-Ho Bae, Feifei Lian, Eric Pop, and William P King. Nanoscale Joule heating, Peltier cooling and current crowding at graphene-metal contacts. *Nat Nanotechnol*, 6(5):287–290, 2011.
- [179] Kyle L Grosse, Vincent E Dorgan, David Estrada, Joshua D Wood, Ivan Vlassiouk, Gyula Eres, Joseph W Lyding, William P King, and Eric Pop. Direct observation of resistive heating at graphene wrinkles and grain boundaries. *Applied Physics Letters*, 105(14), 2014.
- [180] Kyle L Grosse, Eric Pop, and William P King. Nanometer-scale temperature imaging for independent observation of Joule and Peltier effects in phase change memory devices. *Review of Scientific Instruments*, 85(9), 2014.
- [181] Olga S Ovchinnikova, Maxim P Nikiforov, James A Bradshaw, Stephen Jesse, and Gary J Van Berkel. Combined Atomic Force Microscope-Based Topographical Imaging and Nanometer-Scale Resolved Proximal Probe Thermal Desorption/Electrospray Ionization-Mass Spectrometry. *ACS Nano*, 5(7):5526–5531, 2011.
- [182] Matthias Lorenz, Olga S Ovchinnikova, Vilmos Kertesz, and Gary J Van Berkel. Controlled-Resonant Surface Tapping-Mode Scanning Probe Electrospray Ionization Mass Spectrometry Imaging. *Analytical Chemistry*, 86(6):3146–3152, 2014.
- [183] Yves Fleming, Tom Wirtz, Urs Gysin, Thilo Glatzel, Urs Wegmann, Ernst Meyer, Urs Maier, and Joerg Rychen. Three dimensional imaging using secondary ion mass spectrometry and atomic force microscopy. *Applied Surface Science*, 258(4):1322–1327, 2011.
- [184] Tom Wirtz, Yves Fleming, Urs Gysin, Thilo Glatzel, Urs Wegmann, Ernst Meyer, Urs Maier, and Joerg Rychen. Combined SIMS-SPM instrument for high sensitivity and high-resolution elemental 3D analysis. *Surface and Interface Analysis*, 45(1):513–516, 2013.
- [185] Tom Wirtz, Yves Fleming, Mathieu Gerard, Urs Gysin, Thilo Glatzel, Ernst Meyer, Urs Wegmann, Urs Maier, Aitziber Herrero Odriozola, and Daniel Uehli. Design and performance of a combined secondary ion mass spectrometry-scanning probe microscopy instrument for high sensitivity and high-resolution elemental three-dimensional analysis. *Review of Scientific Instruments*, 83(6), 2012.
- [186] A M Moore, S Yeganeh, Y X Yao, S A Claridge, J M Tour, M A Ratner, and P S Weiss. Polarizabilities of Adsorbed and Assembled Molecules: Measuring the Conductance through Buried Contacts. *ACS nano*, 4(12):7630–7636, 2010.

- [187] Jascha Repp, Gerhard Meyer, Sladjana M. Stojković, Andr Gourdon, and Christian Joachim. Molecules on Insulating Films: Scanning-Tunneling Microscopy Imaging of Individual Molecular Orbitals. *Physical Review Letters*, 94(2):026803, 1 2005.
- [188] Chi-lun Chiang, Chen Xu, Zhumin Han, and W Ho. Real-space imaging of molecular structure and chemical bonding by single-molecule inelastic tunneling probe. *Science (New York, N.Y.)*, 344(6186):885–8, 5 2014.
- [189] A M Moore and P S Weiss. Functional and Spectroscopic Measurements with Scanning Tunneling Microscopy. *Annual Review of Analytical Chemistry*, 1:857–882, 2008.
- [190] H J W Zandvliet and A van Houselt. Scanning Tunneling Spectroscopy. *Annual Review of Analytical Chemistry*, 2:37–55, 2009.
- [191] M H Hamidian, A R Schmidt, I A Firmo, M P Allan, P Bradley, J D Garrett, T J Williams, G M Luke, Y Dubi, A V Balatsky, and J C Davis. How Kondo-holes create intense nanoscale heavy-fermion hybridization disorder. *Proceedings of the National Academy of Sciences of the United States of America*, 108(45):18233–18237, 2011.
- [192] A R Schmidt, M H Hamidian, P Wahl, F Meier, A V Balatsky, J D Garrett, T J Williams, G M Luke, and J C Davis. Imaging the Fano lattice to ‘hidden order’ transition in URu<sub>2</sub>Si<sub>2</sub>. *Nature*, 465(7298):570–576, 2010.
- [193] M Akai-Kasaya, K Shimizu, Y Watanabe, A Saito, M Aono, and Y Kuwahara. Electronic structure of a polydiacetylene nanowire fabricated on highly ordered pyrolytic graphite. *Physical Review Letters*, 91(25):4, 2003.
- [194] S Folsch, P Hyldgaard, R Koch, and K H Ploog. Quantum confinement in monatomic Cu chains on Cu(111). *Physical Review Letters*, 92(5):4, 2004.
- [195] O Wolf, M Dasog, Z Yang, I Balberg, J G C Veinot, and O Millo. Doping and Quantum Confinement Effects in Single Si Nanocrystals Observed by Scanning Tunneling Spectroscopy. *Nano Letters*, 13(6):2516–2521, 2013.
- [196] Young Jae Song, Kyuho Lee, Seong Heon Kim, Byoung-Young Choi, Jaejun Yu, and Young Kuk. Mapping atomic contact between pentacene and a Au surface using scanning tunneling spectroscopy. *Nano letters*, 10(3):996–9, 3 2010.
- [197] S Chi, S Grothe, R X Liang, P Dosanjh, W N Hardy, S A Burke, D A Bonn, and Y Pennec. Scanning Tunneling Spectroscopy of Superconducting LiFeAs Single Crystals: Evidence for Two Nodeless Energy Gaps and Coupling to a Bosonic Mode. *Physical Review Letters*, 109(8):5, 2012.
- [198] R Decker, Y Wang, V W Brar, W Regan, H Z Tsai, Q Wu, W Gannett, A Zettl, and M F Crommie. Local Electronic Properties of Graphene on a BN Substrate via Scanning Tunneling Microscopy. *Nano Letters*, 11(6):2291–2295, 2011.
- [199] P Liljeroth, J Repp, and G Meyer. Current-induced hydrogen tautomerization and conductance switching of naphthalocyanine molecules. *Science*, 317(5842):1203–1206, 2007.

- [200] R C Jaklevic and J Lambe. Molecular Vibration Spectra by Electron Tunneling. *Physical Review Letters*, 17(22):1139–&, 1966.
- [201] W Ho. Single-molecule chemistry. *Journal of Chemical Physics*, 117(24):11033–11061, 2002.
- [202] P K Hansma. Inelastic electron-tunneling. *Physics Reports-Review Section of Physics Letters*, 30(2):145–206, 1977.
- [203] J R Hahn and W Ho. Vibrational mode specific bond dissociation in a single molecule. *Journal of Chemical Physics*, 131(4):4, 2009.
- [204] J I Pascual, J J Jackiw, Z Song, P S Weiss, H Conrad, and H P Rust. Adsorbate-substrate vibrational modes of benzene on Ag(110) resolved with scanning tunneling spectroscopy. *Physical Review Letters*, 86(6):1050–1053, 2001.
- [205] M Lackinger, M S Janson, and W Ho. Localized interaction of single porphyrin molecules with oxygen vacancies on TiO<sub>2</sub>(110). *Journal of Chemical Physics*, 137(23):7, 2012.
- [206] M M Blake, S U Nanayakkara, S A Claridge, L C Fernandez-Torres, E C H Sykes, and P S Weiss. Identifying Reactive Intermediates in the Ullmann Coupling Reaction by Scanning Tunneling Microscopy and Spectroscopy. *Journal of Physical Chemistry A*, 113(47):13167–13172, 2009.
- [207] Byoung-Young Choi, Se-Jong Kahng, Seungchul Kim, Hajin Kim, Hyo Kim, Young Song, Jisoon Ihm, and Young Kuk. Conformational Molecular Switch of the Azobenzene Molecule: A Scanning Tunneling Microscopy Study. *Physical Review Letters*, 96(15):156106, 4 2006.
- [208] T Komeda. Chemical identification and manipulation of molecules by vibrational excitation via inelastic tunneling process with scanning tunneling microscopy. *Progress in Surface Science*, 78(2):41–85, 2005.
- [209] Manfred Parschau, Karl-Heinz Rieder, Hans J Hug, and Karl-Heinz Ernst. Single-molecule chemistry and analysis: mode-specific dehydrogenation of adsorbed propene by inelastic electron tunneling. *Journal of the American Chemical Society*, 133(15):5689–91, 4 2011.
- [210] Y Sainoo, Y Kim, T Komeda, M Kawai, and H Shigekawa. Observation of cis-2-butene molecule on Pd(110) by cryogenic STM: site determination using tunneling-current-induced rotation. *Surface Science*, 536(1-3):L403–L407, 2003.
- [211] K Motobayashi, Y Kim, R Arafune, M Ohara, H Ueba, and M Kawai. Dissociation pathways of a single dimethyl disulfide on Cu(111): Reaction induced by simultaneous excitation of two vibrational modes. *Journal of Chemical Physics*, 140(19):8, 2014.
- [212] B C Stipe, M A Rezaei, and W Ho. Single-molecule vibrational spectroscopy and microscopy. *Science*, 280(5370):1732–1735, 1998.
- [213] N Lorente, M Persson, L J Lauhon, and W Ho. Symmetry selection rules for vibrationally inelastic tunneling. *Physical Review Letters*, 86(12):2593–2596, 2001.

- [214] Q Huan, Y Jiang, Y Y Zhang, U Ham, and W Ho. Spatial imaging of individual vibronic states in the interior of single molecules. *Journal of Chemical Physics*, 135(1):6, 2011.
- [215] A S Hallback, N Oncel, J Huskens, H J W Zandvliet, and B Poelsema. Inelastic electron tunneling spectroscopy on decanethiol at elevated temperatures. *Nano Letters*, 4(12):2393–2395, 2004.
- [216] Rajiv Giridharagopal, Jun Zhang, and Kevin F Kelly. Antenna-based ultrahigh vacuum microwave frequency scanning tunneling microscopy system. *Review of Scientific Instruments*, 82(5), 2011.
- [217] J Lee, X W Tu, and W Ho. Spectroscopy and microscopy of spin-sensitive rectification current induced by microwave radiation. *Nano Letters*, 5(12):2613–2617, 2005.
- [218] J H Worne, R Giridharagopal, K F Kelly, and D Natelson. Interfacial Charge Transfer in Nanoscale Polymer Transistors. *Nano Research*, 1(4):341–350, 2008.
- [219] A Hazarika, E Peretz, V Dikovsky, P K Santra, R Z Shneck, D D Sarma, and Y Manassen. STM verification of the reduction of the Young’s modulus of CdS nanoparticles at smaller sizes. *Surface Science*, 630:89–95, 2014.
- [220] N Agrait, A L Yeyati, and J M van Ruitenbeek. Quantum properties of atomic-sized conductors. *Physics Reports-Review Section of Physics Letters*, 377(2-3):81–279, 2003.
- [221] S J van der Molen and P Liljeroth. Charge transport through molecular switches. *Journal of Physics: Condensed Matter*, 22(13):30, 2010.
- [222] F Chen and N J Tao. Electron Transport in Single Molecules: From Benzene to Graphene. *Accounts of Chemical Research*, 42(3):429–438, 2009.
- [223] X L Li, B Q Xu, X Y Xiao, X M Yang, L Zang, and N J Tao. Controlling charge transport in single molecules using electrochemical gate. *Faraday Discussions*, 131:111–120, 2006.
- [224] M Brandbyge, J Schiøtz, M R Sørensen, P Stoltze, K W Jacobsen, J K Nørskov, L Olesen, E Laegsgaard, I Stensgaard, and F Besenbacher. Quantized Conductance in Atom-Sized Wires Between Two Metals. *Physical Review B*, 52(11):8499–8514, 1995.
- [225] B Q Xu and N J J Tao. Measurement of single-molecule resistance by repeated formation of molecular junctions. *Science*, 301(5637):1221–1223, 2003.
- [226] F Chen, X L Li, J Hihath, Z F Huang, and N J Tao. Effect of anchoring groups on single-molecule conductance: Comparative study of thiol-, amine-, and carboxylic-acid-terminated molecules. *Journal of the American Chemical Society*, 128(49):15874–15881, 2006.
- [227] M Kamenetska, M Koentopp, A C Whalley, Y S Park, M L Steigerwald, C Nuckolls, M S Hybertsen, and L Venkataraman. Formation and Evolution of Single-Molecule Junctions. *Physical Review Letters*, 102(12), 2009.

- [228] X Y Xiao, B Q Xu, and N J Tao. Measurement of single molecule conductance: Benzenedithiol and benzenedimethanethiol. *Nano Letters*, 4(2):267–271, 2004.
- [229] S Loth, M Etzkorn, C P Lutz, D M Eigler, and A J Heinrich. Measurement of Fast Electron Spin Relaxation Times with Atomic Resolution. *Science*, 329(5999):1628–1630, 2010.
- [230] A A Khajetoorians, B Baxevanis, C Hubner, T Schlenk, S Krause, T O Wehling, S Lounis, A Lichtenstein, D Pfannkuche, J Wiebe, and R Wiesendanger. Current-Driven Spin Dynamics of Artificially Constructed Quantum Magnets. *Science*, 339(6115):55–59, 2013.
- [231] N Atodiresei, J Brede, P Lazic, V Caciuc, G Hoffmann, R Wiesendanger, and S Blugel. Design of the Local Spin Polarization at the Organic-Ferromagnetic Interface. *Physical Review Letters*, 105(6):4, 2010.
- [232] J E Bickel, F Meier, J Brede, A Kubetzka, K von Bergmann, and R Wiesendanger. Magnetic properties of monolayer Co islands on Ir(111) probed by spin-resolved scanning tunneling microscopy. *Physical Review B*, 84(5):6, 2011.
- [233] J Brede, N Atodiresei, S Kuck, P Lazic, V Caciuc, Y Morikawa, G Hoffmann, S Blugel, and R Wiesendanger. Spin- and Energy-Dependent Tunneling through a Single Molecule with Intramolecular Spatial Resolution. *Physical Review Letters*, 105(4):4, 2010.
- [234] S Krause, L Berbil-Bautista, G Herzog, M Bode, and R Wiesendanger. Current-induced magnetization switching with a spin-polarized scanning tunneling microscope. *Science*, 317(5844):1537–1540, 2007.
- [235] A J Heinrich, J A Gupta, C P Lutz, and D M Eigler. Single-atom spin-flip spectroscopy. *Science*, 306(5695):466–469, 2004.
- [236] C F Hirjibehedin, C P Lutz, and A J Heinrich. Spin coupling in engineered atomic structures. *Science*, 312(5776):1021–1024, 2006.
- [237] Y J Song, A F Otte, V Shvarts, Z Y Zhao, Y Kuk, S R Blankenship, A Band, F M Hess, and J A Stroscio. Invited Review Article: A 10 mK scanning probe microscopy facility. *Review of Scientific Instruments*, 81(12):33, 2010.
- [238] T Zhang, N Levy, J Ha, Y Kuk, and J A Stroscio. Scanning tunneling microscopy of gate tunable topological insulator Bi<sub>2</sub>Se<sub>3</sub> thin films. *Physical Review B*, 87(11):6, 2013.
- [239] P Messina, M Mannini, A Caneschi, D Gatteschi, L Sorace, P Sigalotti, C Sandrin, S Prato, P Pittana, and Y Manassen. Spin noise fluctuations from paramagnetic molecular adsorbates on surfaces. *Journal of Applied Physics*, 101(5):14, 2007.
- [240] C Durkan and M E Welland. Electronic spin detection in molecules using scanning-tunneling-microscopy-assisted electron-spin resonance. *Applied Physics Letters*, 80(3):458–460, 2002.
- [241] L Gorini, M Fabrizioli, M Mannini, L Sorace, and A Yakovenko. Addressing single molecules of a thin magnetic film. *Inorganica Chimica Acta*, 361(14-15):4089–4093, 2008.

- [242] V Mugnaini, M Fabrizioli, I Ratera, M Mannini, A Caneschi, D Gatteschi, Y Manassen, and J Veciana. Towards the detection of single polychlorotriphenylmethyl radical derivatives by means of Electron Spin Noise STM. *Solid State Sciences*, 11(5):956–960, 2009.
- [243] Thomas Schmid, Lothar Opilik, Carolin Blum, and Renato Zenobi. Nanoscale chemical imaging using tip-enhanced raman spectroscopy: A critical review. *Angewandte Chemie - International Edition*, 52:5940–5954, 2013.
- [244] Eric a. Pozzi, Matthew D. Sonntag, Nan Jiang, Jordan M. Klingsporn, Mark C. Hersam, and Richard P. Van Duyne. Tip-enhanced raman imaging: An emergent tool for probing biology at the nanoscale. *ACS Nano*, 7(2):885–888, 2013.
- [245] C Chen, N Hayazawa, and S Kawata. A 1.7 nm resolution chemical analysis of carbon nanotubes by tip-enhanced Raman imaging in the ambient. *Nat Commun*, 5:5, 2014.
- [246] W H Zhang, B S Yeo, T Schmid, and R Zenobi. Single molecule tip-enhanced Raman spectroscopy with silver tips. *Journal of Physical Chemistry C*, 111(4):1733–1738, 2007.
- [247] J Steidtner and B Pettinger. Tip-enhanced Raman spectroscopy and microscopy on single dye molecules with 15 nm resolution. *Physical Review Letters*, 100(23):4, 2008.
- [248] R Zhang, Y Zhang, Z C Dong, S Jiang, C Zhang, L G Chen, L Zhang, Y Liao, J Aizpurua, Y Luo, J L Yang, and J G Hou. Chemical mapping of a single molecule by plasmon-enhanced Raman scattering. *Nature*, 498(7452):82–86, 2013.
- [249] Matthew D Sonntag, Jordan M Klingsporn, Luis K Garibay, John M Roberts, Jon A Dieringer, Tamar Seideman, Karl A Scheidt, Lasse Jensen, George C Schatz, and Richard P Van Duyne. Single-Molecule Tip-Enhanced Raman Spectroscopy. pages 478–483, 2012.
- [250] N Jiang, E T Foley, J M Klingsporn, M D Sonntag, N A Valley, J A Dieringer, T Seideman, G C Schatz, M C Hersam, and R P Van Duyne. Observation of Multiple Vibrational Modes in Ultrahigh Vacuum Tip-Enhanced Raman Spectroscopy Combined with Molecular-Resolution Scanning Tunneling Microscopy. *Nano Letters*, 12(10):5061–5067, 2012.
- [251] Jordan M Klingsporn, Nan Jiang, Eric a Pozzi, Matthew D Sonntag, Dhabih Chulhai, Tamar Seideman, Lasse Jensen, Mark C Hersam, and Richard P Van Duyne. Intramolecular Insight into Adsorbate Substrate Interactions via Spectroscopy. *Journal of the American Chemical Society*, 136:3881–3887, 2014.
- [252] M Paulite, C Blum, T Schmid, L Opilik, K Eyer, G C Walker, and R Zenobi. Full Spectroscopic Tip-Enhanced Raman Imaging of Single Nanotapes Formed from beta-Amyloid(1-40) Peptide Fragments. *ACS Nano*, 7(2):911–920, 2013.
- [253] Carolin Blum, Thomas Schmid, Lothar Opilik, Norman Metanis, Simon Weidmann, and Renato Zenobi. Missing amide i mode in gap-mode tip-enhanced raman spectra of proteins. *Journal of Physical Chemistry C*, 116:23061–23066, 2012.

- [254] T Matsushima, T Okuda, T Eguchi, M Ono, A Harasawa, T Wakita, A Kataoka, M Hamada, A Kamoshida, Y Hasegawa, and T Kinoshita. Development and trial measurement of synchrotron-radiation-light-illuminated scanning tunneling microscope. *Review of Scientific Instruments*, 75(6):2149–2153, 2004.
- [255] V Rose, J W Freeland, State Govt Victoria Australian Govt Dept Innovat Ind Sci Australian Synchrotron, Elsevier Int Atom Energy Agcy Australian Res Council Mol Res, J J X ray A s Lightsources Mat Struct Network, Synchrotron Australian, and Adv Photon Source Argonne I L U S A Argonne Natl Lab. Nanoscale chemical imaging using synchrotron x-ray enhanced scanning tunneling microscopy. In *10th International Conference on Synchrotron Radiation Instrumentation*, volume 1234, pages 445–448, Melbourne, Australia, 2009. Amer Inst Physics.
- [256] N Shirato, M Cummings, H Kersell, Y Li, B Stripe, D Rosenmann, S W Hla, and V Rose. Elemental Fingerprinting of Materials with Sensitivity at the Atomic Limit. *Nano Letters*, 14(11):6499–6504, 2014.
- [257] V Rose, K K Wang, T Y Chien, J Hiller, D Rosenmann, J W Freeland, C Preissner, and S W Hla. Synchrotron X-Ray Scanning Tunneling Microscopy: Fingerprinting Near to Far Field Transitions on Cu(111) Induced by Synchrotron Radiation. *Advanced Functional Materials*, 23(20):2646–2652, 2013.
- [258] J T Groves, N Ulman, and S G Boxer. Micropatterning fluid lipid bilayers on solid supports. *Science (New York, N.Y.)*, 275(5300):651–653, 1997.
- [259] Paul S Cremer and Steven G Boxer. Formation and Spreading of Lipid Bilayers on Planar Glass Supports. *Journal of Physical Chemistry B*, 103(13):2554–2559, 1999.
- [260] Jay T Groves and Steven G Boxer. Micropattern formation in supported lipid membranes. *Accounts of Chemical Research*, 35(3):149–157, 2002.
- [261] Colin D Bain, E Barry Troughton, Yu Tai Tao, Joseph Evall, George M Whitesides, and Ralph G Nuzzo. Formation of monolayer films by the spontaneous assembly of organic thiols from solution onto gold. *Journal of the American Chemical Society*, 111(1):321–335, 1989.
- [262] Ralph G Nuzzo, Lawrence H Dubois, and David L Allara. Fundamental studies of microscopic wetting on organic surfaces. 1. Formation and structural characterization of a self-consistent series of polyfunctional organic monolayers. *Journal of the American Chemical Society*, 112(2):558–569, 1990.
- [263] Paul E Laibinis, George M Whitesides, David L Allara, Yu Tai Tao, Atul N Parikh, and Ralph G Nuzzo. Comparison of the structures and wetting properties of self-assembled monolayers of n-alkanethiols on the coinage metal surfaces, copper, silver, and gold. *Journal of the American Chemical Society*, 113(19):7152–7167, 1991.
- [264] J Christopher Love, Lara A Estroff, Jennah K Kriebel, Ralph G Nuzzo, and George M Whitesides. Self-assembled monolayers of thiolates on metals as a form of nanotechnology. *Chemical reviews*, 105(4):1103–69, 4 2005.

- [265] Gregory E Poirier. Characterization of Organosulfur Molecular Monolayers on Au(111) using Scanning Tunneling Microscopy. *Chemical Reviews (Washington, D. C.)*, 97(4):1117–1127, 1997.
- [266] Clemens Burda, Xiaobo Chen, Radha Narayanan, and Mostafa A El-Sayed. Chemistry and properties of nanocrystals of different shapes. *Chemical reviews*, 105(4):1025–1102, 2005.
- [267] A P Alivisatos. Semiconductor clusters, nanocrystals, and quantum dots. *Science (Washington, D. C.)*, 271(5251):933–937, 1996.
- [268] Michael L Steigerwald and Louis E Brus. Semiconductor crystallites: a class of large molecules. *Accounts of Chemical Research*, 23(6):183–188, 1990.
- [269] C B Murray, C R Kagan, and M G Bawendi. Synthesis and characterization of monodisperse nanocrystals and close-packed nanocrystal assemblies. *Annual Review of Materials Science*, 30:545–610, 2000.
- [270] Yasuhiro Shirasaki, Geoffrey J Supran, Mouni G Bawendi, and Vladimir Bulovic. Emergence of colloidal quantum-dot light-emitting technologies. *Nature Photonics*, 7(1):13–23, 2013.
- [271] Shelley A Claridge, A W Castleman Jr., Shiv N Khanna, Christopher B Murray, Ayusman Sen, and Paul S Weiss. Cluster-Assembled Materials. *ACS Nano*, 3(2):244–255, 2009.
- [272] A Paul Alivisatos, Weiwei Gu, and Carolyn Larabell. Quantum dots as cellular probes. *Annual Review of Biomedical Engineering*, 7:55–76, 2005.
- [273] A P Alivisatos, K P Johnsson, X Peng, T E Wilson, C J Loweth, M P Jr Bruchez, and P G Schultz. Organization of 'nanocrystal molecules' using DNA. *Nature*, 382(6592):609–611, 1996.
- [274] Liberato Manna, Erik C Scher, and A Paul Alivisatos. Synthesis of Soluble and Processable Rod-, Arrow-, Teardrop-, and Tetrapod-Shaped CdSe Nanocrystals. *Journal of the American Chemical Society*, 122(51):12700–12706, 2000.
- [275] C A Mirkin, R L Letsinger, R C Mucic, and J J Storhoff. A DNA-based method for rationally assembling nanoparticles into macroscopic materials. *Nature*, 382(6592):607–609, 1996.
- [276] Sung Yong Park, Abigail K R Lytton-Jean, Byeongdu Lee, Steven Weigand, George C Schatz, and Chad A Mirkin. DNA-programmable nanoparticle crystallization. *Nature (London, United Kingdom)*, 451(7178):553–556, 2008.
- [277] A K Geim. Graphene: Status and Prospects. *Science (Washington, DC, United States)*, 324(5934):1530–1534, 2009.
- [278] Andrew Kozbial, Zhiting Li, Caitlyn Conaway, Rebecca McGinley, Shonali Dhingra, Vahid Vahdat, Feng Zhou, Brian D'Urso, Haitao Liu, and Lei. Li. Surface energy of graphene by contact angle measurement. *Langmuir*, 30(28):8598–8606, 2014.
- [279] Steven De Feyter and Frans C. De Schryver. Two-dimensional supramolecular self-assembly probed by scanning tunneling microscopy. *Chemical Society Reviews*, 32(3):139–150, 4 2003.



- [280] L C Giancarlo and G W Flynn. Raising flags: applications of chemical marker groups to study self-assembly, chirality, and orientation of interfacial films by scanning tunneling microscopy. *Accounts of chemical research*, 33(7):491–501, 2000.
- [281] Donna M. Cyr, Bhawani Venkataraman, and George W. Flynn. STM Investigations of Organic Molecules Physisorbed at the LiquidSolid Interface. *Chemistry of Materials*, 8(8):1600–1615, 1 1996.
- [282] Johannes A A W Elemans, Shengbin Lei, and Steven. De Feyter. Molecular and Supramolecular Networks on Surfaces: From Two-Dimensional Crystal Engineering to Reactivity. *Angewandte Chemie, International Edition*, 48(40):7298–7332, 2009.
- [283] Xiaobo Mao, Yuanyuan Guo, Yin Luo, Lin Niu, Lei Liu, Xiaojing Ma, Huibin Wang, Yanlian Yang, Guanghong Wei, and Chen. Wang. Sequence Effects on Peptide Assembly Characteristics Observed by Using Scanning Tunneling Microscopy. *Journal of the American Chemical Society*, 135(6):2181–2187, 2013.
- [284] Hiroyasu Furukawa, Kyle E Cordova, Michael O’Keeffe, and Omar M Yaghi. The Chemistry and Applications of Metal-Organic Frameworks. *Science (Washington, DC, United States)*, 341(6149):974, 2013.
- [285] P Samori, A Fechtenkotter, F Jackel, T Bohme, K Mullen, and J P Rabe. Supramolecular staircase via self-assembly of disklike molecules at the solid-liquid interface. *Journal of the American Chemical Society*, 123(46):11462–11467, 2001.
- [286] Andrew J Gellman and Kris R Paserba. Kinetics and Mechanism of Oligomer Desorption from Surfaces: n-Alkanes on Graphite. *Journal of Physical Chemistry B*, 106(51):13231–13241, 2002.
- [287] John W Colson, Arthur R Woll, Arnab Mukherjee, Mark P Levendorf, Eric L Spitler, Virgil B Shields, Michael G Spencer, Jiwoong Park, and William R Dichtel. Oriented 2D Covalent Organic Framework Thin Films on Single-Layer Graphene. *Science (Washington, DC, United States)*, 332(6026):228–231, 2011.
- [288] D Cui, J M MacLeod, M Ebrahimi, F Rosei, and D F Perepichka. Solution and air stable host/guest architectures from a single layer covalent organic framework. *Chemical communications (Cambridge, England)*, 51(92):16510–16513, 2015.
- [289] Y Okawa and M Aono. Nanoscale control of chain polymerization. *Nature*, 409(6821):683–684, 2001.
- [290] Y Okawa, M Akai-Kasaya, Y Kuwahara, S K Mandal, and M Aono. Controlled chain polymerisation and chemical soldering for single-molecule electronics. *Nanoscale*, 4(10):3013–3028, 2012.
- [291] Aparna Deshpande, Chun-Hong Sham, Justice M P Alaboson, Jonathan M Mullin, George C Schatz, and Mark C Hersam. Self-Assembly and Photopolymerization of Sub-2 nm One-Dimensional Organic Nanostructures on Graphene. *Journal of the American Chemical Society*, 134(40):16759–16764, 2012.

- [292] Kazukuni Tahara, Keisuke Katayama, Matthew Oliver Blunt, Kohei Iritani, Steven De Feyter, and Yoshito. Tobe. Functionalized Surface-Confined Pores: Guest Binding Directed by Lateral Noncovalent Interactions at the Solid-Liquid Interface. *ACS Nano*, 8(8):8683–8694, 2014.
- [293] C D Bain and G M Whitesides. A study by contact-angle of the acid-base behavior of monolayers containing omega-mercaptocarboxylic acids adsorbed on gold - an example of reactive spreading. *Langmuir*, 5(6):1370–1378, 1989.
- [294] Kenan P Fears, Stephen E Creager, and Robert A Latour. Determination of the Surface pK of Carboxylic- and Amine-Terminated Alkanethiols Using Surface Plasmon Resonance Spectroscopy. *Langmuir*, 24(3):837–843, 2008.
- [295] *Biochemistry of Lipids, Lipoproteins and Membranes*. Elsevier, 2008.
- [296] Derek Marsh. *Handbook of Lipid Bilayers*.
- [297] Mitchell J Shuster, Amit Vaish, Matthew E Szapacs, Mary E Anderson, Paul S Weiss, and Anne M Andrews. Biospecific recognition of tethered small molecules diluted in self-assembled monolayers. *Advanced Materials (Weinheim, Germany)*, 20(1):164–167, 2008.
- [298] Amit Vaish, Mitchell J Shuster, Sarawut Cheunkar, Yogesh S Singh, Paul S Weiss, and Anne M Andrews. Native Serotonin Membrane Receptors Recognize 5-Hydroxytryptophan-Functionalized Substrates: Enabling Small-Molecule Recognition. *ACS Chemical Neuroscience*, 1(7):495–504, 2010.
- [299] D F O’Brien, T H Whitesides, and R T Klingbiel. The photopolymerization of lipid-diacetylenes in bimolecular-layer membranes. *Journal of Polymer Science, Polymer Letters Edition*, 19(3):95–101, 1981.
- [300] Han Zhang, James R. Joubert, and S. Scott Saavedra. Membranes from Polymerizable Lipids. pages 1–42. Springer, Berlin, Heidelberg, 2009.
- [301] Encarnacion Lopez, David F O’Brien, and Thomas H Whitesides. Structural effects on the photopolymerization of bilayer membranes. *Journal of the American Chemical Society*, 104(1):305–307, 1982.
- [302] R H Baughman. Solid-state polymerization of diacetylenes. *Journal of Applied Physics*, 43(11):4362–&, 1972.
- [303] Gerhard. Wegner. Topochemical reactions of monomers with conjugated triple bonds. IV. Polymerization of 2,4-hexadiyne-1,6-diol bis(p-toluenesulfonate). *Makromolekulare Chemie*, 145:85–94, 1971.
- [304] Yuji Okawa, Daisuke Takajo, Shigeru Tsukamoto, Tsuyoshi Hasegawa, and Masakazu. Aono. Atomic force microscopy and theoretical investigation of the lifted-up conformation of polydiacetylene on a graphite substrate. *Soft Matter*, 4(5):1041–1047, 2008.
- [305] Osamu Endo, Naoya Toda, Hiroyuki Ozaki, and Yasuhiro. Mazaki. Domain structure of 17,19-hexatriacontadiyne monolayers formed on graphite (0 0 0 1) surfaces studied by UHV-STM. *Surface Science*, 545(1-2):41–46, 2003.

- [306] Shane R Russell and Shelley A Claridge. Peptide interfaces with graphene: an emerging intersection of analytical chemistry, theory, and materials. *Analytical and Bioanalytical Chemistry*, 408(11):2649–2658, 2016.
- [307] Mark A Bryant and Richard M Crooks. Determination of surface pKa values of surface-confined molecules derivatized with pH-sensitive pendant groups. *Langmuir*, 9(2):385–387, 1993.
- [308] Xiaolin Zhao, Suchitra Subrahmanyam, and Kenneth B Eisenthal. Determination of pKa at the air/water interface by second harmonic generation. *Chemical Physics Letters*, 171(5-6):558–562, 1990.
- [309] William M. Haynes. *CRC handbook of chemistry and physics : a ready-reference book of chemical and physical data*.
- [310] Jacob N. Israelachvili. *Intermolecular and surface forces*. Academic Press, 2011.
- [311] L A Bumm and P S Weiss. Small cavity nonresonant tunable microwave-frequency alternating current scanning tunneling microscope. *Review of Scientific Instruments*, 66(8):4140–4145, 1995.
- [312] J J Bang, S R Russell, K K Rupp, and S A Claridge. Multimodal scanning probe imaging: nanoscale chemical analysis from biology to renewable energy. *Analytical Methods*, 7(17):7106–7127, 2015.
- [313] Wei-Ssu Liao, Sarawut Cheunkar, Huan H Cao, Heidi R Bednar, Paul S Weiss, and Anne M Andrews. Subtractive Patterning via Chemical Lift-Off Lithography. *Science (Washington, DC, United States)*, 337(6101):1517–1521, 2012.
- [314] Steven De Feyter and Frans C De Schryver. Self-assembly at the liquid/solid interface: STM reveals. *The journal of physical chemistry. B*, 109(10):4290–302, 3 2005.
- [315] Yuji Okawa, Swapan K Mandal, Chunping Hu, Yoshitaka Tateyama, Stefan Goedecker, Shigeru Tsukamoto, Tsuyoshi Hasegawa, James K Gimzewski, and Masakazu. Aono. Chemical Wiring and Soldering toward All-Molecule Electronic Circuitry. *Journal of the American Chemical Society*, 133(21):8227–8233, 2011.
- [316] B Tieke, H J Graf, G Wegner, B Naegelé, H Ringsdorf, A Banerjee, D Day, and J B Lando. Polymerization of mono- and multilayer forming diacetylenes. *Colloid and Polymer Science*, 255(6):521–531, 1977.
- [317] B Li, K Tahara, J Adisoejoso, W Vanderlinden, K S Mali, S De Gendt, Y Tobe, and S De Feyter. Self-Assembled Air-Stable Supramolecular Porous Networks on Graphene. *ACS nano*, 7(12):10764–10772, 2013.
- [318] Jae Jin Bang, Kortney K Rupp, Shane R Russell, Shi Wah Choong, and Shelley A Claridge. Sitting Phases of Polymerizable Amphiphiles for Controlled Functionalization of Layered Materials. *Journal of the American Chemical Society*, 138(13):4448–4457, 2016.
- [319] Kunal S Mali, Nicholas Pearce, Steven De Feyter, and Neil R Champness. Frontiers of supramolecular chemistry at solid surfaces. *Chemical Society Reviews*, 46(9):2520–2542, 2017.

- [320] S W Choong, S R Russell, J J Bang, J K Patterson, and S A Claridge. Sitting Phase Monolayers of Polymerizable Phospholipids Create Dimensional, Molecular-Scale Wetting Control for Scalable Solution Based Patterning of Layered Materials. *ACS Applied Materials & Interfaces*, 9(22):19326–19334, 2017.
- [321] T A Villarreal, S R Russell, J J Bang, J K Patterson, and S A Claridge. Modulating Wettability of Layered Materials by Controlling Ligand Polar Headgroup Dynamics. *Journal of the American Chemical Society*, 139(34):11973–11979, 2017.
- [322] Tyler R Hayes, Jae Jin Bang, Tyson C Davis, Caroline F Peterson, David G McMillan, and Shelley A Claridge. Multimicrometer Noncovalent Monolayer Domains on Layered Materials through Thermally Controlled LangmuirSchaefer Conversion for Noncovalent 2D Functionalization. *ACS Applied Materials & Interfaces*, 9(41):36409–36416, 2017.
- [323] D Vollhardt and V B Fainerman. Characterisation of phase transition in adsorbed monolayers at the air/water interface. *Advances in colloid and interface science*, 154(1-2):1–19, 2010.
- [324] Vladimir M. Kaganer, Helmuth Möhwald, and Pulak Dutta. Structure and phase transitions in Langmuir monolayers. *Reviews of Modern Physics*, 71(3):779–819, 4 1999.
- [325] Charles M Knobler and Daniel K Schwartz. Langmuir and self-assembled monolayers. *Current Opinion in Colloid & Interface Science*, 4(1):46–51, 1999.
- [326] D K Schwartz. Mechanisms and kinetics of self-assembled monolayer formation. *Annual review of physical chemistry*, 52:107–137, 2001.
- [327] Canay Ege, Maria K Ratajczak, Jaroslaw Majewski, Kristian Kjaer, and Ka Yee C Lee. Evidence for lipid/cholesterol ordering in model lipid membranes. *Biophysical Journal*, 91(1):L1–L3, 2006.
- [328] J Ding, D Y Takamoto, Nahmen A von, M M Lipp, K Y Lee, A J Waring, and J A Zasadzinski. Effects of lung surfactant proteins, SP-B and SP-C, and palmitic acid on monolayer stability. *Biophysical journal*, 80(5):2262–2272, 2001.
- [329] Katherine B Blodgett. Monomolecular films of fatty acids on glass. *Journal of the American Chemical Society*, 56:495, 1934.
- [330] Xiaodong Chen, Steven Lenhart, Michael Hirtz, Nan Lu, Harald Fuchs, and Lifeng Chi. Langmuir-Blodgett Patterning: A Bottom-Up Way to Build Mesostructures over Large Areas. *Accounts of Chemical Research*, 40(6):393–401, 2007.
- [331] Shelli L Frey, Eva Y Chi, Cristobal Arratia, Jaroslaw Majewski, Kristian Kjaer, and Ka Yee C Lee. Condensing and fluidizing effects of ganglioside GM1 on phospholipid films. *Biophysical Journal*, 94(8):3047–3064, 2008.
- [332] Yuji Okawa and Masakazu. Aono. Materials science: Nanoscale control of chain polymerization. *Nature (London)*, 409(6821):683–684, 2001.

- [333] K Takami, Y Kuwahara, T Ishii, M Akai-Kasaya, A Saito, and M Aono. Significant increase in conductivity of polydiacetylene thin film induced by iodine doping. *Surface Science*, 591(1-3):L273–L279, 2005.
- [334] R M Morelis, A P Girard-Egrot, and P R Coulet. Dependence of Langmuir-Blodgett film quality on fatty acid monolayer integrity. 1. Nucleation crystal growth avoidance in the monolayer through the optimized compression procedure. *Langmuir*, 9(11):3101–3106, 1993.
- [335] A P Girard-Egrot, R M Morelis, and P R Coulet. Dependence of Langmuir-Blodgett film quality on fatty acid monolayer integrity. 2. Crucial effect of the removal rate of monolayer during Langmuir-Blodgett film deposition. *Langmuir*, 9(11):3107–3110, 1993.
- [336] R Aveyard, B P Binks, P D I Fletcher, and X Ye. Contact angles and transfer ratios measured during the Langmuir-Blodgett deposition of docosanoic acid onto mica from CdCl<sub>2</sub> subphases. *Colloids and Surfaces, A: Physicochemical and Engineering Aspects*, 94(2/3):279–289, 1995.
- [337] Irving Langmuir, V J Schaefer, and Harry. Sobotka. Multilayers of sterols and the adsorption of digitonin by deposited monolayers. *Journal of the American Chemical Society*, 59:1751–1759, 1937.
- [338] E P Honig, J H Th. Hengst, and D Den Engelsen. Langmuir-Blodgett deposition ratios. *Journal of Colloid and Interface Science*, 45(1):92–102, 1973.
- [339] K B Blodgett. Films built by depositing successive monomolecular layers on a solid surface. *Journal of the American Chemical Society*, 57(1):1007–1022, 1935.
- [340] Jin Liu and John C Conboy. 1,2-Diacyl-phosphatidylcholine flip-flop measured directly by sum-frequency vibrational spectroscopy. *Biophysical Journal*, 89(4):2522–2532, 2005.
- [341] Gabriel P Lopez, Hans A Biebuyck, and George M Whitesides. Scanning electron microscopy can form images of patterns in self-assembled monolayers. *Langmuir*, 9(6):1513–1516, 1993.
- [342] Charan Srinivasan, Thomas J Mullen, J Nathan Hohman, Mary E Anderson, Arrelaine A Dameron, Anne M Andrews, Elizabeth C Dickey, Mark W Horn, and Paul S Weiss. Scanning Electron Microscopy of Nanoscale Chemical Patterns. *ACS Nano*, 1(3):191–201, 2007.
- [343] Nathan H Mack, Rui Dong, and Ralph G Nuzzo. Quantitative Imaging of Protein Adsorption on Patterned Organic Thin-Film Arrays Using Secondary Electron Emission. *Journal of the American Chemical Society*, 128(24):7871–7881, 2006.
- [344] A G Bittermann, S Jacobi, L F Chi, H Fuchs, and R Reichelt. Contrast Studies on Organic Monolayers of Different Molecular Packing in FESEM and Their Correlation with SFM Data. *Langmuir*, 17(6):1872–1877, 2001.
- [345] D Vollhardt and V B Fainerman. Characterisation of phase transition in adsorbed monolayers at the air/water interface. *Advances in Colloid and Interface Science*, 154(1-2):1–19, 2010.

- [346] Brian G Moore, Charles M Knobler, Silvere Akamatsu, and Francis Rondelez. Phase diagram of Langmuir monolayers of pentadecanoic acid: quantitative comparison of surface pressure and fluorescence microscopy results. *Journal of Physical Chemistry*, 94(11):4588–4595, 1990.
- [347] L F Chi, L M Eng, K Graf, and H Fuchs. Structure and stability of Langmuir-Blodgett films investigated by scanning force microscopy. *Langmuir*, 8(9):2255–2261, 1992.
- [348] L F Chi, H Fuchs, R R Johnston, and H Ringsdorf. Investigations of phase-separated Langmuir-Blodgett films by atomic force microscopy. *Thin Solid Films*, 242(1-2):151–156, 1994.
- [349] Hans Riegler and Karl Spratte. Structural changes in lipid monolayers during the Langmuir-Blodgett transfer due to substrate/monolayer interactions. *Thin Solid Films*, 210-211(Part 1):9–12, 1992.
- [350] Fazale R Rana, Suci Widayati, Brian W Gregory, and Richard A Dluhy. Metastability in monolayer films transferred onto solid substrates by the Langmuir-Blodgett method: IR evidence for transfer-induced phase transitions. *Applied Spectroscopy*, 48(10):1196–1203, 1994.
- [351] B Tieke, G Lieser, and G Wegner. Polymerization of diacetylenes in multilayers. *Journal of Polymer Science Part a-Polymer Chemistry*, 17(6):1631–1644, 1979.
- [352] Gerhard. Wegner. Topochemical reactions of monomers with conjugated triple bonds. I. Polymerization of derivatives of 2,4-hexadiyne-1,6-diols in the crystalline state. *Zeitschrift fuer Naturforschung, Teil B: Anorganische Chemie, Organische Chemie, Biochemie, Biophysik, Biologie*, 24(7):824–832, 1969.
- [353] H. Bässler. Photopolymerization of diacetylenes. In *Polydiacetylenes*, pages 1–48. Springer-Verlag, Berlin/Heidelberg, 1984.
- [354] Karl M Robinson, Carlos Hernandez, and J Adin Mann Jr. In situ x-ray diffraction of diacetylene monolayers. *Thin Solid Films*, 210-211(Part 1):73–75, 1992.
- [355] Chunbo Yuan, Jennifer Furlong, Pierre Burgos, and Linda J Johnston. The size of lipid rafts: an atomic force microscopy study of ganglioside GM1 domains in sphingomyelin/DOPC/cholesterol membranes. *Biophysical Journal*, 82(5):2526–2535, 2002.
- [356] John R Silvius. Role of cholesterol in lipid raft formation: lessons from lipid model systems. *Biochimica et Biophysica Acta, Biomembranes*, 1610(2):174–183, 2003.
- [357] Claudia Steinem, Andreas Janshoff, Wolf-Peter Ulrich, Manfred Sieber, and Hans-Joachim Galla. Impedance analysis of supported lipid bilayer membranes: a scrutiny of different preparation techniques. *Biochimica et Biophysica Acta (BBA) - Biomembranes*, 1279(2):169–180, 3 1996.
- [358] David Nečas and Petr Klapetek. Gwyddion: an open-source software for SPM data analysis, 2012.
- [359] Caroline A Schneider, Wayne S Rasband, and Kevin W Eliceiri. NIH Image to ImageJ: 25 years of image analysis. *Nature Methods*, 9(7-part1):671–675, 2012.

- [360] A. H. Castro Neto, N. M. R. Peres, K. S. Novoselov, and A. K. Geim. The electronic properties of graphene. *Reviews of Modern Physics*, 81(1):109–162, 1 2009.
- [361] D Chen, L H Tang, and J H Li. Graphene-based materials in electrochemistry. *Chemical Society reviews*, 39(8):3157–3180, 2010.
- [362] D Jariwala, T J Marks, and M C Hersam. Mixed-dimensional van der Waals heterostructures. *Nature Materials*, 16(2):170–181, 2017.
- [363] K S Novoselov, A Mishchenko, A Carvalho, and A H C Neto. 2D materials and van der Waals heterostructures. *Science*, 353(6298):7, 2016.
- [364] Y Q Sun, Q O Wu, and G Q Shi. Graphene based new energy materials. *Energy & Environmental Science*, 4(4):1113–1132, 2011.
- [365] A Kumar, K Banerjee, and P Liljeroth. Molecular assembly on two-dimensional materials. *Nanotechnology*, 28(8), 2017.
- [366] V Georgakilas, M Otyepka, A B Bourlinos, V Chandra, N Kim, K C Kemp, P Hobza, R Zboril, and K S Kim. Functionalization of Graphene: Covalent and Non-Covalent Approaches, Derivatives and Applications. *Chemical Reviews*, 112(11):6156–6214, 2012.
- [367] T Kuila, S Bose, A K Mishra, P Khanra, N H Kim, and J H Lee. Chemical functionalization of graphene and its applications. *Progress in Materials Science*, 57(7):1061–1105, 2012.
- [368] G Wegner. Topochemical Reactions of Monomers with Conjugated Triple Bonds .3. Solid-State Reactivity of Derivatives of Diphenyldiacetylene. *Journal of Polymer Science Part B-Polymer Letters*, 9(2):133–144, 1971.
- [369] S Nakamura, H Nakahara, M P Krafft, and O Shibata. Two-component Langmuir monolayers of single-chain partially fluorinated amphiphiles with dipalmitoylphosphatidylcholine (DPPC). *Langmuir*, 23(25):12634–12644, 2007.
- [370] K Y C Lee, A Gopal, A von Nahmen, J A Zasadzinski, J Majewski, G S Smith, P B Howes, and K Kjaer. Influence of palmitic acid and hexadecanol on the phase transition temperature and molecular packing of dipalmitoylphosphatidyl-choline monolayers at the air-water interface. *Journal of Chemical Physics*, 116(2):774–783, 2002.
- [371] D Vollhardt. Effect of unsaturation in fatty acids on the main characteristics of Langmuir monolayers. *Journal of Physical Chemistry C*, 111(18):6805–6812, 2007.
- [372] H Jiang and R Jelinek. Mixed Diacetylene/Octadecyl Melamine Nanowires Formed at the Air/Water Interface Exhibit Unique Structural and Colorimetric Properties. *Langmuir*, 31(21):5843–5850, 2015.
- [373] B P Binks. Insoluble monolayers of weakly ionizing low molar mass materials and their deposition to form Langmuir-Blodgett multilayers. *Advances in Colloid and Interface Science*, 34:343–432, 1991.

- [374] J Liu and J C Conboy. Structure of a gel phase lipid bilayer prepared by the Langmuir-Blodgett/Langmuir-Schaefer method characterized by sum-frequency vibrational spectroscopy. *Langmuir*, 21(20):9091–9097, 2005.
- [375] I Pascher. Molecular Arrangements in Sphingolipids Conformation and Hydrogen-Bonding of Ceramide and Their Implication on Membrane Stability and Permeability. *Biochimica Et Biophysica Acta*, 455(2):433–451, 1976.
- [376] J P Slotte. The importance of hydrogen bonding in sphingomyelin’s membrane interactions with co-lipids. *Biochimica Et Biophysica Acta-Biomembranes*, 1858(2):304–310, 2016.
- [377] J D Lambert and E D T Strong. The Dimerization of Ammonia and Amines. *Proceedings of the Royal Society of London. Series A, Mathematical and Physical Sciences*, 200(1063):566–572, 1950.
- [378] T Kosztolanyi, I Bako, and G Palinkas. Hydrogen Bonding in Liquid Methanol, Methylamine, and Methanethiol Studied by Molecular-Dynamics Simulations. *Journal of Chemical Physics*, 118(10):4546–4555, 2003.
- [379] J Chocholousova, J Vacek, and P Hobza. Acetic Acid Dimer in the Gas Phase, Nonpolar Solvent, Microhydrated Environment, and Dilute and Concentrated Acetic acid: Ab initio Quantum Chemical and Molecular Dynamics Simulations. *Journal of Physical Chemistry A*, 107(17):3086–3092, 2003.
- [380] D A Dixon, K D Dobbs, and J J Valentini. Amide-Water and Amide-Amide Hydrogen-Bond Strengths. *Journal of Physical Chemistry*, 98(51):13435–13439, 1994.
- [381] S Kim, M S Jhon, and H A Scheraga. Analytic Intermolecular Potential Functions from ab Initio SCF Calculations of Interaction Energies between CH<sub>4</sub>, CH<sub>3</sub>OH, CH<sub>3</sub>COOH, and CH<sub>3</sub>COO<sup>-</sup> and Water. *Journal of Physical Chemistry*, 92(26):7216–7223, 1988.
- [382] B Marten, K Kim, C Cortis, R A Friesner, R B Murphy, M N Ringnalda, D Sitkoff, and B Honig. New model for calculation of solvation free energies: Correction of self-consistent reaction field continuum dielectric theory for short-range hydrogen-bonding effects. *Journal of Physical Chemistry*, 100(28):11775–11788, 1996.
- [383] K Ariga, T Nakanishi, J P Hill, M Shirai, M Okuno, T Abe, and J Kikuchi. Tunable pK of amino acid residues at the air-water interface gives an L-zyzyme (Langmuir enzyme). *Journal of the American Chemical Society*, 127(34):12074–12080, 2005.
- [384] J R Kanicky and D O Shah. Effect of degree, type, and position of unsaturation on the pK(a) of long-chain fatty acids. *Journal of Colloid and Interface Science*, 256(1):201–207, 2002.
- [385] A M Bouchet, M A Frias, E Lairion, F Martini, H Almaleck, G Gordillo, and E A Disalvo. Structural and dynamical surface properties of phosphatidylethanolamine containing membranes. *Biochimica Et Biophysica Acta-Biomembranes*, 1788(5):918–925, 2009.



- [386] G Vanderkooi. Crystal-Refined Hydrogen-bond Potentials for Interactions Involving the Phosphate Group. *Journal of Physical Chemistry*, 87(25):5121–5129, 1983.
- [387] M Pasenkiewicz-Gierula, Y Takaoka, H Miyagawa, K Kitamura, and A Kusumi. Charge pairing of headgroups in phosphatidylcholine membranes: A molecular dynamics simulation study. *Biophysical journal*, 76(3):1228–1240, 1999.
- [388] J Milhaud. New insights into water-phospholipid model membrane interactions. *Biochimica Et Biophysica Acta-Biomembranes*, 1663(1-2):19–51, 2004.
- [389] K S Kim, J Y Lee, S J Lee, T K Ha, and D H Kim. On Binding Forces between Aromatic Ring and Quaternary Ammonium Compound. *Journal of the American Chemical Society*, 116(16):7399–7400, 1994.
- [390] Robert B Gennis. The Structures and Properties of Membrane Lipids. In *Biomembranes: Molecular Structure and Function*, pages 36–84. Springer New York, New York, NY, 1989.
- [391] Michael Canavan Phillips and Dennis. Chapman. Monolayer characteristics of saturated 1,2-diacyl phosphatidylcholines (lecithins) and phosphatidylethanolamines at the air-water interfact. *Biochimica et Biophysica Acta, Biomembranes*, 163(3):301–313, 1968.
- [392] T J McIntosh. Hydration properties of lamellar and non-lamellar phases of phosphatidylcholine and phosphatidylethanolamine. *Chemistry and Physics of Lipids*, 81(2):117–131, 1996.
- [393] M Sovago, G W H Wurpel, M Smits, M Muller, and M Bonn. Calcium-induced phospholipid ordering depends on surface pressure. *Journal of the American Chemical Society*, 129(36):11079–11084, 2007.
- [394] J Yang, C Calero, M Bonomi, and J Marti. Specific Ion Binding at Phospholipid Membrane Surfaces. *Journal of Chemical Theory and Computation*, 11(9):4495–4499, 2015.
- [395] J W Zhang, A Ebrahimpour, and G H Nancollas. Ion Association in Calcium-Phosphate Solutions at 37 Degree Celsius. *Journal of Solution Chemistry*, 20(5):455–465, 1991.
- [396] L W Bruch, R D Diehl, and J A Venables. Progress in the Measurement and Modeling of Physisorbed Layers. *Reviews of Modern Physics*, 79(4):1381–1454, 2007.
- [397] M A Castro, S M Clarke, A Inaba, C C Dong, and R K Thomas. Crystalline Monolayer of Dodecanoic Acid Adsorbed on Graphite from n-Heptane Solution. *Journal of Physical Chemistry B*, 102(5):777–781, 1998.
- [398] D Cohen and Y Zeiri. Molecular-Dynamics Study of the Surface-Diffusion of n-Alkane like Adsorbates. 2. Role of Chain Stiffness. *Surface Science*, 274(1):173–184, 1992.


- [399] K P Kootery, H Jiang, S Kolusheva, T P Vinod, M Ritenberg, L Zeiri, R Volinsky, D Malferrari, P Galletti, E Tagliavini, and R Jelinek. Poly(methyl methacrylate)-Supported Polydiacetylene Films: Unique Chromatic Transitions and Molecular Sensing. *ACS Applied Materials & Interfaces*, 6(11):8613–8620, 2014.
- [400] H Jiang and R Jelinek. Dramatic Shape Modulation of Surfactant/Diacetylene Microstructures at the Air-Water Interface. *Chemistry - A European Journal*, 20(50):16747–16752, 2014.
- [401] S Ampornpun, S Montha, G Tumcharern, V Vchirawongkwin, M Sukwat-tanasinitt, and S Wacharasindhu. Odd-Even and Hydrophobicity Effects of Diacetylene Alkyl Chains on Thermochromic Reversibility of Symmetrical and Unsymmetrical Diyndiamide Polydiacetylenes. *Macromolecules*, 45(22):9038–9045, 2012.

## PUBLICATION

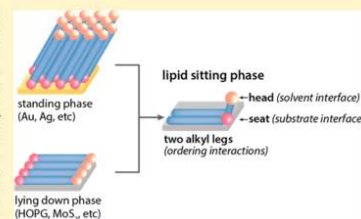
## Sitting Phases of Polymerizable Amphiphiles for Controlled Functionalization of Layered Materials

Jae Jin Bang,<sup>†</sup> Kortney K. Rupp,<sup>‡</sup> Shane R. Russell,<sup>‡</sup> Shi Wah Choong,<sup>†</sup> and Shelley A. Claridge<sup>\*,†,‡</sup>

<sup>†</sup>Department of Chemistry and <sup>‡</sup>Weldon School of Biomedical Engineering, Purdue University, West Lafayette, Indiana 47907, United States

 Supporting Information

**ABSTRACT:** Precisely tailoring surface chemistry of layered materials is a growing need for fields ranging from electronics to biology. For many applications, the need for noncovalently adsorbed ligands to simultaneously control interactions with a nonpolar substrate and a polar solvent is a particular challenge. However, biology routinely addresses a similar challenge in the context of the lipid bilayer. While conventional standing phases of phospholipids (such as those found in a bilayer) would not provide spatially ordered interactions with the substrate, here we demonstrate formation of a sitting phase of polymerizable phospholipids, in which the two alkyl chains extend along the surface and the two ionizable functionalities (a phosphate and an amine) sit adjacent to the substrate and project into the solvent, respectively. Interfacial ordering and polymerization are assessed by high-resolution scanning probe measurements. Water contact angle titrations demonstrate interfacial  $pK_a$  shifts for the lipid phosphate but not for the amine, supporting localization of the phosphate near the nonpolar graphite surface.



### INTRODUCTION

Precisely controlling surface chemistry using self-assembled monolayers (SAMs) and bilayers has been a central focus of research in both synthetic and biological interfaces.<sup>1–4</sup> Much synthetic monolayer chemistry has its basis in the formation of SAMs of alkanethiols on gold and the coinage metals, pioneered by groups including those of Whitesides, Nuzzo, and Allara in the 1980s.<sup>5–8</sup> Standing-up phases of alkanethiol monolayers form based on a combination of covalent or ionic molecule–substrate interactions (e.g., Au–S), strong molecule–molecule van der Waals interactions (e.g., between long alkyl chains) that improve ordering, and a terminal functionality (e.g.,  $-\text{CH}_3$ ,  $-\text{COOH}$ ,  $-\text{NH}_2$ , biotin, DNA) that confers solvent wetting properties and/or selectivity for analytes.<sup>8,9</sup> The surge of interest in colloidal nanocrystals<sup>10–15</sup> has further increased the importance of monolayer chemistry as well as opened entirely new avenues for control of morphology, electronic properties, solubility, and analyte binding.<sup>16–20</sup>

Layered materials (e.g., HOPG, graphene,  $\text{MoS}_2$ )<sup>21,22</sup> represent a new frontier in utilizing monolayer chemistry to control physical properties and solubility<sup>23,24</sup> but also introduce substantial challenges.<sup>23,25</sup> In single-layer graphene, for instance, all atoms are surface atoms and in solution can actually be coordinated through two faces, promising unusually high levels of electronic control through the design and spatial organization of appropriate ligands.<sup>23,24</sup> In contrast with colloidal nanoscopic materials, in which surface curvature typically decreases ligand ordering, the relative flatness of a

layered material surface enables ligand ordering that can more strongly resemble SAMs on extended solids.<sup>23,26</sup> However, maintenance of extended  $\pi$ -conjugation in the layer requires noncovalent functionalization, restricting the choice of ligands.<sup>26</sup> These challenges have impacted the utility of graphene and other layered materials in many applications.

Monolayers on highly oriented pyrolytic graphite (HOPG) and graphene are frequently formed on the basis of lying-down phases of molecules;<sup>23,24,26,27</sup> the increased surface area of the molecule–substrate interaction partially offsets the decreased per-atom interaction strength of noncovalent (vs covalent) interactions.<sup>23</sup> Two common classes of adsorption motifs utilized are long alkanes (e.g., 23-carbon tricosane)<sup>28,29</sup> and planar aromatic hydrocarbons (e.g., pyrene, anthracene).<sup>24,30</sup> In noncovalent monolayers, molecule–molecule interactions also play a more prominent role in monolayer stability. These may be based on van der Waals interactions between long alkanes such as tricosane, one or more hydrogen-bonding interactions (e.g., between planar aromatic molecules that display carboxylic acids on their peripheries<sup>31</sup> or  $\beta$ -strand peptides that hydrogen bond to form  $\beta$ -sheets<sup>32,33</sup>), or ionic interactions (e.g., in MOFs<sup>34</sup>).

However, even between very long alkanes, intermolecular forces are relatively weak ( $\sim 5$  kJ/mol of  $\text{CH}_2$  between alkane chains<sup>35</sup> and 5–10 kJ/mol of  $\text{CH}_2$  for alkane–HOPG

Received: December 16, 2015  
Published: March 14, 2016

interactions<sup>36</sup>). Thus, an extension of this strategy involves noncovalent functionalization using lying-down phases of reactive molecules, followed by polymerization within the layer.<sup>37–39</sup> One such route is based on self-assembly of long-chain carboxylic acids derivatized with an internal diyne that can be photopolymerized to yield a conjugated ene-yne polymer.<sup>37,40–43</sup> A number of studies have examined this reaction on HOPG,<sup>37,43,44</sup> graphene,<sup>45</sup> and MoS<sub>2</sub>,<sup>42,46</sup> due to interest in the conductive ene-yne as a molecular wire. Such a strategy can produce monolayers that exhibit some solvent stability,<sup>39,47</sup> but a new challenge arises. Early work on monolayers on bulk metals has demonstrated that functional groups positioned adjacent to a hydrophobic monolayer interface undergo large  $pK_a$  shifts (frequently 4 units or more) due to the inability of the interface to stabilize the charged form of the molecule.<sup>48,49</sup> These shifts mean that groups such as carboxylic acids and amines may be predominantly neutral near pH 7 (for instance, in biological buffers), substantially altering their chemical behavior.

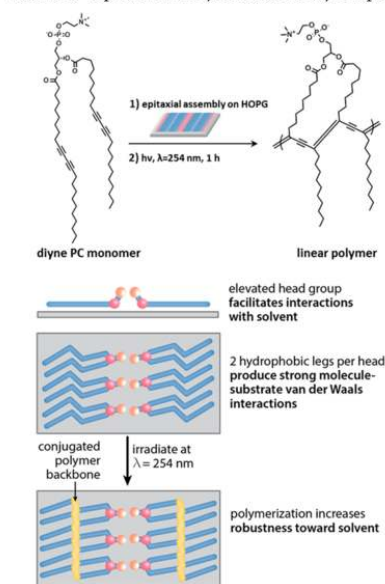
Interestingly, a vast amount of biology involving weak acids and bases occurs in a very similar chemical environment: at the periphery of the cellular membrane. Cellular membranes are largely composed of phosphoglycerolipids (typically 60–80%),<sup>50</sup> in which two long hydrophobic acyl chains connect through a three-carbon glycerol backbone to a hydrophilic head. The head is comprised of a phosphate group connected through a short linker to a terminal functional group that is exposed at the solvent interface. The nominal phosphate  $pK_a$  values of 1.0 for phosphocholine and 1.7 for phosphoethanolamine<sup>51</sup> mean that the group will remain charged at physiological pH (7.4), even if it undergoes an interfacial  $pK_a$  shift. Additionally, the structure of the glycerol backbone facilitates control over headgroup orientation relative to the hydrophobic chains that root it in the bilayer.

Here, we take advantage of the phospholipid architecture to develop an atom-efficient interfacial functionalization strategy that confers the benefits of both standing-up and lying-down monolayers. Lipids in this “sitting-phase” geometry coordinate the surface through two nonpolar alkyl legs, allowing the terminal functional group in the head to project from the interface (Scheme 1). Leveraging noncovalent assembly and subsequent polymerization utilizing polymerizable phospholipids makes fundamental and important differences in the surface chemistry that enable a new level of control over the ligand’s substrate and solvent interactions. A critical element of this strategy is the elevation of the terminal functional groups above the substrate and the monolayer to reduce interfacial  $pK_a$  shifts. Even modest separation also increases steric accessibility, which has previously been found to facilitate binding of analytes from solution.<sup>52,53</sup>

## RESULTS AND DISCUSSION

**Self-Assembled Sitting Phases of Diyne Phospholipids.** As a starting point for developing a sitting-phase ligand chemistry for layered materials, we first test the ability of polymerizable diyne phospholipids<sup>54,55</sup> to self-assemble into appropriate structural elements. Previous studies of diyne phospholipids in standing-phase monolayers and bilayers indicate that the headgroup tilts; as a result, the two functional alkyl chains penetrate different distances into the bilayer.<sup>56</sup> Thus, when the monolayer is polymerized, the two functional groups join two different polymer chains in the membrane, resulting in low molecular weight cross-linked polymers very

Scheme 1. Topochemical Polymerization of Diyne Lipids



different from the high molecular weight linear polymers that would be necessary to stabilize the sitting-phase monolayers targeted here.

Monolayers of diyne amphiphiles were prepared either by drop-casting a small amount of dilute amphiphile in organic solvent or through Langmuir–Schaefer deposition (see the Experimental Methods for details). Because monolayers of fatty acids such as pentacosadiynoic acid (PCDA) have been prepared previously, we compared self-assembled structures of PCDA (Figure 1a) and two polymerizable phospholipids: 1,2-bis(10,12-tricosadiynoyl)-*sn*-glycero-3-phosphocholine (diyne PC, Figure 1b) and 1,2-bis(10,12-tricosadiynoyl)-*sn*-glycero-3-phosphoethanolamine (diyne PE, Figure 1c). The two phospholipids differ only in the structure of the terminal headgroup functionality; diyne PE terminates in a primary amine, which may be charged or neutral depending on pH and solvent, while the diyne PC terminates in a quaternary ammonium group, which remains charged under all pH and solvent conditions.

A combination of atomic force microscopy (AFM), semi-empirical molecular modeling, and molecular dynamics simulation was used to examine molecular adsorption geometry. First, we assessed structural features in AFM images to address the question of whether molecules assemble head-to-head, creating double rows of headgroups with a ~6 nm periodicity (Scheme 1), or head-to-tail, resulting in single rows of headgroups with ~3 nm periodicity. Second, because the molecules can adsorb through two chemically different faces,



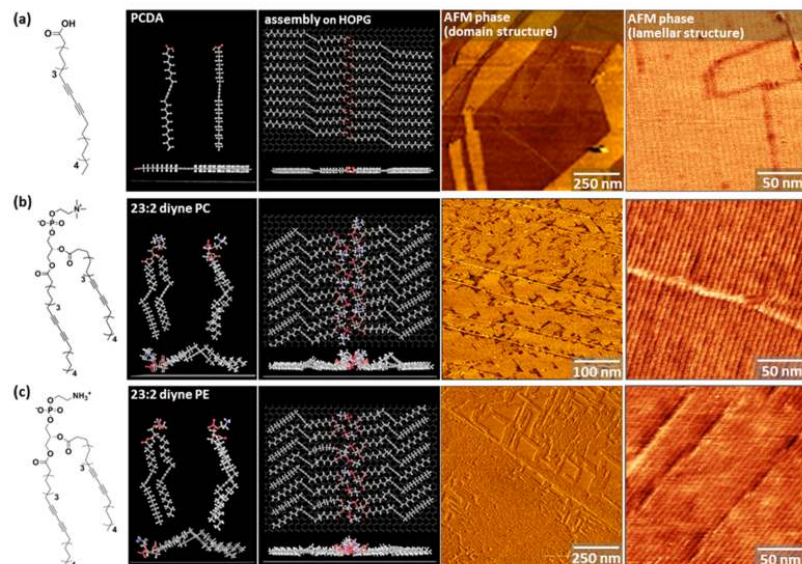


**Figure 1.** Modeled structures and AFM images of self-assembled polymerizable amphiphiles on HOPG. The first column shows (a) PCDA, (b) diyne PC, and (c) diyne PE. For each molecule, the second column shows two views of the solvent-minimized molecular structure (top) and a view of the solvent structure adsorbed to HOPG (bottom). The adsorbed structures were minimized to create the models in the third column, showing top and side views of each monolayer. In the fourth column, AFM phase images show large domains of molecules oriented epitaxially on HOPG; high-resolution images in the fifth column reveal lamellar periodicities ( $\sim 6$  nm) commensurate with the head-to-head models shown in the second column.

we performed energy minimizations to examine which adsorption geometry is preferred, an issue that would impact which functional groups in the head are most solvent-accessible.

AFM images of all three molecules deposited on HOPG reveal similar striped patterns with domains arranged at  $\sim 120^\circ$  angles, characteristic of epitaxy with the hexagonal HOPG lattice, as expected from previous experiments with diynoic acids.<sup>44</sup> Line scans extracted from high-resolution AFM images exhibit lamellar periodicities of  $6.3 \pm 0.1$  nm for diyne PE and  $6.6 \pm 0.1$  nm for diyne PC. This is in good agreement with the modeled widths of double lamellae (6.0 nm for diyne PE and 6.4 nm for diyne PC) plus a van der Waals contact distance. Importantly, this suggests that the head-to-head structure is energetically preferred for both phospholipids, since a head-to-tail arrangement would likely produce features with  $\sim 3$  nm periodicity.

Unlike the diynoic acids, both diyne phospholipids contain a chiral center in the headgroup, creating multiple possible adsorption geometries. Phospholipids may adsorb with the phosphate ( $-\text{PO}_2^-$ ) facing the substrate, increasing the solvent accessibility of the amine (and presumably partly screening the phosphate charge), or they may adsorb with the phosphate proximal to the solvent and the amine adjacent to the surface. To test which configuration is more energetically favorable, we created models consisting of two adjacent rows of

eight diyne lipids each adsorbed to a stack of two graphene sheets (see the [Supporting Information](#)), with all molecules adsorbed in either a phosphate-down configuration (Figure 2a) or a phosphate-up configuration (Figure 2b). Additionally, because the phosphocholine and phosphoethanolamine headgroups are narrower than the combined width of the two alkyl tails, it is possible to envision that headgroups from adjacent rows might interdigitate, leading to a configuration in which phosphates from one row lie next to the terminal amine or ammonium groups of molecules in the adjacent row. Such an interdigitated structure would be expected to increase the robustness of the monolayer, while likely decreasing the solvent accessibility of the headgroups. Therefore, we created sets of models in which molecules are initially positioned with interdigitated headgroups and models in which the rows are positioned 4 Å further apart, producing a noninterdigitated initial headgroup configuration. Minimization results in chloroform are presented in Figure 2c, as an energy difference between phosphate-down and phosphate-up adsorption geometries, expressed in units of eV/molecule (1 eV/molecule  $\approx$  96 kJ/mol). Both interdigitated and noninterdigitated initial headgroup configurations lead to an energetic preference of 0.6–0.7 eV/molecule for the phosphate-down configuration. Analyzing contributions from van der Waals and electrostatic interactions, strain, and solvation reveals that the preference

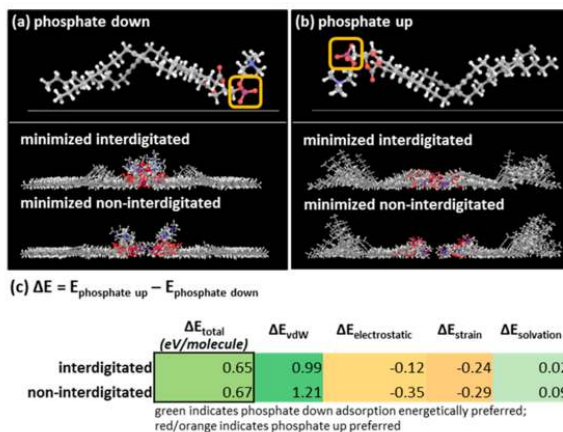


**Figure 2.** Minimizations of amphiphiles in phosphate-down and phosphate-up adsorption geometries. Minimized models of rows of molecules adsorbed in (a) phosphate-down and (b) phosphate-up configurations reveal greater tail group ordering for the phosphate-down configuration in both interdigitated and noninterdigitated headgroup configurations. (c) Energy differences between the two adsorption configurations indicate that the phosphate-down conformation is preferred due to increased van der Waals interactions.

arises from increased van der Waals interactions in the phosphate-down configuration. This is qualitatively visible in side views of the minimized models (Figure 2a,b) as increased ordering of the tail groups for phosphate-down structures in comparison with those of phosphate-up structures.

On the basis of modeling, it is not evident whether interdigitated headgroups would be preferred; however, a comparison of calculated and experimental lamellar widths suggests that the peripheries of the lamellar structures are not interdigitated. Minimizations of interdigitated structures lead to slightly smaller calculated average lamellar widths (5.8 nm for diyne PE and 5.7 nm for diyne PC) than those calculated for noninterdigitated structures (6.0 and 6.4 nm, vide supra). For diyne PC in particular (presumably due to the larger steric bulk of the terminal quaternary ammonium group), this leads to a relatively large difference between the modeled structure width and the structural periodicity observed experimentally in AFM images. Therefore, we postulate that the surface-adsorbed lipids adopt a noninterdigitated headgroup organization, which would increase the steric freedom of the terminal functional groups in comparison with an interdigitated structure.

**Polymerization of Diyne Phospholipids.** While individual molecules are relatively weakly adsorbed at the interface, surface-templated polymerization provides a route for increasing monolayer stability. Because diyne acid monolayers on HOPG are known to undergo surface-templated photopolymerization,<sup>40,44</sup> it is reasonable to expect the same reactivity from the diyne lipids we use here. However, a key structural consideration prompted us to examine molecular models to further explore the likelihood of polymerization: adjacent chains in lipid lamellae are bound together through the phospholipid headgroup, while the chains in diyne acid lamellae are not.

Such a consideration is important in the context of this surface-templated reaction for two reasons. First, photopolymerization rates for diynes are known to depend strongly on the distance between the two bond-forming carbons in the crystal. In 3D crystals of smaller diynes (particularly *p*-toluenesulfonate hexadiyne),<sup>37,58</sup> increases of 1.0 Å between the bond-forming carbons correspond to a 2-fold decrease in polymerization rate. Similar constraints hold in 2D domains of diacetylene; in addition to decreasing polymerization efficiency with increasing separation between bond-forming carbons, studies of diyne acids on HOPG and MoS<sub>2</sub> suggest differences in organization and polymerization behavior based on differences in lattice constants and work functions of the substrates.<sup>42–46</sup> For instance, on MoS<sub>2</sub>, polymerization efficiency is ~4 times higher than on HOPG, due to the increased conformational freedom afforded to alkyl chains in weaker epitaxy with the MoS<sub>2</sub> lattice.<sup>46</sup> A second structural consideration for polymerization is that the diyne functional group undergoes a rotation of ~45° in the plane of the substrate in order to join the growing ene-yne polymer chain.<sup>37</sup> Therefore, it is possible that the additional constraints placed on chains joined through a headgroup would prevent them from undergoing polymerization.

With these considerations in mind, we compare the average distance ( $D_{10-13}$ ) between bond-forming carbons (C10 of one chain and C13 of the adjacent chain) in monolayers of PCDA with those for the diyne phospholipid monolayers we form here. In calculating the C10–C13 distances for lipids, we examine pairs of chains both within a single molecule and between adjacent molecules. Minimized models of the diyne lipids show  $D_{10-13}(\text{diyne PC}) = 4.1$  Å, comparable to  $D_{10-13}(\text{PCDA}) = 4.0$  Å. In addition, the initial angle  $\Theta$  between the diyne and the lamellar axis is slightly smaller for the phospholipids ( $\Theta_{\text{PCDA}} = 59^\circ$ ,  $\Theta_{\text{diyne PC}} = 51^\circ$ ), leading to



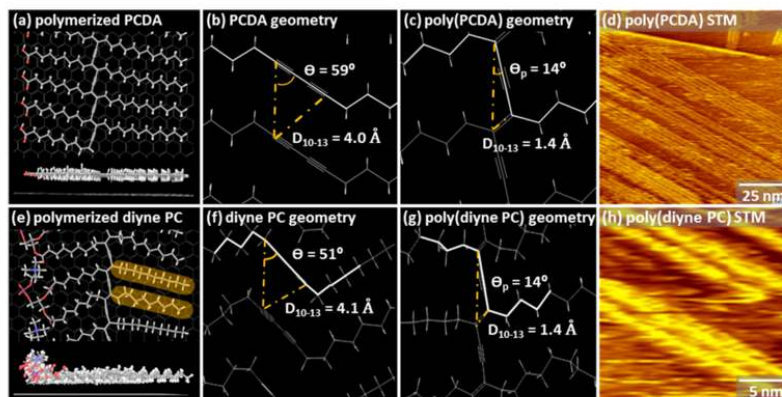


**Figure 3.** Energy-minimized molecular models and STM images showing polymerized (a–d) PCDA and (e–h) diyne PC. Minimized models of (b) unpolymerized PCDA and (f) diyne PC show that the distance between bond-forming carbons ( $D_{10-13}$ ) and the angle between diyne and lamellar axis ( $\Theta$ ) are similar for the two molecules. STM images of polymerized (d) PCDA and (h) diyne PC show apparent protrusions corresponding to the conjugated ene–yne polymer. Highlighting in panel e indicates the alternating alkyl chain orientation probed in Figure 5.

favorable reduced rotational angles relative to PCDA ( $\Delta\Theta_{\text{PCDA}} = 45^\circ$ ,  $\Delta\Theta_{\text{diyne PC}} = 34^\circ$ ).

STM images of polymerized diynes are known to exhibit features with increased apparent height due to formation of the conjugated ene–yne polymer backbone.<sup>4,40</sup> Figure 3 shows STM images of polymerized diynoic acids (Figure 3d) and polymerized diyne PC (Figure 3h). Apparent protrusions in the image appear corresponding to modulations in both the topography and the local density of electronic states (LDOS). The relatively small HOMO–LUMO gap in polymerized diacetylenes vs diacetylene monomers increases the LDOS near the Fermi level, increasing the probability of electron tunneling;<sup>41</sup> although the native band gap of bulk polydiacetylenes is 2.3–2.5 eV, p-doping from HOPG substrates can reduce the band gap to as little as 0.5 eV.<sup>42</sup> Imaging at sufficiently large negative sample biases (here,  $V_s = -1.5$  V) facilitates a two-step tunneling process that proceeds through the polydiacetylene wire.<sup>41,58</sup> While a number of studies provide experimental evidence suggesting that PCDA and other diynoic acids form a polymerized structure in which the ene–yne polymer is elevated  $\sim 1.4$  Å in relation to the surrounding alkyl chains,<sup>40,44</sup> DFT studies suggest that the lifted and in-plane polymer structures are similar in energy,<sup>60</sup> and in our simulations, models of both polymerized PCDA and diyne PC minimize to in-plane structures, though experimentally we find the standard linear features (Figure 3d) observed previously in STM images of polymerized PCDA. Previous studies imaging monolayers of long-chain diynes that do not form hydrogen-bonded dimers between headgroups (e.g. 17,19-hexatriacontadiyne) find a transition from a lifted phase at 220 K to the in-plane conformation at room temperature,<sup>61</sup> which lacks the protruding linear features visible in STM images of PCDA. Here, while we observe the appearance of some linear features in STM images of polymerized diyne phospholipids (Figure 3h), the surface density of such features is lower than for PCDA, which could indicate either lower polymerization

efficiency or the formation of an in-plane polymerized phase, as indicated in the minimized model (Figure 3e).

Because our primary interest is in the wetting properties of the interface, we use a washing assay to assess the impact of the polymerization on improving film robustness toward solvent. Samples of unpolymerized and polymerized amphiphiles were imaged and then subjected to sequential washing and imaging cycles to understand the extent to which washing removed molecules from the monolayer. Ethanol was used as a low surface tension washing solvent. Samples were washed vigorously with a stream of solvent from a squeeze bottle for 5-s intervals and then blown dry using compressed nitrogen gas. Figure 4 shows prewash and postwash images for unpolymerized and polymerized PCDA and diyne PE. Polymerized PCDA (Figure 4b) exhibits enhanced stability relative to unpolymerized PCDA (Figure 4a), demonstrating well-resolved lamellar structures within the domains throughout the washing procedure, although molecules at domain edges were eroded. The destabilizing effect of washing is also reflected in the increasing streakiness of the domain images, typically indicative of the presence of loose molecules. Conversely, a substantial fraction of the surface of the unpolymerized PCDA sample appeared bare after 5 s of washing, with only sparsely distributed aggregates of PCDA still visible, appearing as dark islands in the phase insets. In contrast, washing unpolymerized diyne PE (Figure 4c) resulted in slow etching of domain edges, with  $\sim 40\%$  of the surface containing ordered domains even after 30 s of washing. For polymerized diyne PE (Figure 4d), etching around domain edges was much slower, and  $\sim 80\%$  of the surface remained covered after 30 s of washing. We postulate that the enhanced stability of both polymerized and unpolymerized phospholipids relative to the diynoic acids may result from the increased number of alkyl carbons per molecule.

Molecular models suggest substantial differences in alkyl chain orientation between PCDA and the diyne phospholipids

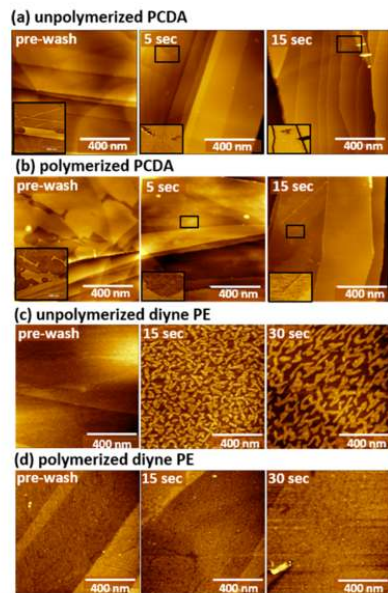


**Figure 4.** Solvent washing assay for unpolymerized and polymerized PCDA (a and b) and diyne PE (c and d) shows the enhanced stability of polymerized monolayers in comparison with unpolymerized monolayers and increased stability of diyne PE vs PCDA. Insets of panels a and b show phase images of the entire images or the corresponding scanned areas marked by the black square.

(Figure 3a,e). In PCDA, strong hydrogen-bonding interactions in carboxylic acid dimers order the headgroups, and tails form a tightly packed lattice with the zigzag backbone of the alkyl chains parallel to the HOPG surface.<sup>40</sup> In contrast, our models suggest that the lipid headgroups are somewhat disordered due to the three-dimensional geometry around the glycerol backbone. Our models also suggest that the lipid tail groups form an unusual structure in which the alkyl chains alternately zigzag parallel and perpendicular to the HOPG surface (highlighted in Figure 3e). Polarization modulated IR reflection absorption spectroscopy (PM-IRRAS)<sup>62</sup> measurements of films of PCDA and diyne lipids on HOPG exhibit substantial differences in C–H stretch intensity (Figure 5a) consistent with this difference in ordering. Ester C=O stretch peak intensities for diyne PC are also reduced relative to PCDA C=O stretch intensities (Figure 5b), consistent with energy-minimized models, suggesting that the ester linkage adopts a variety of configurations relative to the surface normal, in order to bring the two diynes into alignment as the lipid conforms to the graphite surface.

**Controlling the Charge State of Surface Functional Group Patterns.** The difference in placement of the phosphate and amine functional groups relative to the interface

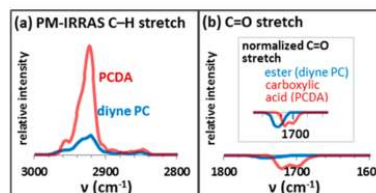


**Figure 5.** PM-IRRAS spectra of films of PCDA and diyne PC exhibit differences in (a) C–H and (b) C=O stretch intensities consistent with alkyl chain orientation differences observed in energy-minimized molecular models.

is expected to impact their ionization and, thus, interactions with solvents and analytes.

A number of techniques, including differential capacitance measurements,<sup>63</sup> nonlinear optical spectroscopy,<sup>64</sup> and contact angle goniometry,<sup>48</sup> can be used to assess ionization behavior at interfaces. Here, we use contact angle titration, in which a series of small droplets of buffers with controlled pH are applied to the interface; the contact angles of the buffer droplets change in pH ranges corresponding to the ionization of functional groups at the interface.<sup>65</sup> Interfacial  $pK_{1/2}$  values are known to differ substantially from  $pK_s$  of the same functionalities in solution. For instance, the  $pK_s$  of acetic acid in dilute aqueous solution is  $\sim 4.7$ .<sup>65</sup> However, previously it has been shown that both carboxylic acid-terminated SAMs and oxidized polymer films displaying carboxylic acids typically exhibit  $pK_{1/2}$  values of 7–8.<sup>48</sup> Similarly,  $pK_{1/2}$  values of amines in alkanethiol SAMs typically decrease relative to  $pK_s$  values in aqueous solutions. While the  $pK_s$  of dilute methylamine in aqueous solution is 10.5,<sup>49</sup> one study measured a  $pK_{1/2}$  of 6.5 for an  $NH_2$ -terminated undecanethiol SAM, lower than the measured  $pK_{1/2}$  of 7.4 for a COOH-terminated undecanethiol SAM measured in the same work.<sup>49</sup> Both shifts can be understood by considering the equilibrium between charged and neutral forms of the molecules; in both amines and carboxylic acids, proximity to the nonpolar interface decreases stabilization of the charged form of the functional group, shifting the equilibrium toward the neutral form. Similarly,  $pK_{1/2}$  has been shown to vary with the surface density of functional groups in a SAM.<sup>48</sup> For a 75% COOH-terminated alkyl SAM, the measured  $pK_{1/2}$  was 8.5, while for a lower-coverage 15% COOH-terminated alkyl SAM, the  $pK_{1/2}$  shifted as high as 11.

Both surface shifts and those due to fractional coverage are important in predicting the ionization behavior of functional groups in the monolayers prepared here. Figure 1a shows that for PCDA monolayers, approximately 10% of the surface consists of ionizable functional groups. However, the chemical environment of the carboxylic acid groups is more similar to that which would be found in a high-percentage COOH-terminated alkyl thiol SAM, since the functionalities are clustered at the lamellar edges.

Figure 6 shows the results of contact angle titrations for pentacosane, PCDA, diyne PC, and diyne PE. For films of pentacosane (Figure 6a), a 25-carbon alkane, on HOPG, contact angles are  $\sim 98^\circ$  across the tested pH range (1–13). For PCDA (Figure 6b, squares = advancing, circles = receding), contact angles are lower than for pentacosane due to the introduction of the polar carboxylic acid functional group.



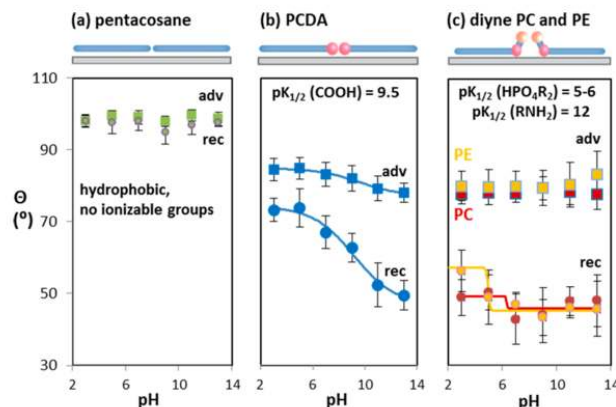


**Figure 6.** Contact angle titrations showing changes in contact angle with buffer pH for HOPG with adsorbed (a) pentacosane, (b) polymerized PCDA, and (c) polymerized diyne lipids PC and PE. Square markers indicate advancing contact angles; circles indicate receding contact angles. Error bars indicate the standard deviation in angle over a series of nine measurements acquired from three different samples.

Below pH 5, the carboxylic acids are neutral, leading to advancing contact angles of  $\sim 84^\circ$ . We correlate this decrease with the fractional surface coverage of carboxylic acids using a modified form of the Young–Dupré equation for interfaces with nanoscale chemical heterogeneity:<sup>66</sup>

$$(1 + \cos \theta_{\text{PCDA}})^2 = f_{\text{alkyl}}(1 + \cos \theta_{\text{alkyl}})^2 + f_{\text{COOH}}(1 + \cos \theta_{\text{COOH}})^2$$

Using the measured contact angle of  $98^\circ$  for alkyl chains aligned epitaxially on HOPG,  $84^\circ$  for neutral PCDA, and  $30^\circ$  for neutral COOH groups (value observed in previous contact angle measurements on 100% COOH-terminated alkyl thiol SAMs<sup>48</sup>), the observed decrease in contact angle relative to pentacosane would be expected for an 18% surface coverage of neutral carboxylic acid groups, consistent with moderate disordering of the COOH groups during wetting. We note that it is not entirely clear that the contact angle for a lying-down phase of COOH dimers would be exactly the same as that ( $30^\circ$ ) for a standing phase of alkanethiol-terminated COOH groups and that, if the bond dipoles in the carboxylic acid are oriented in the plane of the monolayer, this would lead to a somewhat higher water contact angle. Using a larger contact angle in the above equation results in a higher calculated  $f_{\text{COOH}}$ , implying more disordering at the interface and a disruption of the COOH dimers along the periphery of the lamellar structure. This reorientation would produce hydrophilic areas with unpaired  $-\text{COOH}$  groups more closely resembling standing-phase COOH-terminated alkanethiols. Thus, the calculated hydrophilic surface coverage of 18% should be considered an approximate but reasonable minimum.

With increasing pH, the carboxylic acids begin to ionize, further decreasing both advancing and receding angles. On the basis of the receding angles (blue circles), in which the larger change in contact angle makes the transition more evident, we estimate an onset of ionization at pH 5 and a  $\text{p}K_{1/2}$  of 9.5, using

a sigmoidal fit (blue line). Therefore, while the  $\text{p}K_{1/2}$  is shifted due to the nonpolar environment at the interface, clustering the carboxylic acid groups at lamellar edges decreases the  $\text{p}K_{1/2}$  relative to the value of 11 measured previously for 15% COOH-terminated standing phases of alkanethiol SAMs on Au(111).<sup>48</sup>

In contrast with PCDA, diyne PC (Figure 6c, red squares = advancing; red circles = receding) has a terminal quaternary ammonium group that remains charged across the pH range, leading to advancing contact angles  $\sim 74^\circ$ , similar to those for the ionized form of PCDA. Although the ammonium group remains charged, at low pH, the phosphate group can become protonated. While the solution  $\text{p}K_a$  for a phosphocholine phosphate is 1, here we observe a  $\text{p}K_{1/2}$  of approximately 5.9, consistent with the interfacial  $\text{p}K_a$  shift of the carboxylic acid in PCDA. Similarly, for diyne PE, an increase in receding contact angle is observed at low pH (Figure 6c, yellow circles), with a calculated  $\text{p}K_{1/2} = 4.9$ . This sigmoidal fit was calculated using additional data points below pH 3 to improve accuracy (see the Supporting Information).

The diyne PE primary amine has a solution  $\text{p}K_a$  of 11. A small increase in the advancing contact angle is observed near pH 11 (Figure 6c, yellow squares), consistent with neutralization of the amine. No corresponding increase in receding angle is observed (Figure 6c, yellow circles), presumably because the phosphate group remains charged and can influence the receding angle more strongly than the advancing angle. Importantly, this suggests that the diyne PE amine does not undergo a significant interfacial  $\text{p}K_{1/2}$  shift due to its separation from the hydrophobic interface and the proximity of the charged phosphate group.

## CONCLUSIONS AND PROSPECTS

Here, we have demonstrated a route for functionalization of layered materials based on sitting phases of polymerizable lipids. The lipids contain multiple functional groups (phosphate and amine or ammonium) that are precisely positioned relative

to the layered material interface. Because the phosphate sits close to the interface, it experiences a  $pK_a$  shift characteristic of functional groups at hydrophobic interfaces; conversely, the terminal primary amine in diene PE, which projects just a few angstroms above the interface, maintains its standard solution ionization behavior. This difference points to the ability to tailor chemical characteristics of the interface by varying the functionalities present in the lipid headgroup and their positions relative to the interface.

On the basis of the diversity of natural lipids (over 100 unique lipids have been identified to date),<sup>50</sup> it is reasonable to suppose that a large amount of structural and chemical diversity can be introduced into monolayers using this strategy. In biology, lipids are known to play roles in stabilizing membrane curvature and junctions, protein interactions, regulating cell growth, and biosynthetic pathways, suggesting the possibility that similarly diverse functions could be stably integrated with layered materials.

## ■ EXPERIMENTAL METHODS

**Amphiphile Monolayer Preparation.** Diacetylene-functionalized phospholipids and fatty acids were purchased from suppliers indicated and used as received: 1,2-bis(10,12-tricosadiynoyl)-*sn*-glycero-3-phosphocholine (Avanti Lipids, Alabaster, AL, >99.0% purity), 1,2-bis(10,12-tricosadiynoyl)-*sn*-glycero-3-phosphoethanolamine (Avanti, >99.0% purity), 10,12-pentacosadiynoic acid (Sigma-Aldrich, St. Louis, MO, ≥97.0% purity), and 10,12-nonacosadiynoic acid (Tokyo Chemical International, Tokyo, Japan, >97.0% purity). Chloroform, hexane, and isopropyl alcohol (ChromAR grade) were purchased from Macron Fine Chemicals (Center Valley, PA) and used as received. Self-assembled monolayers of diacetylene-functionalized lipids and fatty acids were prepared either by drop-casting or Langmuir–Schaefer (LS) deposition as described below. In both techniques, polymerizable amphiphiles were deposited on  $1 \times 1$  cm highly oriented pyrolytic graphite (HOPG, SPI Supplies, West Chester, PA) substrates, which were freshly cleaved immediately prior to sample deposition. All initial steps in the deposition process were carried out under UV-filtered light to prevent polymerization in solution.

For samples prepared by drop-casting, monolayers of lipids and fatty acids were formed by placing 6  $\mu$ L of a 0.015–0.017 mg/mL solution of the functional molecule in a 3:2 (v/v) mixture of hexane:isopropyl alcohol on a heated (90–107 °C) HOPG substrate. LS deposition was performed using a KSV-NIMA Langmuir–Blodgett trough (Biolin Scientific, Stockholm, Sweden). For the deposition of fatty acids, 12  $\mu$ L of a 0.75 mg/mL solution of fatty acid in chloroform was deposited on a subphase of deionized water (~18 M $\Omega$ ). For phospholipid monolayers, deposition was performed by spreading 15–20  $\mu$ L of a 0.5 mg/mL solution of lipid in chloroform onto a subphase of aqueous 5 mM MnCl<sub>2</sub>. After the small amount of chloroform used for amphiphile transfer was allowed to evaporate, trough barriers were slowly moved inward to adjust the surface pressure. When the surface pressure reached 10 mN/m, the HOPG substrate was slowly lowered onto the subphase with the cleaved surface facing down, parallel to the liquid interface. After 4 min in contact with the liquid interface, the HOPG was gently lifted out of contact with the liquid using the automatic dipper.

Diacetylene-functionalized amphiphile monolayers prepared using the described procedure were photopolymerized by 1 h of irradiation under a 254-nm 8-W UV lamp with approximately 4 cm between the lamp and the sample surface.

**AFM Imaging.** All AFM measurements were performed under ambient conditions using a Veeco MultiMode (Bruker Instruments, Billerica, MA) instrument in tapping mode with Nanoprobe (Neuchatel, Switzerland) PPP-FM or RFESP-75 tips (nominal force constant 3 N/m and radius of curvature <10 nm).

**STM Imaging.** STM images were acquired using a custom-built ambient STM<sup>67–69</sup> with a Besocke-type head design and RHK-R9

control electronics (RHK Technology, Troy, MI). STM tips were prepared mechanically from Pt/Ir alloy wire (Goodfellow, Pt 90%, Ir 10%). Imaging was performed in constant current mode with a tip bias of 1.5 V and tunneling current set point of 7 pA.

**Energy Minimization.** Software packages Maestro<sup>46</sup> and Macro-model<sup>47</sup> (Schrödinger, Cambridge, MA) were used, respectively, to visualize the structures of phospholipids and fatty acids on graphene and to perform the force field minimizations and molecular dynamics simulations. All models were minimized using the OPLS\_2005 force field,<sup>48</sup> with normal cutoffs for van der Waals, electrostatic, and hydrogen-bonding interactions. Minimization were performed using the Polak–Ribiere conjugate gradient (PRCG) algorithm and gradient method with 50 000 runs and a convergence threshold of 0.05. Most minimizations converged in less than 10 000 runs. For all calculations, atoms in the graphene sheets were frozen, to more closely mimic the structure of HOPG. Thus, while they contributed to the forces present in the system, their positions did not change in response to conformational changes of the adsorbed amphiphiles. For simulations using aqueous buffers, molecular dynamics simulations were carried out using explicit water and ions to simulate 5 mM MnCl<sub>2</sub> (see the Supporting Information). Briefly, 1680 water molecules, 19 Mn<sup>2+</sup> ions, and 38 Cl<sup>−</sup> were positioned with appropriate spacings over graphene sheets identical to those used in chloroform and solvent-free minimizations. Molecular dynamics simulations were run for 200 ps; models were subsequently re-minimized and energy values tabulated as for other models.

**Contact Angle Titrations.** Contact angle titrations were performed using an Attension Theta optical tensiometer (Biolin Scientific, Stockholm, Sweden) in sessile drop mode. Buffers with 20 mM buffering capacity at a range of pH values from 1 to 14 were purchased from Sigma-Aldrich and used as received. The pH of each buffer was measured prior to utilization in contact angle measurements to ensure that the measured pH was within 0.2 units of the stated pH. For each measurement, a 5- $\mu$ L droplet of buffer solution at the stated pH was deposited on a prepared sample of polymerized amphiphile on HOPG, and the contact angle was measured within 10 s and recorded as the advancing contact angle. Subsequently, solvent was withdrawn from the droplet using a syringe with a 32-gauge needle, until the solvent front on the sample receded. The contact angle was measured at this point and recorded as the receding contact angle. Each contact angle graphed in the paper represents the average of nine points (three points measured on each of three different samples). Typically, it was possible to acquire a grid of nine measurements per  $1 \times 1$  cm sample.

**PM-IRRAS.** Spectra were acquired using a custom-built PM-IRRAS spectrophotometer. The infrared light source, interferometer, and data collection and processing were provided by a Nicolet i550R spectrometer (Thermo, Waltham, MA). All optical components were purchased from Thorlabs (Newton, NJ) unless otherwise specified. The infrared beam was passed from the spectrometer exit port into a polycarbonate enclosure and directed through a KRS-5 lens at a 70° incidence angle using AR-coated gold mirrors. The beam then passed through a holographic BaF<sub>2</sub> linear polarizer set at an angle of 45° relative to the optical axis of a Hinds Series II ZNS50 photoelastic modulator (Hinds Instruments, Portland, OR), which modulated the beam at a 50 kHz frequency with the half-wave retardation set to 2100 cm<sup>−1</sup>. The beam was then focused onto the sample and reflected through a second BaF<sub>2</sub> linear polarizer, which was adjusted to minimize the polarization effects of the substrate. Finally, the light was focused through a BaF<sub>2</sub> lens onto a HgCdTe high D\* detector (Thermo, Waltham, MA). Spectra were acquired at 8 cm<sup>−1</sup> resolution and normalized by dividing a spectrum of the substrate with a monolayer by a spectrum of a bare substrate.

## ■ ASSOCIATED CONTENT

### Supporting Information

The Supporting Information is available free of charge on the ACS Publications website at DOI: 10.1021/jacs.5b13179.



Additional descriptions of molecular models, contact angle repeatability profiling, and data used for sigmoidal curve fitting of diyne PE below pH 3 (PDF)

## AUTHOR INFORMATION

### Corresponding Author

\*claridge@purdue.edu

### Author Contributions

J.J.B. and K.K.R. contributed equally to this work.

### Notes

The authors declare no competing financial interests.

## ACKNOWLEDGMENTS

S.A.C. and J.J.B. acknowledge support through an ACS Petroleum Research Fund Doctoral New Investigator Award (PRF# 54763-DNIS), and S.A.C. acknowledges support through an NSF CAREER award (NSF-CHE 1555173). S.R.R. has been supported through a W. Brooks Fortune Predoctoral Fellowship and a Frederick N. Andrews Predoctoral Fellowship. The authors are grateful to D. Thompson for helpful discussions, and D. McMillan and H. Hedderich for technical assistance.

## REFERENCES

- Groves, J. T.; Ulman, N.; Boxer, S. G. *Science* **1997**, 275, 651.
- Cremier, P. S.; Boxer, S. G. *J. Phys. Chem. B* **1999**, 103, 2554.
- Groves, J. T.; Boxer, S. G. *Acc. Chem. Res.* **2002**, 35, 149.
- Claridge, S. A.; Liao, W.-S.; Thomas, J. C.; Zhao, Y.; Cao, H. H.; Cheunkar, S.; Serino, A. C.; Andrews, A. M.; Weiss, P. S. *Chem. Soc. Rev.* **2013**, 42, 2725.
- Bain, C. D.; Troughton, E. B.; Tao, Y. T.; Evall, J.; Whitesides, G. M.; Nuzzo, R. G. *J. Am. Chem. Soc.* **1989**, 111, 321.
- Nuzzo, R. G.; Dubois, L. H.; Allara, D. L. *J. Am. Chem. Soc.* **1990**, 112, 558.
- Laibinis, P. E.; Whitesides, G. M.; Allara, D. L.; Tao, Y. T.; Parikh, A. N.; Nuzzo, R. G. *J. Am. Chem. Soc.* **1991**, 113, 7152.
- Love, J. C.; Estroff, L. A.; Kriebel, J. K.; Nuzzo, R. G.; Whitesides, G. M. *Chem. Rev.* **2005**, 105, 1103.
- Poirier, G. E. *Chem. Rev.* **1997**, 97, 1117.
- Burda, C.; Chen, X. B.; Narayanan, R.; El-Sayed, M. A. *Chem. Rev.* **2005**, 105, 1025.
- Alivisatos, A. P. *Science* **1996**, 271, 933.
- Steigerwald, M. L.; Brus, L. E. *Acc. Chem. Res.* **1990**, 23, 183.
- Murray, C. B.; Kagan, C. R.; Bawendi, M. G. *Annu. Rev. Mater. Sci.* **2000**, 30, 545.
- Shirasaki, Y.; Supran, G. J.; Bawendi, M. G.; Bulovic, V. *Nat. Photonics* **2013**, 7, 13.
- Claridge, S. A.; Castleman, A. W.; Khanna, S. N.; Murray, C. B.; Sen, A.; Weiss, P. S. *ACS Nano* **2009**, 3, 244.
- Alivisatos, A. P.; Gu, W. W.; Larabell, C. *Annu. Rev. Biomed. Eng.* **2005**, 7, 55.
- Alivisatos, A. P.; Johnsson, K. P.; Peng, X. G.; Wilson, T. E.; Loweth, C. J.; Bruchez, M. P.; Schultz, P. G. *Nature* **1996**, 382, 609.
- Manna, L.; Scher, E. C.; Alivisatos, A. P. *J. Am. Chem. Soc.* **2000**, 122, 12700.
- Mirkin, C. A.; Letsinger, R. L.; Mucic, R. C.; Storhoff, J. J. *Nature* **1996**, 382, 607.
- Park, S. Y.; Lytton-Jean, A. K. R.; Lee, B.; Weigand, S.; Schatz, G. C.; Mirkin, C. A. *Nature* **2008**, 451, 553.
- Butler, S. Z.; Hollen, S. M.; Cao, L.; Cui, Y.; Gupta, J. A.; Gutierrez, H. R.; Heinz, T. F.; Hong, S. S.; Huang, J.; Ismach, A. F.; Johnston-Halperin, E.; Kuno, M.; Plashnitsa, V. V.; Robinson, R. D.; Ruoff, R. S.; Salahuddin, S.; Shan, J.; Shi, L.; Spencer, M. G.; Terrones, M.; Windl, W.; Goldberger, J. E. *ACS Nano* **2013**, 7, 2898.
- Geim, A. K. *Science* **2009**, 324, 1530.
- MacLeod, J. M.; Rosei, F. *Small* **2014**, 10, 1038.
- Mann, J. A.; Dichtel, W. R. *J. Phys. Chem. Lett.* **2013**, 4, 2649.
- Kozbial, A.; Li, Z.; Conaway, C.; McGinley, R.; Dhingra, S.; Vahdat, V.; Zhou, F.; D'Urso, B.; Liu, H.; Li, L. *Langmuir* **2014**, 30, 8598.
- De Feyter, S.; De Schryver, F. C. *Chem. Soc. Rev.* **2003**, 32, 139.
- Giancarlo, L. C.; Flynn, G. W. *Acc. Chem. Res.* **2000**, 33, 491.
- Cyr, D. M.; Venkataraman, B.; Flynn, G. W. *Chem. Mater.* **1996**, 8, 1600.
- Giancarlo, L. C.; Flynn, G. W. *Annu. Rev. Phys. Chem.* **1998**, 49, 297.
- Wei, Y. H.; Kannappan, K.; Flynn, G. W.; Zimmt, M. B. *J. Am. Chem. Soc.* **2004**, 126, 5318.
- Elemans, J. A. A. W.; Lei, S.; De Feyter, S. *Angew. Chem., Int. Ed.* **2009**, 48, 7298.
- Claridge, S. A.; Thomas, J. C.; Silverman, M. A.; Schwartz, J. J.; Yang, Y.; Wang, C.; Weiss, P. S. *J. Am. Chem. Soc.* **2013**, 135, 18528.
- Mao, X.; Guo, Y.; Luo, Y.; Niu, L.; Liu, L.; Ma, X.; Wang, H.; Yang, Y.; Wei, G.; Wang, C. *J. Am. Chem. Soc.* **2013**, 135, 2181.
- Furukawa, H.; Cordova, K. E.; O'Keefe, M.; Yaghi, O. M. *Science* **2013**, 341, 974.
- Samori, P.; Fechtenkotter, A.; Jackel, F.; Bohme, T.; Mullen, K.; Rabe, J. P. *J. Am. Chem. Soc.* **2001**, 123, 11462.
- Gellman, A. J.; Paserba, K. R. *J. Phys. Chem. B* **2002**, 106, 13231.
- Grim, P. C. M.; De Feyter, S.; Gesquiere, A.; Vanoppen, P.; Ruker, M.; Valiyaveetil, S.; Moessner, G.; Mullen, K.; De Schryver, F. C. *Angew. Chem., Int. Ed. Engl.* **1997**, 36, 2601.
- Colson, J. W.; Woll, A. R.; Mukherjee, A.; Levendorf, M. P.; Spittler, E. L.; Shields, V. B.; Spencer, M. G.; Park, J.; Dichtel, W. R. *Science* **2011**, 332, 228.
- Cui, D.; MacLeod, J. M.; Ebrahimi, M.; Perepichka, D. F.; Rosei, F. *Chem. Commun.* **2015**, 51, 16510.
- Okawa, Y.; Aono, M. *J. Chem. Phys.* **2001**, 115, 2317.
- Akai-Kasaya, M.; Shimizu, K.; Watanabe, Y.; Saito, A.; Aono, M.; Kuwahara, Y. *Phys. Rev. Lett.* **2003**, 91, 255501.
- Giridharagopal, R.; Kelly, K. F. *ACS Nano* **2008**, 2, 1571.
- Okawa, Y.; Aono, M. *Nature* **2001**, 409, 683.
- Okawa, Y.; Akai-Kasaya, M.; Kuwahara, Y.; Mandal, S. K.; Aono, M. *Nanoscale* **2012**, 4, 3013.
- Deshpande, A.; Sham, C.-H.; Alaboson, J. M. P.; Mullin, J. M.; Schatz, G. C.; Hersam, M. C. *J. Am. Chem. Soc.* **2012**, 134, 16759.
- Mandal, S. K.; Okawa, Y.; Hasegawa, T.; Aono, M. *ACS Nano* **2011**, 5, 2779.
- Tahara, K.; Katayama, K.; Blunt, M. O.; Iritani, K.; De Feyter, S.; Tobe, Y. *ACS Nano* **2014**, 8, 8683.
- Bain, C. D.; Whitesides, G. M. *Langmuir* **1989**, 5, 1370.
- Fears, K. P.; Creager, S. E.; Latour, R. A. *Langmuir* **2008**, 24, 837.
- Biochemistry of Lipids, Lipoproteins and Membranes*, 5th ed.; Vance, D. E., Vance, J. E., Eds.; Elsevier: New York, 2008.
- Marsh, D. *Handbook of Lipid Bilayers*, 2nd ed.; CRC Press: Boca Raton, FL, 2013.
- Shuster, M. J.; Vaish, A.; Szapacs, M. E.; Anderson, M. E.; Weiss, P. S.; Andrews, A. M. *Adv. Mater.* **2008**, 20, 164.
- Vaish, A.; Shuster, M. J.; Cheunkar, S.; Singh, Y. S.; Weiss, P. S.; Andrews, A. M. *ACS Chem. Neurosci.* **2010**, 1, 495.
- O'Brien, D. F.; Whitesides, T. H.; Klingbiel, R. T. *J. Polym. Sci., Polym. Lett. Ed.* **1981**, 19, 95.
- Zhang, H.; Joubert, J. R.; Saavedra, S. S. *Adv. Polym. Sci.* **2009**, 224, 1.
- Lopez, E.; O'Brien, D. F.; Whitesides, T. H. *J. Am. Chem. Soc.* **1982**, 104, 305.
- Baughman, R. H. *J. Appl. Phys.* **1972**, 43, 4362.
- Wegner, G. *Makromol. Chem.* **1971**, 145, 85.
- Giridharagopal, R.; Kelly, K. F. *J. Phys. Chem. C* **2007**, 111, 6161.
- Okawa, Y.; Takajo, D.; Tsukamoto, S.; Hasegawa, T.; Aono, M. *Soft Matter* **2008**, 4, 1041.
- Endo, O.; Toda, N.; Ozaki, H.; Mazaki, Y. *Surf. Sci.* **2003**, 545, 41.

- (62) Russell, S. R.; Claridge, S. A. *Anal. Bioanal. Chem.* **2016**, DOI: 10.1007/s00216-015-9262-5.
- (63) Bryant, M. A.; Crooks, R. M. *Langmuir* **1993**, *9*, 385.
- (64) Zhao, X. L.; Subrahmanyam, S.; Eisenthal, K. B. *Chem. Phys. Lett.* **1990**, *171*, 558.
- (65) *CRC Handbook of Chemistry and Physics*; 95th ed.; CRC Press, Inc.: Boca Raton, FL, 2014.
- (66) Israelachvili, J. N. *Intermolecular and Surface Forces*, 3rd ed.; Elsevier: Waltham, MA, 2011.
- (67) Bumm, L. A.; Weiss, P. S. *Rev. Sci. Instrum.* **1995**, *66*, 4140.
- (68) Moore, A. M.; Yeganeh, S.; Yao, Y. X.; Claridge, S. A.; Tour, J. M.; Ratner, M. A.; Weiss, P. S. *ACS Nano* **2010**, *4*, 7630.
- (69) Bang, J. J.; Russell, S. R.; Rupp, K. K.; Claridge, S. A. *Anal. Methods* **2015**, *7*, 7106.